UNIVERSITÀ DELLA CALABRIA

UNIVERSITA' DELLA CALABRIA
Dipartimento di Fisica

Dottorato di Ricerca in
Scienze e Tecnologie Fisiche, Chimiche e dei Materiali in convenzione con il CNR

CICLO
XXXII

X-RAY PHASE-CONTRAST TOMOGRAPHY APPLIED TO VIRTUAL UNFOLDING OF HERCULANEUM PAPYRI

Settore Scientifico Disciplinare FIS-07

Coordinatore: Ch.ma Prof.ssa Gabriella Cipparrone

[redacted]

Supervisore: Dott.ssa Alessia C[redacted]

[redacted]

Co-Supervisore: Dot[redacted]

Firma oscurata in base alle linee guida del Garante della privacy

[redacted]

Dottoranda:[redacted] Dott.ssa Sara Stabile

Firma oscurata in base alle linee
guida del Garante della privacy

I would like to dedicate this thesis to my loving family

Sommario

Nel 1750 su una collina che domina Ercolano e il Golfo di Napoli fu scoperta una grande villa. Questa villa aristocratica pare appartenesse, secondo l'ipotesi più accreditata, a Lucio Calpurnio Pisone Cesonino, noto uomo politico romano, nonché protettore del filosofo Filodemo di Gadara. La villa fu seppellita sotto una coltre di detriti vulcanici di circa trenta metri durante la catastrofica eruzione vesuviana del 79 d. C.

Nel corso degli scavi nella villa, furono riportati alla luce non solo affreschi e pavimenti, ma anche un gran numero di statue e circa 1800 rotoli di papiri, divenuta nota perciò come Villa dei Papiri. Si tratta di una notevole collezione di opere greche e alcune anche latine perdute dalla tradizione medievale, in particolare trattati di Epicuro e dei suoi epigoni fino a Filodemo di Gadara.

Sepolti sotto una coltre di materiale lavico e sottoposti ad una temperatura elevatissima, i papiri di Ercolano hanno subìto un processo di combustione che ne ha consentito la conservazione, ma li ha resi dei blocchi estremamente fragili, friabili e compatti. Il peso dei detriti sotto cui sono rimasti per secoli, non solo ha reso compatti i vari strati, ma ne ha provocato la rottura, la deformazione, lo schiacciamento e il raggrinzimento.

Fin dall'epoca della loro scoperta, i papiri di Ercolano sono stati al centro di grande interesse da parte degli studiosi e numerose tecniche manuali e purtroppo distruttive sono state impiegate per poter srotolarli e leggere le inestimabili informazioni in essi contenute.

Il mio lavoro di ricerca di Dottorato riguarda lo studio dei papiri di Ercolano utilizzando tecniche non distruttive a raggi X con una serie di nuovi algoritmi numerici per lo "srotolamento virtuale".

In particolare, ho usato la Micro Tomografia Computerizzata a raggi X (μ-CT) e la Tomografia a Contrasto di Fase a raggi X (XPCT) come potenti tecniche di test non distruttive per l'ispezione dell'intero volume dei papiri in grado di dare informazioni morfologiche e fisiche sulla struttura interna del campione esaminato. Ho analizzato tre frammenti di papiri di Ercolano: *PHerc.1103* e *PHerc.1105* che appartengono alla parte esterna, scorza, e *PHerc.110* che appartiene ad un papiro parzialmente srotolato nel 1867.

Lo scopo principale del mio lavoro di ricerca è stato costruire una piattaforma computazionale per l'indagine virtuale 3D dei frammenti di papiri. A causa delle loro cat-

tive condizioni, le operazioni sulle immagini tomografiche 3D, come la segmentazione e l'appiattimento dei fogli, risultano complicate e richiedono un approccio sviluppato appositamente per questo particolare compito.
In questa tesi, descrivo in dettaglio la piattaforma computazionale sviluppata, che è il risultato composito della digitalizzazione, segmentazione, modellizzazione, appiattimento e texture mapping dei dati 3D del foglio di papiro.
Dopo la digitalizzazione 3D dei dati, presento il passaggio di segmentazione, grazie al quale posso identificare digitalmente il singolo foglio di papiro all'interno del volume. Il passaggio successivo è la modellazione della superficie del foglio mediante l'uso di una mesh triangolare, preferibile ad altri tipi di mesh perché semplifica la matematica e consente operazioni più veloci. Infine, mi concentro sui metodi di parametrizzazione per l'appiattimento del foglio che introducono distorsioni minime. Una volta identificato il metodo di parametrizzazione corretto, il passaggio successivo consiste nel texturing, ovvero l'assegnazione delle informazioni di colore 3D a ciascun punto sulla mesh 2D. La trama risultante rivela le caratteristiche del foglio appiattito.

Inoltre, sono state condotte indagini su diversi metodi di recupero di fase. Ho implementato e testato tre dei metodi più diffusi per trovare quello migliore. Un altro problema impegnativo, dovuto agli artefatti ad anello presenti nella ricostruzione che disturba la qualità delle immagini, è stato risolto attraverso algoritmi adattati a questo caso particolare. Il processo di rimozione degli artefatti ha consentito la visualizzazione di sezioni pulite e ha contribuito a rivelare tracce compatibili con la scrittura, dimostrando così il vantaggio dell'applicazione della tecnica XPCT per scoprire e decifrare il testo antico.

Alcuni dei risultati di questa ricerca sono riportati nel seguente articolo accettato per la pubblicazione: *Stabile S., et al.*, **Computational Platform for the virtual unfolding of Herculaneum Papyri**, Sci. Reports.

Abstract

In 1750 a large villa on a hill overlooking Herculaneum and the Bay of Naples was discovered. This villa probably once belonged to the wealthy Roman aristocrat Lucius Calpurnius Piso Caesoninus, a well-known Roman politician, who was a patron of Epicurean philosophers. The villa was lost from history in A.D. 79 in the catastrophic eruption of Mount Vesuvius when it was buried by tons of thick volcanic mud which gradually hardened to a concrete-like consistency.

During villa excavations, workers discovered many important works of art and an impressive library of some 1800 papyri rolls - thus the name Villa of the Papyri. The library consists of a remarkable collection of Epicurean philosophical texts written in Greek, and a lesser number of Latin texts.

Due to the intense heat of the volcanic flow and the pressure exerted by the weight of mud, lava, pumice, and rubble, these rolls are extremely fragile, lost more or less the original cylindrical shape, and the individual sheets stuck together tenaciously.

Since their discovery, numerous efforts have been made to open the carbonized-Herculaneum-papyri and read the priceless information contained in them employing several manual and destructive techniques.

My Ph.D. research work concerns the study of Herculaneum papyri using a non-destructive X-ray technique and a new set of numerical algorithms for ‘virtual-unrolling’.

In particular, I used X-ray-micro-computed tomography (μX-CT) and X-ray Phase Contrast Tomography (XPCT) as powerful non-destructive testing techniques for the full-volume inspection of the papyri, able to give morphological and physical information on the inner structure of the investigated sample. I analyzed three Herculaneum papyri fragments: *PHerc.1103* and *PHerc.1105* belonged to the scroll exterior part, *scorza*, and *PHerc.110* belonged to a papyrus partially unrolled in 1867.

The main purpose of my research work was building a computational platform for the virtual 3D investigation of the Herculaneum papyri fragments. Due to the poor conditions of the fragments, virtual operations on the 3D tomographic images, such as segmentation and flattening of the papyrus sheets, result complicated and require an approach developed specifically for this particular task.

In this thesis, I describe in detail this computational platform, which is the composite result of 3D data digitisation, segmentation, modelling, flattening and texture mapping of papyrus sheets. Following 3D data digitisation, the segmentation step is presented, thanks to which I can digitally identify the single papyrus sheet within the volume. After the sheet surface is modeled using triangular meshing, preferred to other kinds of mesh because it simplifies the math and allows for faster operations. Finally, I focus on the parameterization methods for unfolding sheet with minimum distortion. Once the good parametrization method has been identified, the next step is texturing, i.e., assignment of 3D color information to each point on a 2D mesh. The resulting texture reveals the features of the flattened sheet.

Besides, investigations on different phase retrieval approaches have been performed. I implemented and tested three of the widespread methods to find the best one. Another challenging problem, due to the ring artifacts present in the reconstruction that disturbs the image impression, was resolved through algorithms adapted to this particular case. The artifacts removal process allowed the visualization of clean slices and helped to reveal traces compatible with writing. It has so been demonstrated the benefit of applying the XPCT technique to trace handwriting.

Some of the results of this research are reported in the following paper has been accepted for publication: *Stabile S., et al.*, **Computational Platform for the virtual unfolding of Herculaneum Papyri**, Sci. Reports.

Contents

List of Figures

List of Tables

Chapter 1

History of Herculaneum Papyri

The town of Herculaneum was destroyed by the pyroclastic flows of the erupting Mount Vesuvius in A.D. 79. However, many artifacts and structures were preserved by this same process, until their discovery in the last few centuries. Among the artifacts found there are hundreds of papyrus rolls contain valuable writings of the Greek philosophers of the day, including works of the Epicurean Philodemus. This collection is the only known library of antiquity to have survived to the modern era. Reading the text within has been a challenge to scholars ever since.

In this chapter, the history of Herculaneum papyri is given from their discovery (Section 1.1 and Section 1.2) to the unrolling methods used in the past (Section 1.4).

In Section 1.3 a concise introduction is given to the topic of manufacture process and the use of papyri as writing material and both the bibliological aspects (length and height of the rolls, relationship between written and unwritten space, typology of the columns) and technical libraries (sticometric calculations, titles and annotations) useful to understand how to read such papyri.

1.1 Villa dei Papiri

The *Villa dei Papiri* or *Villa dei Pisoni* is a large building (253 meters in length) located in the north-west of ancient Herculaneum, near the sea.

This Villa has given us artistic treasures, such as bronze and marble sculptures, magnificent frescoes and floors and a unique library of some 1800 papyri rolls, thus the name *Villa dei Papiri*. This book collection has exceptional importance on different levels: librarian, palaeographic, papyrological, historical-philosophical and literary.

Many hypotheses for the attribution of the Villa have been proposed and the question remains, still today, open, engaging many scholars for almost two hundred years.

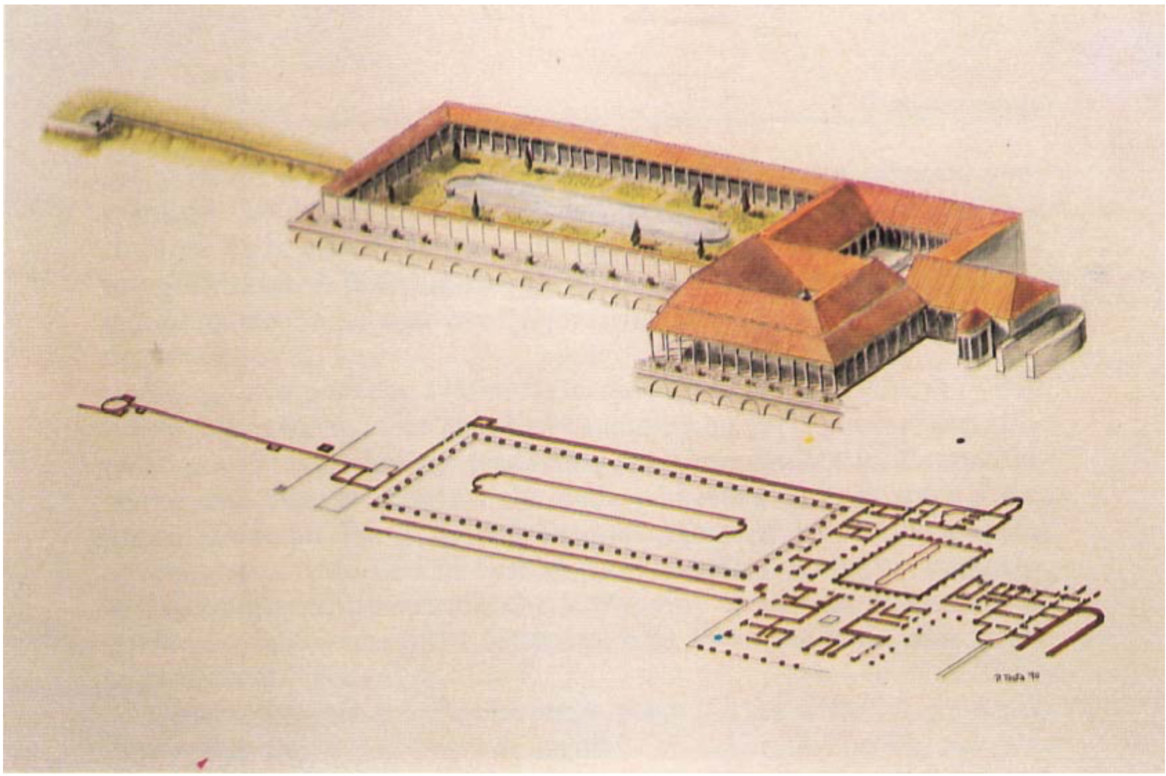

Figure 1.1 Architectural system (Weber plan) and virtual reconstruction of the Villa dei Papiri. Figure adapted from G. Cavallo [21].

The Villa probably once belonged to the wealthy Roman aristocrat Lucius Calpurnius Piso Caesoninus [27], father-in-law of Julius Caesar, an adversary of Cicero and Roman politician in B.C. 58. Piso Caesoninus was a friend of Philodemus of Gadara, a popularizer in Rome around the middle of the 1st century B.C. of the doctrines of the Epicurean philosophers. And it is precisely in the Villa that many epicurean texts have been found.

In A.D. 79 the catastrophic eruption of Vesuvius buried the Villa by volcanic mud that gradually hardened (called *tufo*). Afterwards, in 1631 there was a second eruption that covered the Villa by basaltic lava flow. Today the Villa is buried under a 27-meter layer of volcanic material.

The excavation began towards the end of April 1750, under Charles of Bourbon, directed by the Swiss engineer Karl Weber, with the supervision of the Spanish Roque J. Alcubierre. Thanks to Karl Weber, we know the precise location and also a large part of the architectural structure of the Villa. He created the plans of the building, shown in Figure 1.1 and Figure 1.2. In Figure 1.1 there is the complete architectural layout of the Villa with its ideal virtual reconstruction. The plan shows all the rooms explored and the tunnels built. Figure 1.2

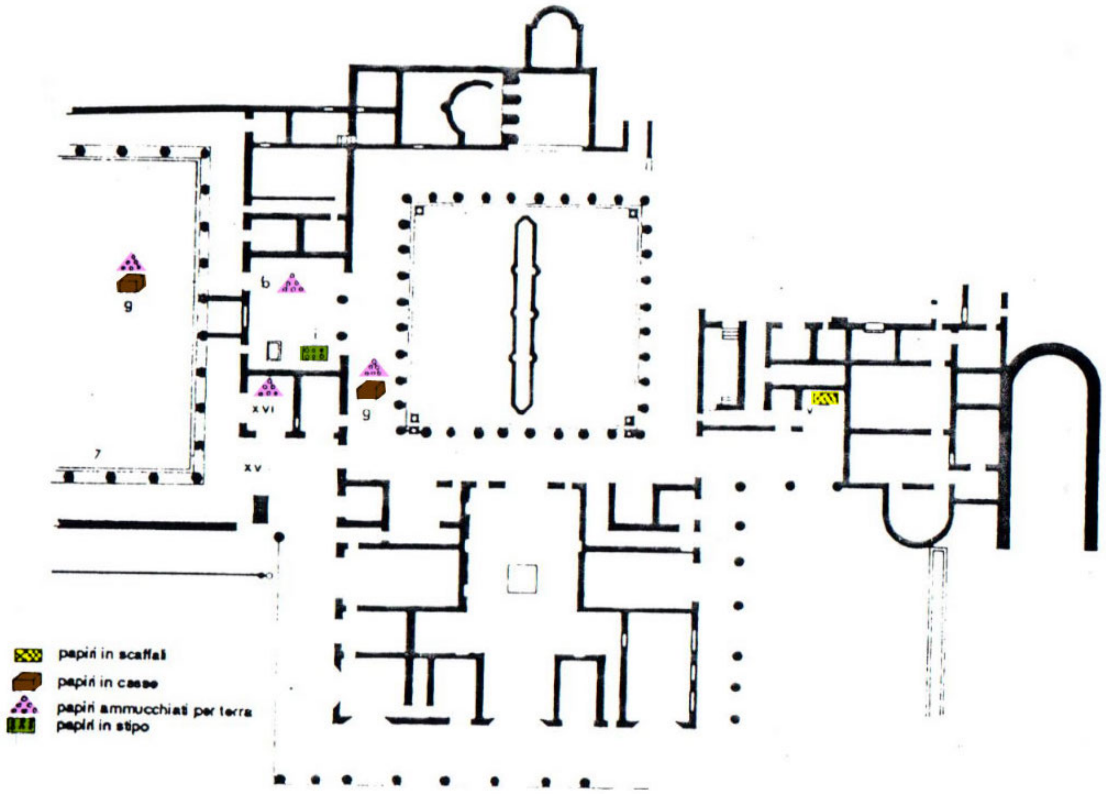

Figure 1.2 Weber plan. The areas of the finds are marked. Figure adapted from G. Cavallo [21].

shows, instead, a part of the Weber plan, where the areas of the finds are indicated with remarkable precision.

In 1761 the excavation was interrupted due to the extremely dangerous gas and the political, administrative and financial difficulties. Other exploration (1986-1987) and excavation (1992-1997) operations were carried out, from which important discoveries emerged.
The operations are never finished, and the Villa is still an active site.

1.2 Discovery of the Villa’s Library

The papyri were found between 19 October 1752 and 25 August 1754 at different times and places. We can have information on the findings of the papyrus thanks to the reports drawn

Figure 1.3 A photos collection of some Herculaneum papyri. The upper panels show whole rolls, while the lower ones show fragments.

up at the excavation time - such as plan of the Villa by Kerl Weber in Figure 1.2 (1764) and *Memorie* of Father Antonio Piaggio (1769-1771) [66] - and to the more recent works - as *Manuale di Papirologia Ercolanese* of Capasso (1991) [17]).

The papyri were found in five different points, marked in the plan of Villa in Figure 1.2.

The first group of scrolls was found from 19 October to the first half of November 1752. About 10 and 12 rolls were found in *i* and *b* of Figure 1.2, respectively. These rolls were mostly Latin. The 10 papyri found in *i* were preserved in a cabinet and it is thought that originally the papyri of the *tablinum* were much more (almost 60 papyri).

Subsequently, on 8 April 1753, in the room adjacent to the *tablinum* (room XVI in Figure 1.2) 11 rolls – completely uncertain whether Greek or Latin- were found. In the same year, from 7 to 21 May, a total of at least 161 rolls – perhaps mostly Greek rather than Latin - were recovered near the quadrangular peristyle and the central column of the rectangular peristyle (point *g* in Figure 1.2). Some of these rolls were preserved in three charred wooden box and others piled on the ground.

From 24 February to 25 August 1754 about 840 papyri were found in a small quadrangular environment (room V in Figure 1.2), placed on shelves. These rolls were mostly Greek and were no longer intact but reduced to fragments. Finally, on 8 May 1759, a scroll in the rectangular peristyle (point 7 in Figure 1.2) was found by chance.

Many other papyri were lost, the diggers did not notice that they were papyrus rolls. They were mistaken for fragments of charred wood and thrown away. Therefore, a certain number of rolls, probably not too high (30 or 50), was destroyed because it was considered a material without importance.

It is likely that the rest of the library is still buried in the unexplored parts of the Villa.

Subjected to a very high temperature, higher than 300°C [95], the Herculaneum rolls underwent a partial combustion process. The carbonization process has neutralized climatic and environmental factors such as humidity, temperature variations, microorganisms, which under normal conditions have destructive effects on papyrus paper. The partial combustion, if on the one hand, has allowed the conservation of the rolls, on the other, it has made them extremely fragile with the consequent risk of irreparable cracks and losses.

Now, Herculaneum papyri are housed in the *Officina dei Papiri Ercolanesi* at the *Biblioteca Nazionale* in Naples (Italy), Figure 1.3.

1.3 Greek and Latin Papyri

Library of the Villa is exclusively divided into two separate sections: one Greek and one Latin [20].

In this section, we discuss the bibliological aspects (length and height of the rolls, relationship between written and unwritten space, typology of the columns) and technical libraries (sticometric calculations, titles and annotations) for - both Latin and Greek - Herculaneum papyri. Before, we put our attention on the basic principles of manufacture and the use of papyrus plant as writing material.

1.3.1 Papyrus manifacture

Leach and Tait [49] give a complete discussion about papyrus plant structure, manufacture process and its use as writing material. Briefly, we give an overview of these topics.

For the preparation of the papyrus sheet the lower, and therefore wider, part of the *Cyperus papyrus L.* stem was used because it contains the most pith. The pith was cut longitudinally into thin strips and 20-30 centimeters long. These strips were laid side by side to form one layer; the second layer strips were then placed on top at right angles to form a second layer. The whole was pressed with a roller to form a homogeneous sheet thanks to the natural sap contained in the plant. Then the sheet was put to dry in the sun. In this way rectangular sheets were obtained (called in Greek *kòllema*, plural: *kollemata*).

Individual sheets of papyrus were then joined together with a glue of water and flour, overlapping a few centimeters (1–5 cm). These junctions between the sheets are called *kolleseis*.

The preparation ended with the sanding of the sheet with a stone, which was rolled up to form the roll. The scroll had a crisscross pattern, where we can distinguish an inside, called *recto*, where commonly the text was written (writing surface), and an exterior, *verso*, useful for rolling the sheet (supporting layer).

In the Herculaneum rolls, it is difficult to distinguish the signs of the *kolleseis* because of the good quality of the papyrus material, the state of carbonization, and the presence of vertical bending caused by the pressure of the lava mud. Moreover, it has been noted that the *kolleseis* are crossed by writing. Thus, it was written on rolls composed of *kollemata* already joined together and not on individual sheets [17].

1.3.2 Greek Papyri

The papyrus containing Greek texts are all high and medium-high formal books.

The oldest nucleus of the Greek sector is a remarkable collection of texts of Epicurean philosophers, such as Epicuro, Demetrio Lacone, Metrodoro e Carneisco, datable up to the 3rd century B.C. [19].

An analysis of the Greek papyrus writings shows that the most consistent collection of the works is from the Epicurean philosopher Philodemus of Gadara (in present day Jordan), dating back to the 1st century A.C.. These are works of stereography, ethics, music, and rhetoric dating back to the beginnings of the philosophical activity of Philodemus (circa 75-50 BC); also, *Poetica*, works of ethics, theology, political ideology and gnoseology dating back to maturity (around 50-25 BC).

Even after the death of Philodemus, the Greek library was enriched with other Epicurean materials, attesting that in the Villa the interest in this doctrine did not end with the Philodemic era.

FORMAT

The Greek Herculaneum materials had a length around 6-9 meters without exceeding 10 meters and an average height of 21-22 cm. The Herculaneum scribes maintained the height and width of the columns constant throughout the roll. This means that in the same roll, the relationship between written space and unwritten space was respected. On the contrary, not much attention was paid to the organization of the columns; variations in the number of rows in the various columns and the number of letters in the various rows of the same column could be present. In the Herculaneum rolls, a strict alignment of the lines on the left is observed; it is a possible sign of the high quality of the artifacts [19]. The Herculaneum column covers $3/4$ or $4/5$ of the height of the papyrus. On average there are 30-34 rows in columns that are 5-6 cm wide. The margins (lower and upper) occupy $1/4$ or $1/5$ of the height of the roll.

Each roll ended with the last *kollema* (*eschatokollion*) which was not written or at most contained an indication of the title. It was applied, with the internal fibers in a horizontal direction, after the last column to avoid fraying. In some cases, a small papyrus band (just 1 cm wide) was applied as reinforcement to the end of the roll.

TITLES AND STICOMETRY

The titles are usually at the end of the text. Since in all rolls the initial *kollema* (*protokollon*) has been lost, we do not if titles were also at the beginning. The title, usually arranged symmetrically on a single line, includes:

- author's name,
- title of the work,
- book number, followed by the subtitle of the book,
- tome number,
- possible annotation of the nature of the text.

Below the title, usually, there is the number of lines in which the text was articulated, i.e., the stichometrical indication. These notes were made according to the acrophonic system, whereby: $I = 1$; $\Pi = 5$; $\Gamma^{\Delta} = 10$; $\Pi_{\Delta} = 50$; $H = 100$; $\Gamma^{H} = 500$; $X = 1000$. In some cases, the sticometric annotation is marginal, on the left side of the columns at regular intervals. The marginal notes were indicated by the use of the capital letters of the alphabet placed between two horizontal or oblique bars. Sometimes, they were also or accompanied or interspersed with points.

INK AND WRITING INSTRUMENTS

Herculaneum ink, like the one generally used for papyrus in the ancient world, is black, made with gum and coal juice dissolved in water. According to Fackelmann [77] this ink was less resistant than that used by the Egyptians, obtained from a mixture of gum and carbon black (particles of coal obtained by burning organic substances) dissolved in water. This would explain, according to Fackelmann [77], because today in the Herculaneum materials we often note the total or partial disappearance of writing, which did not resist the chemical reactions the volumes underwent mostly during the eruption and in also the almost seventeen centuries during which they remained buried.

The instrument used to write was a cane with a hard and thin tip. With this type of writing tool, it was impossible to get full strokes and the final text was static.

1.3.3 Latin Papyri

The texts of the Latin sector are difficult to read and know their content. This is due to the relatively small number of papyri and, above all, to the greater state of degradation in which they are found. The exceptions are few poetic, political, and juridical texts have been found.

FORMAT

We have no data on the length of the Latin papyrus, due to the poor state of preservation. The height was greater than the Greek rolls; it could reach 28 cm. The width of the column is around 5-6 cm, much smaller than the Latin papyrus (17 cm).

TITLES AND STICOMETRY

The structure of Latin papyrus titles was similar to that seen previously for Greek ones.
The stichometrical calculation, on the other hand, is absent.

INK AND WRITING INSTRUMENTS

The ink of the Latin scribes was similar to the ink of the Greeks; what differentiates them is the writing instrument. The Greek copyists, as we have seen, used a thin and hard tip calamus, while the Latins used a flexible and wide tip. With this type of tip, it was possible to contrast full and thin lines, giving the writing a relief and a rhythm absent in the Greek rolls. With a flexible and wide tip, it is also possible to obtain *chiaroscuro*, an element characterizing Latin papyrus.

1.4 Methods of unrolling

The problem of opening the Herculaneum papyri begins with their first discovery. The greatest obstacle is the high degree of carbonization in which the papyri are found, which made them extremely fragile and some, with time, petrified.
Under the weight of the pyroclastic material, for about seventeen centuries, the papyri lost

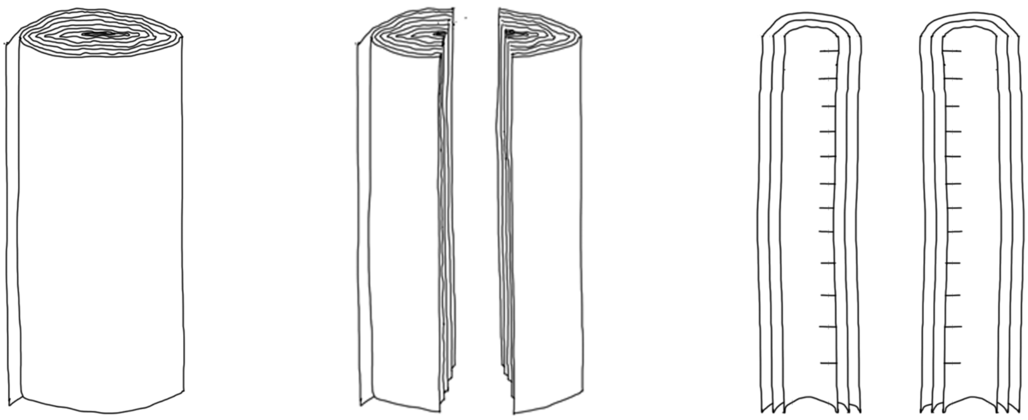

Figure 1.4 Scheme of *total scorzatura*.

more or less the original cylindrical shape: compressed, crushed, shortened and not a few broken into two or more pieces. Furthermore, as an effect of carbonization and compression, the individual sheets of the rolls have stuck together tenaciously.
The opening can be further hindered by their high porosity; the air makes the fibers even weaker and less treatable.

The first attempts at opening the papyri consisted of treating them with hydroalcoholic and glutinous solutions to give elasticity to the carbonized fibers [17]. These solutions were applied in different ways: by completely immersing the papyri in them; spreading them with a brush only on the surface; wrapping the papyrus in damp cloths; pouring them from the top of the papyrus, so that they penetrated through the layers, causing their detachment. These attempts, rather than favoring the softening and distension of the carbonized papyrus surface, cause their crushing or crumbling. Equally unsuccessful were the experiments of Raimondo di Sangro, Prince of Sansevero, who sent more than four rolls into pieces with mercury [17].

Another technique, which led to the destruction of hundreds of scrolls, was the (total and partial) *scorzatura* [2] practiced by Camillo Paderni, custodian of the *Museo ercolanese di Portici* in 1750. This technique consisted of five phases:

1. the papyrus was wetted with hydroalcoholic solutions, solvents or glutinous;
2. with a knife, the papyrus was cut:
   - longitudinally in two half-cylinders of the same thickness, for the *total scorzatura* (Figure 1.4);

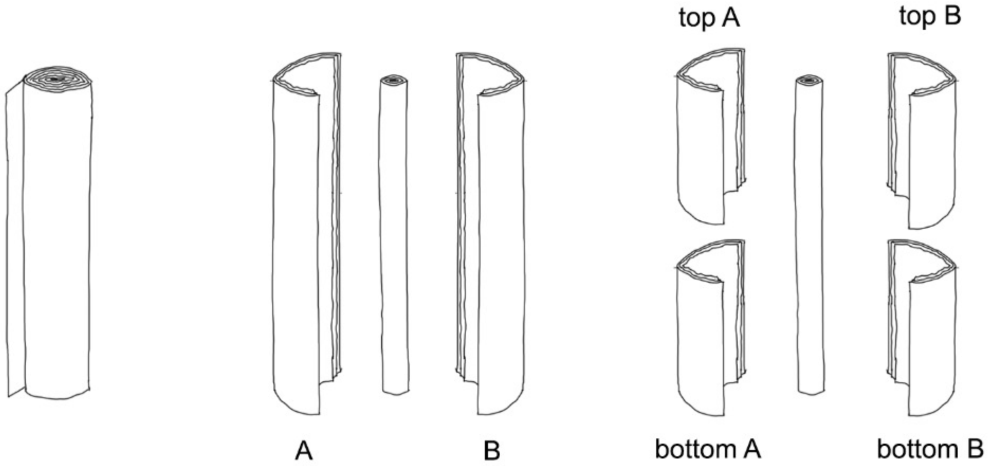

Figure 1.5 Scheme of *partial scorzatura*.

- longitudinally with two parallel cuts, sometimes also with two central cuts perpendicular to the height of the roll, for *partial scorzatura* (Figure 1.5);

3. until a substantial part of the text was found, the inside of the two (or four) parts were scraped;

4. the text was transcribed, and the papyrus parts were scraped to re-emerge the underlying layer;

5. the outer most residual parts (called *scorze*) were reinforced with pieces of cloth glued to the outside, without writing, with a chinese painting.

In *total scorzatura*, the papyrus was almost destroyed; only the outer sheets (*scorze*) were saved. The inner part of the roll, including the final title, crumbled because it is very fragile because it is less compact. On the contrary, in the *partial scorzatura*, only the external parts were peeled. The *midollo* (the central part of the papyrus), in addition to the two or four rinds, were saved.

There is also an editorial issue: for the papyrus unrolled by *scorzatura*, we have only the hand-drawn facsimiles. The people who transcribed the text were not scholars and did not know Greek, so in these documents, there are errors.

In 1753, father Antonio Piaggio, Latin writer and guardian of the miniatures of the *Biblioteca Vaticana*, invented the famous machine that takes its name (Figure 1.6).

Piaggio's machine, which remained in operation until 1900, was able to open *midollo*, left by Paderni [2, 17]. The original structure of Piaggio's machine provided a horizontal worktop

Figure 1.6 Piaggio’s machine.

over the wooden holder using a screw, which had the function of adjusting the height of the top as needed. At the center of the worktop, there were two steel bars, on which a stell half-moon was placed. In the concave part, the papyrus roll was placed. This holder was also supported at the ends by two ribbons tied to an upper axis with violin keys to position the papyrus without touch it.

The outer edge of the *midollo* (i.e., the strip without writing) was wetted with glue. This glue served to soften and detach the sheets, but also, to glue small pieces of sheep or beef intestine. On the reinforced surface silk threads were attached with the same glue. These were connected, using hooks, to the upper part of the machine. The silk threads were slowly pulled one after the other so that the lined papyrus strip separated from the roll. When, through traction, the unrolled papyrus had reached the height of the frame, it was wind back around a roller.

This procedure took a very long time: with four or five hours of work, no more than a finger of papyrus width was possible to wad and detach.

The Piaggio's machine could be applied to papyrus rolls with non-compact sheets, so it was necessary to delete the external part of the papyrus roll. Therefore, *partial scorzatura* was a preliminary step, even if destructive, for the unrolling. From here another editorial issue arises about cataloging: *scorze* and the corresponding *midollo* were opened at different times and then, recorded with different numbers [2, 17]. To overcome this problem, to separate the compact papyrus sheets, many complex techniques were tested. Some techniques involved the use of chemicals that destroyed every trace of writing [2, 17].

From 1965 to 1970, Anton Fackelmann, a Viennese librarian, unrolled and restored the Herculaneum papyri. He pointed out three substantial limits to the use of Piaggio's machine: mechanical traction had in many cases caused the laceration of the layers; the glue used had hardened the papyrus making it inflexible; the skin, vulnerable to temperature changes, would have damaged the papyrus over time [2].

Fackelmann worked on dark brown and hard papyrus, but whose layers were easily identifiable and the writing still present. He first gave elasticity to papyrus using papyrus juice and then subjected them to the heat of a lamp [2, 17]. Electromagnetic fields of different polarity were created between the layers which, due to the presence of carbon produced by carbonization, acting as electrodes, began to come off. With the tweezers, the real detachment of the sheets was practiced. The unrolled parts were hermetically sealed between two glass. This arrangement prevented the deposit of dust or other external agents on the surface of the papyrus but made it difficult to read and exposes the papyrus to another set of physical stresses including the possibility that the glass will simply crush the parchment to powder [2, 17].

From 1983 to 1990 a Norwegian team, consisting of Wendelbo, Fosse, Stormer, Jensen, led by the philologist Knut Kleve, devised a method based on the use of acetic acid, gelatin, and water. The doses of these three elements never fixed but varied according to the degree of carbonization and porosity of the papyrus [2, 17]. The contours of the layer were identified, with the microscope. The glue was spread on the unwritten part of the layer. The glue, once dried, causes the papyrus sheet to detach from the underlying layers [2, 17]. Then, with the use of a metal tweezer, the sheet was removed slowly. The unrolled layer was glued onto a sheet of Japanese paper with the same glue used for unwinding and kept in a metal frame. The various phases of the operation were accompanied by photographs which today document the original position of the pieces.

Thanks to the use of these methods, the unrolled rolls have returned important Greek and Latin texts not received by us through the medieval manuscript tradition. Unfortunately, even under the best conditions, much of the text was lost during the unrolling process: very few unrolled parts of papyrus gave a considerable number of continuous and legible columns without large damages. Even after papyri are successfully unrolled, there are still damages that can come from exposing the layers of a scroll to light and air: fading ink, color changes, weakening the structure of papyrus, and the oxidization of ink that causes papyrus breakdown. Carbonization has made it very difficult, sometimes impossible, to unroll and restore papyrus, imposing the search for more complex, non-invasive and non-destructive techniques.

Chapter 2

X-ray Tomography

X-rays have been used for imaging since they were first discovered by the German physicist Wilhelm Conrad Roentgen in 1895 [72]. He demonstrated that the X-ray – X for unknown - could pass through opaque objects where light cannot. The potential of using this characteristic feature for the imaging was immediately recognized, and a multitude of medical, but also industrial and cultural heritage, applications quickly developed.

Decades of research have followed since their discovery, and it is now known that X-rays are a form of electromagnetic radiation emitted by charged particles (usually electrons), with wavelengths in the range of 0.01-10 nm and energies in the range 0.1-100 keV. The energy of each photon is proportional to its frequency, namely:

$$E = h\nu = \frac{hc}{\lambda} \tag{2.1}$$

where $h = 6.63 \times 10^{-34} Js$ is Planck's constant, $c = 3 \times 10^8 m/s$ is the speed of light, and λ is the wavelength of X radiation. By the reduced wavelength, the associated energy is quite high and enable X-rays to pass through matter, unless an interaction on the atomic level occurs, in which case X-rays can be absorbed or scattered. In the energy range of interest for X-ray imaging, there are three mechanisms by which these processes occur:

1. <u>the photoelectric absorption</u>: the photon is completely absorbed by an inner shell electron, which is released from its shell. The kinetic energy of the ejected electron is then given by the difference between the energy of the initial photon and the binding energy of the electron in the atom. The vacant electron position is then filled by an electron of the outer shell, a transition that results in the emission of radiation with energy equal to the energy difference of the two shells, and is therefore characteristic to the atom. In some cases, the excess energy can be emitted by liberating an outer

shell electron, which is then called the Auger electron. The incoming photon energy must be greater than the electron binding energy.

2. the incoherent scattering (also called inelastic or Compton scattering): the photon interacts with an electron (assumed to be at rest) and changes direction, so part of its energy is transferred to the electron. The energy change can be calculated by considering the conservation of both energy and momentum during the interaction. As a result, the electron is ejected, and the photon is scattered with a reduced energy.

3. the coherent scattering (also called elastic or Rayleigh scattering): the photon interacts with the whole atom, causing the oscillation of the entire electron cloud. The latter then emits radiation with the same energy as that of the incident photon, which changes the propagation direction.

In general, the relative contributions of these interactions vary depending on the sample material and X-ray energy.

In this chapter, the background of X-ray physics and conventional X-ray tomography is provided.

2.1 X-ray refraction index

Imaging and tomographic techniques are based on the physical phenomenon of the interaction of X-rays with matter. The basic idea is to detect the transmitted X-rays passing through the matter.

The behavior of X-rays as they travel through an object is generally described with the complex refractive index, obtained in Appendix A. For X-rays the refractive index ($n(\omega)$) is very close to unity and therefore it is often express as [4]:

$$n(\omega) = 1 - \delta + i\beta \tag{2.2}$$

where δ and β, using the results obtained in Appendix A and comparing eqs. (A.15) and (2.2), can be expressed as:

$$\delta = \frac{n_a r_e \lambda^2}{2\pi} f_1^0(\omega) \tag{2.3}$$

$$\beta = \frac{n_a r_e \lambda^2}{2\pi} f_2^0(\omega) \tag{2.4}$$

where n_a is the number density (atoms or electrons per unit volume), r_e is the electron radius, λ the X-rays wavelength, and $f_1^0(\omega)$ and $f_2^0(\omega)$ are the real and imaginary parts of the complex atomic scattering factor (see Appendix A for more details), respectively.

In eq. (2.3) we have the expression of the real part of the refraction index δ, known as refractive index decrement, it describes phenomena like refraction, diffraction, interferences and effects related to the phase shifts of the electromagnetic wave in the matter. While in eq. (2.4) the imaginary part of the refraction index β, also called absorption index, which is linked to the absorption of X-rays into the matter. The absorption index is related to the mass attenuation coefficient μ, through the relation:

$$\mu = \frac{4\pi\beta}{\lambda} \tag{2.5}$$

The mass attenuation coefficient depends on the cross-section σ and the electron density ρ_e of the material crossed:

$$\mu = \sigma\rho_e \tag{2.6}$$

Through the cross section, μ depends on the photons energy E. In the case of more atomic interactions come into play, the total cross-section is the sum of the cross-sections of the individual processes:

$$\sigma_{tot}(E) = \sigma_{abs}(E) + \sigma_{coh}(E) + \sigma_{inc}(E) \tag{2.7}$$

where $\sigma_{abs}(E)$ is the photoelectric cross-section, $\sigma_{coh}(E)$ is the coherent cross-section, and $\sigma_{inc}(E)$ is the incoherent cross-section.

To see the effect of the refractive index, one compares two monochromatic plane waves traveling in the **z**-direction,

$$\mathbf{E}(z,t) = \mathbf{E}_0 \exp\{i(kz - \omega t)\}, \tag{2.8}$$

one that propagates in vacuum (black line) and one in a medium (blue line), as we show in Figure 2.1.

From Maxwell equations results that the refraction index satisfies the dispersion relation:

$$k^2 = \frac{\omega^2 n^2}{c^2} \tag{2.9}$$

so the wave in vacuum (with $n = 1$) can be described as:

$$\mathbf{E}(z,t)_{vacuum} = \mathbf{E}_0 \exp\{i(k_0 z - \omega t)\} \tag{2.10}$$

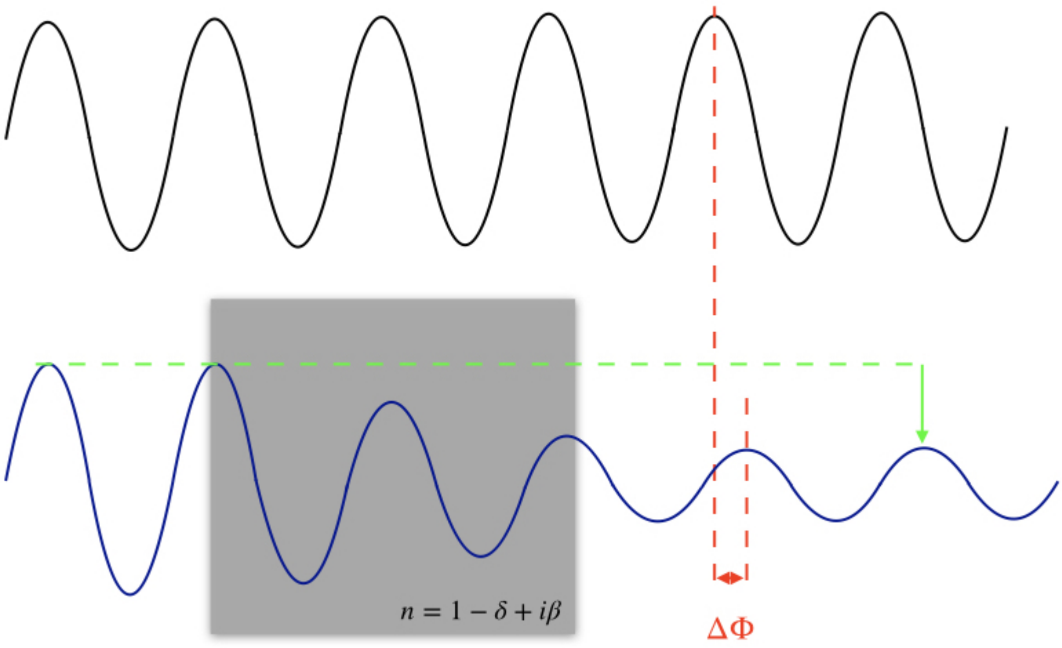

Figure 2.1 Comparison of two monochromatic plane waves traveling in a vacuum (black line) and in a material with refractive index n (blue line). The latter is longitudinally shifted (phase shift, $\Delta\Phi$) and has a loss in amplitude (attenuation).

while the wave inside the material (with complex index of refraction (2.2)) can be described as:

$$\mathbf{E}(z,t)_{matter} = \mathbf{E}_0 \exp\{i(k_0 z - \omega t)\} \exp\{-ik_0\delta z\} \exp\{-k_0\beta z\} \tag{2.11}$$

where $k_0 = \omega/c$ is the wave vector in vacuum. In eq. (2.11):

- the first term represents the wave in a vacuum (eq. (2.10));
- the second term represents the modified phase shift ($\Delta\Phi$, indicated by red lines in Figure 2.1) due to interaction with the material; in general, the phase shift can be written as:

$$\Delta\Phi(x,y) = -\frac{2\pi}{\lambda}\int \delta(x,y,z)\,dz \tag{2.12}$$

- the third term represents the decay of the wave amplitude in the medium due essentially to the photoabsorption (indicated by green lines in Figure 2.1). This amplitude attenuation can be written as:

$$\mu_t(x,y) = \frac{1}{2}\int \mu(x,y,z)\,dz = \frac{2\pi}{\lambda}\int \beta(x,y,z)\,dz \tag{2.13}$$

2.2 Transmission function

The idea of X-ray imaging is to record what comes out on the other side of the sample when X-rays passed through this. As described above, the wavefront will change inside the sample due to the interaction with matter. To be able to get quantitative information about the sample measured, we need to know what happened to the X-ray wavefront as it propagated from the source to the detector.

We know that in a material the electric field $\mathbf{E}(x,y,z,t)$ satisfies equation:

$$\left(\frac{n^2}{c^2}\frac{\partial^2}{\partial t^2} - \nabla^2\right)\mathbf{E}(x,y,z,t) = 0 \tag{2.14}$$

It is easy to verify by direct substitution that the general solution of eq. (2.14) is a monochromatic wave of frequency $\omega = 2\pi c/\lambda$ with wavelength λ:

$$\mathbf{E}(x,y,z,t) = \mathbf{E}_\omega(x,y,z)\exp\left(-i\omega t\right) \tag{2.15}$$

If eq. (2.15) is a solution of eq. (2.14), this implies that $\mathbf{E}_\omega(x,y,z)$ must satisfy the so-called *Helmholtz equation*:

$$\left(\nabla^2 + k^2 n^2\right)\mathbf{E}_\omega(x,y,z) = 0 \tag{2.16}$$

where $k = 2\pi/\lambda = \omega/c$.

For X-ray, the complex refraction index n (see Section 2.1) numerically, deviates only slightly from unity and δ and β being extremely small. For example, for light elements and at X-ray energies in the range $10-100keV$, the refractive index decrement δ can be quoted in $10^{-4}-10^{-7}$ range, while β is in the order of $10^{-8}-10^{-18}$. So the real part of n turns out to be close to 1, this implies that the variations of the X-ray propagation direction within the matter are negligible. Under these conditions, we have propagation in paraxial approximation and $\mathbf{E}_\omega(x,y,z)$ can be rewritten as:

$$\mathbf{E}_\omega(x,y,z) = \mathbf{E}_0(x,y,z)\exp\left(ikz\right) \tag{2.17}$$

where z represents the wave propagation direction. Solving the Helmholtz equation (2.16) for the wave (2.17) is obtained:

$$\frac{\partial^2\mathbf{E}_0}{\partial x^2} + \frac{\partial^2\mathbf{E}_0}{\partial y^2} + \frac{\partial^2\mathbf{E}_0}{\partial z^2} + 2ik\frac{\partial\mathbf{E}_0}{\partial z} + (n^2-1)k^2\mathbf{E}_0 = 0 \tag{2.18}$$

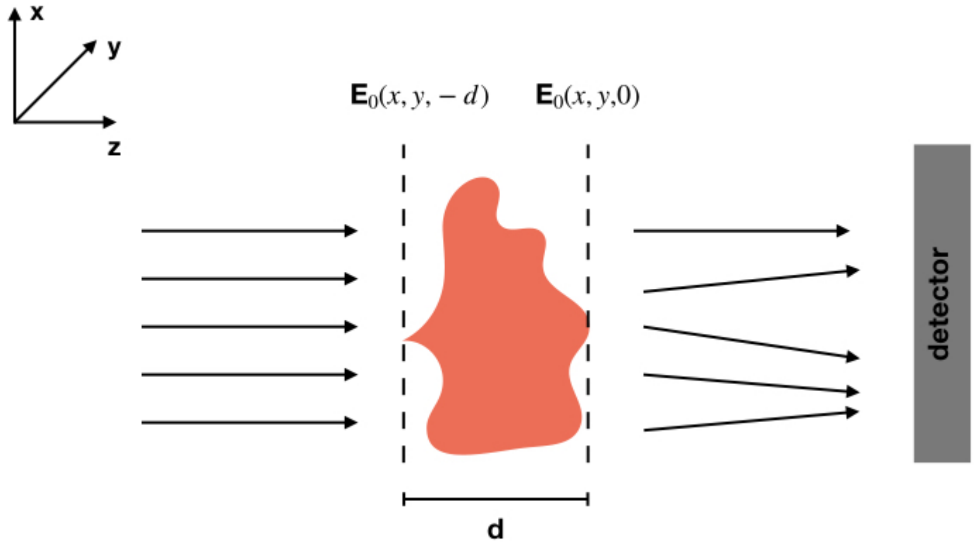

Figure 2.2 Illustration of the projection approximation: an incoming wave $\mathbf{E}_0(x,y,z)$ will be changed by the specimen, such that absorption and phase shift will be cumulated in an exit plane $\mathbf{E}_0(x,y,0)$ without accounting for internal scattering.

Since the amplitude is weakly variable in the propagation direction, the second derivative can be neglected and eq.(2.18) becomes:

$$\left(2ik\frac{\partial}{\partial z}+\Delta_\perp+(n^2-1)k^2\right)\mathbf{E}_0=0 \tag{2.19}$$

where $\Delta_\perp=\frac{\partial^2}{\partial x^2}+\frac{\partial^2}{\partial y^2}$ is the Laplacian in the xy plane, i.e., the transverse Laplacian.

Eq. (2.19) can be solved imposing the *projection approximation* or *thin objects approximation*. The *projection approximation* manifests itself in the assumption that scattering effects inside the specimen can be neglected, i.e., phase shift and absorption are completely determined by considering interactions with infinitesimal thin samples. For eq. (2.19) this means that the effect of the transverse Laplacian $\Delta_\perp$ will be much smaller than that of the axial derivative ∂z and therefore becomes:

$$2ik\frac{\partial \mathbf{E}_0}{\partial z}+(n^2-1)k^2\mathbf{E}_0=0 \tag{2.20}$$

whose solution has the following form:

$$\mathbf{E}_0(x,y,z) = T(x,y)\mathbf{E}_0(x,y,0) \tag{2.21}$$

where $\mathbf{E}_0(x,y,0)$ is the wave incident on the sample, $\mathbf{E}_0(x,y,z)$ is the wave exiting the sample and $T(x,y)$ is the so-called *transmission function* of the object:

$$T(x,y) = \exp\left(ik\int\frac{n^2-1}{2}dz\right) \tag{2.22}$$

with integral evaluated at full extension of the object along the z-direction. But $n = 1-\delta+i\beta$ and neglecting the second-order terms:

$$\frac{n^2-1}{2} = \frac{(1-\delta+i\beta)^2-1}{2} \approx -\delta+i\beta \tag{2.23}$$

Replacing eq. (2.23) in eq. (2.22):

$$\begin{aligned} T(x,y) &= \exp\left[-k\int\beta(x,y,z)\,dz - ik\int\delta(x,y,z)\,dz\right] \\ &= \exp\left[-\mu_t(x,y)\right]\exp\left[i\phi(x,y)\right] \\ &= A(x,y)\exp\left[i\phi(x,y)\right] \end{aligned} \tag{2.24}$$

The transmission function describes the absorption ($A(x,y)$) and phase shift ($\phi(x,y)$) inside the sample. If the interactions imparted by the object are assumed to be sufficiently weak that $\mu_t(x,y)$ and $\phi(x,y)$ may be considered small respect to one, we can Taylor expand the expression of $T(x,y)$ to the first order:

$$T(x,y) = \exp(-\mu_t(x,y)+i\phi(x,y)) \approx 1-\mu_t(x,y)+i\phi(x,y) \tag{2.25}$$

Therefore, the transmission function explicitly shows the components of absorption and phase shift of the wave due to interaction with the sample.

2.3 Absorption imaging and tomography

When an X-ray beam passes through matter, it undergoes attenuation via the processes of scattering and absorption. The amount of decrease in intensity of the X-ray beam depends upon two factors, the depth of penetration (r) and the mass absorption coefficient μ, which depends on the energy of X-ray photons and the sample composition and density (see eq.

(2.5)). Quantitatively it can be described by attenuation law, knows as the Bouger-Lambert-Beer law:

$$I = I_0 e^{-\mu r} \tag{2.26}$$

where I and I_0 are the emerging and incident intensities of X-ray beam, respectively. The above definition is applicable under conditions of monochromaticity, narrow beam geometry, and a homogeneous object. When an inhomogeneous object is irradiated by a beam, hence the attenuation coefficient is a function of x and y, i.e., $\mu(x,y)$, the eq. (2.26) is modified:

$$I = I_0 e^{-\int \mu(x,y)\,dr} \tag{2.27}$$

where dr is an element of length along the ray.
The absorption imaging consists in measuring the number of photons emitted by the source and the number of photons transmitted throughout the sample. For the reconstruction of the attenuation coefficient values, the measured intensity data must first be linearized. Define the measured attenuation A, also referred to as log-corrected data, by

$$A = -\ln\left(\frac{I}{I_0}\right) = \int \mu(x,y)\,dr \tag{2.28}$$

Therefore the absorption imaging delivers a map of $\mu(x,y)$, i.e., the modulus of the transmission function, while the information about the phase is lost. The image formation is based on the partial absorption of the radiation, i.e., dense structures absorb more radiation than lighter elements.

The eq.(2.28) displays a single 2D image (radiograph) where overlapping structures can not unambiguously be discerned. One method to overcome this limitation is X-ray tomography, in which several radiographs at the different angular positions of the sample is used to obtain a 3D volume.
Consider the schematic shown in Figure 2.3 in which the object is rotate around vertical axis z and it is illuminated by a parallel X-ray beam. Here, (x,y,z) describes the stationary frame of reference, and (x',y',z') is the sample frame of reference, and they are related as:

$$\begin{cases} x' &= x\cos\theta + y\sin\theta \\ y' &= -x\sin\theta + y\cos\theta \\ z' &= z \end{cases}$$

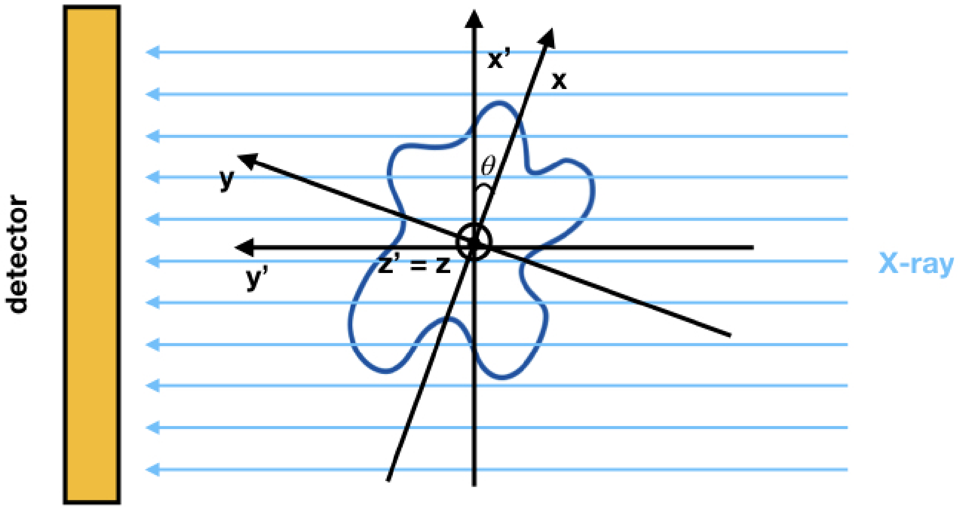

Figure 2.3 The sample coordinate system (x', y', z') is rotate by the angle θ with respect to the deterctor system (x, y, z). The sample is illuminated in the direction along y'.

Eq. (2.28) can be rewritten as a series of integral:

$$p_\theta(x') = -log\left(\frac{I_\theta}{I_0}\right) = \int \mu(x', y')\,dy' \tag{2.29}$$

Using the Dirac-delta function, the eq. (2.29) can be rewritten as:

$$p_\theta(x')) = \iint_{-\infty}^{+\infty} \mu(x,y)\delta(x\cos\theta + y\sin\theta - x')\,dx\,dy \tag{2.30}$$

The function $p_\theta(x')$ as a function of x' for a given value of rotational angle θ, defines the *projection*. A projection is called also *ray-sum* because represents the sum of ray integrals at a different offset from the origin that forms an angle θ.

For a given z the set of projections over 180° is the *Radon transform* of function $\mu(x,y)$. It is also known as the sinogram of $\mu(x,y)$.

In a parallel-beam geometry, 180° is sufficient to represent the Radon trasform since:

$$p_\theta(x')) = p_{\theta+\pi}(-x')) \tag{2.31}$$

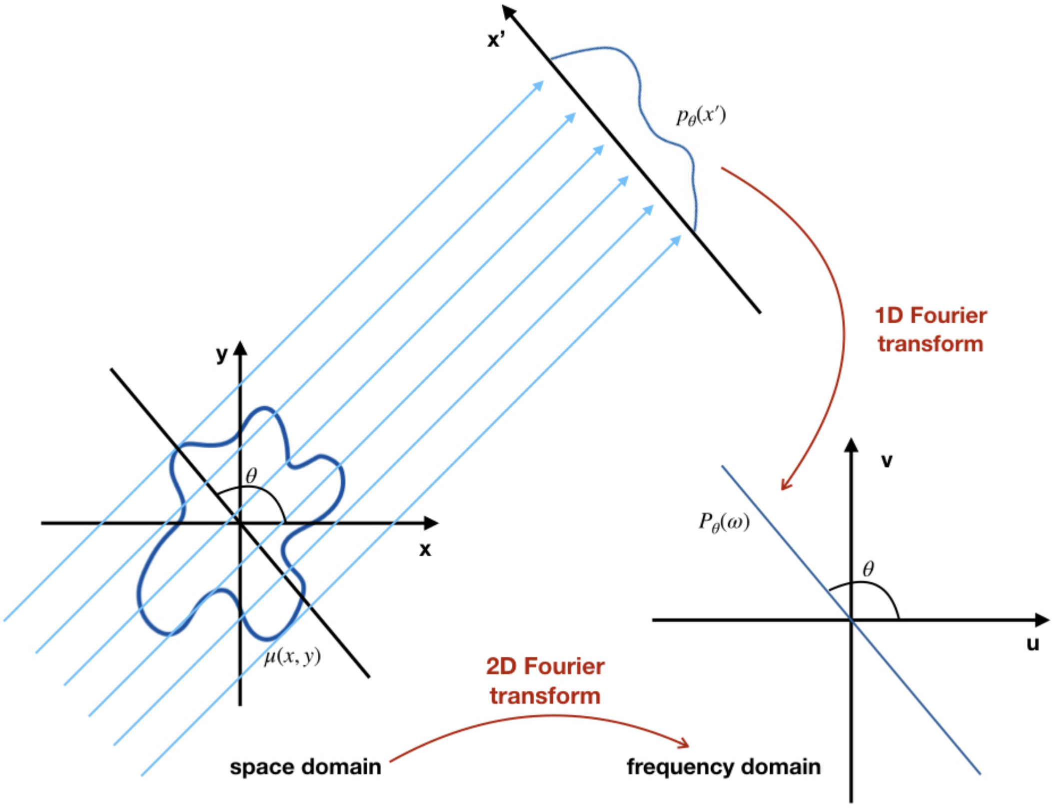

Figure 2.4 Schematic illustration of the Fourier slice theorem. The Fourier tranform of a projection at the angle θ is equal to a slice at angle θ through the Fourier frequency space.

Hence the inverse of the Radon transform can be used to reconstruct the original material property $\mu(x,y)$ of a sample from the projection data obtained as the output of tomographic scan. There are several techniques by which the inverse transform can be calculated, such as the *Filtered Back Projection* (FBP) and *Algebric Reconstruction Technique* (ART) [44]. The most common inversion scheme is the FBP because it provides a good compromise between image quality and calculation time. The FBP is a combination of filtering and integration and it is derived in Section 2.5. It is based on the *Fourier slice theorem*, which is established in Section 2.4.

2.4 Fourier slice theorem

The *Fourier slice theorem* states that the one-dimensional (1D) Fourier transform $P_\theta(\omega)$ of projection $p_\theta(x')$ in the θ direction, is equal to the slice through the origin in the same direction θ of the two-dimensional (2D) Fourier transform of the object function $\mu(x,y)$

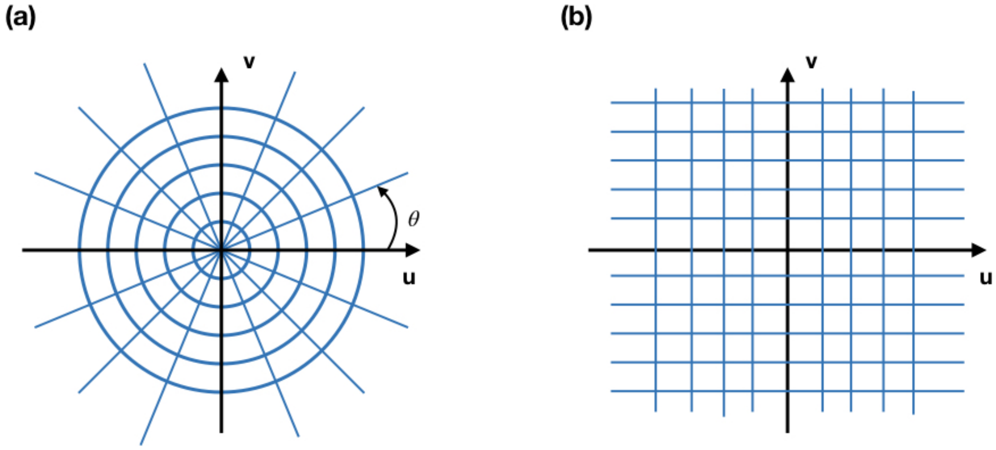

Figure 2.5 (a) A sampling of the Fourier domain with a limited number of projection; (b) Resampling of the Fourier domain into a rectangular grid.

(Figure 2.4) [44]. The validity of the *Fourier slice theorem* can be easily be verified. The 2D Fourier transform of $\mu(x,y)$ is given by:

$$\tilde{\mu}(u,v) = \mathscr{F}\{\mu(x,y)\} = \int\int_{-\infty}^{+\infty} \mu(x,y)\exp\{-i2\pi(ux+vy)\}\,dx\,dy \tag{2.32}$$

Furthermore, the 1D Fourier transform of $p_\theta(x')$ is given by:

$$P_\theta(\omega) = \mathscr{F}\{p_\theta(x')\} = \int_{-\infty}^{+\infty} p_\theta(x')\exp\{-i2\pi\omega x'\}\,dx' \tag{2.33}$$

Substituting eq. (2.30) into eq. (2.33) results in:

$$P_\theta(\omega) = \int\int_{-\infty}^{+\infty} \mu(x,y)\exp\{-i2\pi\omega(x\cos\theta + y\sin\theta)\}\,dx\,dy \tag{2.34}$$

Therefore, given eq. (2.32), it can be concluded that:

$$P_\theta(\omega) = \tilde{\mu}(\omega\cos\theta, \omega\sin\theta) \tag{2.35}$$

proving the *Fourier slice theorem*.

Therefore, it should be possible to reconstruct the object function by taking the projections over an angular range $\theta \in [0,\pi)$ and by first performing a 1D Fourier Transform (FT) on each projection, and then using a 2D inverse FT. In practice, only a finite number of projections of

an object can be taken and the Fourier space is filled radially (Figure 2.5 (a)).
Most algorithms that perform the Fourier transformation require data interpolation from these radial points to the points on a Cartesian grid (Figure 2.5). This interpolation, in the Fourier domain, generally introduces high-frequency reconstruction artefacts since the higher frequencies, which correspond to the fine details of an object, are sampled less frequently. FBP is a reconstruction algorithm which overcomes these drawbacks. In the following, this practical approach, yet related, will be described.

2.5 Filtered Back Projection

To derive the Filtered Back Projection algorithm, we consider the inverse Fourier Transform of eq. (2.32)

$$\mu(x,y) = \int\int_{-\infty}^{+\infty} \tilde{\mu}(u,v) \exp\{i2\pi(ux+vy)\}\, du\, dv \tag{2.36}$$

in polar coordinate system (ω, θ), by substitutions

$$\begin{cases} u = \omega \cos\theta \\ v = \omega \sin\theta \\ du\, dv = \omega\, d\omega\, d\theta \end{cases}$$

eq. (2.36) can be rewritten as:

$$\begin{aligned} \mu(x,y) &= \int_0^{2\pi} \int_0^{+\infty} \tilde{\mu}(\omega\cos\theta, \omega\sin\theta) \exp\{i2\pi(x\cos\theta + y\sin\theta)\omega\}\, \omega\, d\omega\, d\theta \\ &= \int_0^{\pi} \int_{-\infty}^{+\infty} \tilde{\mu}(\omega\cos\theta, \omega\sin\theta) \exp\{i2\pi(x\cos\theta + y\sin\theta)\omega\} |\omega|\, d\omega\, d\theta \\ &= \int_0^{\pi} \int_{-\infty}^{+\infty} P_\theta(\omega)|\omega| \exp\{i2\pi t\omega\}\, d\omega\, d\theta \end{aligned} \tag{2.37}$$

where the first and the second equalities follow from eq. (2.31) and eq. (2.35), respectively. Moreover, in the second equality, $t = x\cos\theta + y\sin\theta$ for simplicity.
Eq. (2.37) is commonly written in two parts:

- the integration over ω:

$$q_\theta(t) = \mathscr{F}^{-1}\{P_\theta(\omega)|\omega|\} = \int_{-\infty}^{+\infty} P_\theta(\omega)|\omega| \exp\{i2\pi t\omega\}\, d\omega \tag{2.38}$$

which is referred to as **filtering**. Each projection data $p_\theta(t)$ is filtered by multiplying its Fourier transform, $P_\theta(\omega)$, with $|\omega|$. The frequency response of the filter is given by $|\omega|$. And,

- the integration over θ:

$$\mu(x,y) = \int_0^{\pi} q_\theta(t)\, d\theta \tag{2.39}$$

which is referred to as **backprojection**. The filtered projection data is back-projected onto the reconstruction grid along the lines $t = x\cos\theta + y\sin\theta$.

Eqs. (2.38) and (2.39) form the *Filtered Backprojection* inverse scheme.
Under the correspondence between multiplication in Fourier space and convolution in reciprocal space the eq. (2.38) is also possible to write:

$$q_\theta(t) = \int_{-\infty}^{+\infty} P_\theta(t')h(t-t')\, dt' \tag{2.40}$$

where

$$h(t) = \mathscr{F}^{-1}\{|\omega|\} = \int_{-\infty}^{+\infty} |\omega| \exp\{i2\pi t\omega\}\, d\omega \tag{2.41}$$

is often called a ramp-filter due to its shape in the Fourier domain.

The FBP algorithm is applied for tomographic reconstruction of the measurements in Section 5.1.1.

2.6 Feldkamp-Davis-Kress algorithm

FBP is only applicable in the case of a parallel beam projection geometry. While this condition can be achieved by collimating the beam, it leads to reduced flux and increased scan times. Therefore, in practice, most laboratories use an uncollimated cone beam. The FBP formula can then be applied only in those cases where the cone angle is sufficiently small. Otherwise, data should be reconstructed using an extension of the FBP algorithm to cone-beam geometries. A popular reconstruction method for cone-beam data has been proposed by Feldkamp, Davis, and Kress in 1984[32]. We will call this algorithm the FDK method.

Consider the Figure 2.6, we have the projection angle β and the detector position is given by:

$$a(x,y,z) = R\frac{-x\sin\beta + y\cos\beta}{R + x\cos\beta + y\sin\beta}, \qquad b(x,y,z) = z\frac{R}{R + x\cos\beta + y\sin\beta}$$

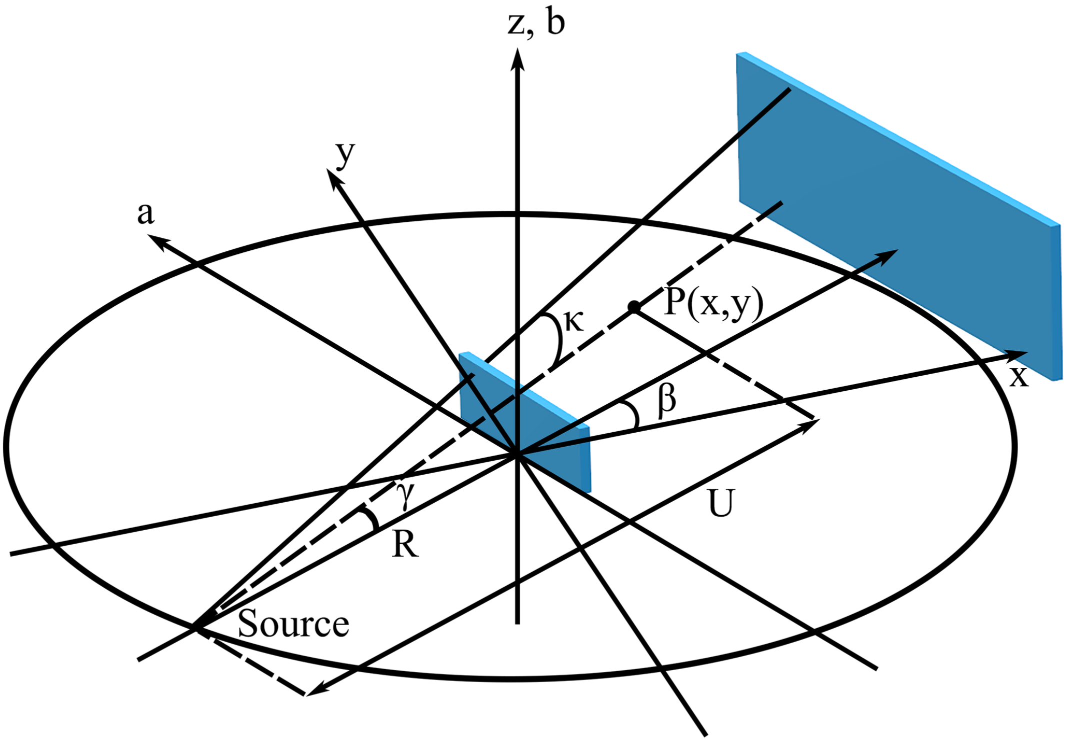

Figure 2.6 The cone-beam geometry with planar (a,b) detector.

Furthermore, we define the fan-angle γ, and the cone-angle κ as:

$$\gamma = \arctan\frac{a}{R}, \qquad \kappa = \arctan\frac{b}{\sqrt{R^2+a^2}}$$

and the distance $U(x,y,\beta)$ between the source and the line parallel with the detector that intersects the image point $P(x,y)$ as:

$$U(x,y,\beta) = R + x\cos\beta + y\sin\beta$$

For cone-beam tomography, the reconstruction is a filtered back-projection very similar to the two-dimensional algorithm presented in Section 2.5, which can be broken into the following three steps:

- Multiply the projection data, $P_\beta(a,b)$, by a pre-weighting factor to find $P'_\beta(a,b)$:

$$P'_\beta(a,b) = \frac{R}{\sqrt{R^2+a^2+b^2}} P_\beta(a,b) \tag{2.42}$$

- Convolve the weighted projection $P'_\beta(a,b)$ with the ramp-filter $h(a)/2$. The result $Q_\beta(a,b)$ is written as:

$$Q_\beta(a,b) = P'_\beta(a,b) * \frac{1}{2}h(a) \tag{2.43}$$

  Note that the ramp-filter is the same as for the parallel beam.

- Finally, each pre-weighted and filtered projection is back-projected over the three-dimensional reconstruction grid:

$$\mu(x,y,z) = \int_0^{2\pi} \frac{R^2}{U(x,y,\beta)^2} Q_\beta(a(x,y,\beta), b(x,y,z,\beta))\, d\beta \tag{2.44}$$

Note that, in eq. (2.42), the pre-weighting factor is factorised into the two cosine factors of the fan- and cone-angle as:

$$\frac{R}{\sqrt{R^2+a^2+b^2}} = \frac{R}{\sqrt{R^2+a^2}} \frac{\sqrt{R^2+a^2}}{\sqrt{R^2+a^2+b^2}} = \cos\gamma \cos\kappa$$

This technique has a simple implementation and fast computation times. It is an approximation technique that generally results in adequate reconstructions for small cone angles, so artefacts become more significant with an increasingly large cone angle [32, 44].

The FDK algorithm is applied for tomographic reconstruction of the measurements in Section 5.1.2.

2.7 Artifacts

Image errors that occur in reconstructed data which do not belong to the object, but that originate from systematic errors in the image acquisition process (by technique or equipment), are called *artifacts*. A wide variety of artifacts may arise in X-ray tomography. In this section, the main artifacts, i.e., beam hardening artifacts, motion artifacts, misalignment artefacts, and ring artifacts, will be described.

The **beam hardening artifacts** occur for polychromatic radiation. The X-ray interaction with the object depends on the X-ray energy. The object absorbs more of the lower energy x-rays than the higher energy X-rays. The transmitted X-rays will consequently have higher mean energy, i.e., they are harder. In this case, the attenuation of the X-ray intensity does not follow the simple absorption law (see eq. (2.27)). In tomography, this leads to cupping artifacts.

Motion artifacts are a type of artifact that originates from unwanted movements of the object or the imaging system during the entire acquisition. It caused smearing of the image with ghost images in the motion direction if the movement is considerable. Small movements of the object result in a blurring of the small portion of the object across the image. The motion artifacts can be partially corrected by an autocorrelation algorithm.

Another type of artifacts is banana-shaped **misalignment artifacts**. These can result if the geometric parameters of a certain projection (i.e., the position of the source and detector-array concerning the origin) are not what is assumed. This can occur if the gantry on which the source and detector are mounted is not stable during its rotation. To correctly perform the aligned projection data, the center of rotation has to be assessed with either automatic suggestions (see e.g. [87]) or visual supervision.

In the last case, circles appear in the reconstructed data (**ring artifacts**) around the axis of rotation, and in straight vertical lines in the sinogram. These are due to systematic errors in the illumination or detector (e.g., irregular sensitivity of the different pixels or dust on the scintillator), since projections are acquired around the full object. As a first-order correction, the projection data (I) can be normalized by also measuring a dark field image, I_{dark} (an image acquired when the X-ray source is turned off), and a bright-field image I_{flat} (an image acquired when the X-ray source is turned on but without the sample):

$$I_{corr} = \frac{I - I_{dark}}{I_{flat} - I_{dark}} \tag{2.45}$$

It assumes that the response is linear and not altered by other factors. These constraints are, however, not always fulfilled, and remaining ring artifacts. They can be removed, for example, by filtering with a selective median filter which is only applied when a pixel deviates from the surrounding pixel by a certain threshold. Otherwise, in literature exist many sinogram de-striping approaches [70, 11, 58].

2.8 Application of X-ray Tomography to Cultural Heritage

X-ray tomography allows a great number of potential applications. Originally born for medical application in the early Seventies, it is currently playing an increasingly important role in the Archeological and Cultural Heritage Science.

X-ray tomography detects shapes and structures not only from the surface but also from the inside, obtaining a complete 3D volume imaging of the analyzed object, also thanks to modern rendering techniques. This kind of information is very important for scientific investigations, restoration procedures and conservation purposes of very rare and fragile objects, on which no damage must be done. Modern conservation principles imposed by the archaeologists in the studies of ancient and precious materials require that the selected techniques must be non-destructive and non-invasive.

A peculiar characteristic of the archeological finds is that they are often heterogeneous and complex in shape and composition and are often covered by alterated layer. Different kinds of objects like sculptures, paintings, and others [57, 56, 71, 8] have to be inspected to acquire significant information, such as composition, dating, provenance, art technology, conservation, but also defects and damage. Although it is a more demanding use, X-ray tomography is an interesting option and, probably, the only one available for non-invasive recovering of text inside damaged manuscripts.

Another technique used in the field of Cultural Heritage is the X-ray radiography which is not enough to read the complete text as in most cases pages of the manuscript are folded several times or there is more than one page in a single document. In such a case, a simple radiograph causes the superposition of writings in the output image. X-ray tomography reconstructs the whole manuscript and allows potentially the virtual separation of single pages. The technique is particularly useful when the conservation conditions (fragile, burnt, etc.) of the manuscripts or the conservators' decision is not allowing their unfolding or for those that are still closed and sealed [6, 53, 79].

These studies have led to important results because the contrast between ink and writing substrate is high thanks to the widespread use, from many centuries and all around Europe, of iron-based inks, the *Iron Gall* [92]. This type of ink is significantly dense and so absorbs more X-ray than the supports (paper and parchments). But, the situation becomes difficult when we have papyrus substrate, made of ordered carbon fibers, and carbon-based ink. Standard absorption tomography is an unsuitable technique to discriminate details of similar densities and a better contrast is achieved applying different imaging methods so that the ink is directly visible in the resulting image. Imaging the phase modulation induced by the object in a coherent or partially coherent beam has been used successfully for imaging the Herculaneum papyri scrolls [54, 16].

In the next chapter, we will study the X-ray phase-contrast tomography in detail.

Chapter 3

X-ray Phase Contrast Tomography

When X-rays penetrate matter, both the amplitude and the phase of the electromagnetic wave are affected (as we see in Chapter 2). The amplitude gets attenuated and the phase gets shifted (Figure 2.1). Both effects can potentially be used for imaging.

To understand the advantages of phase methods in the field of X-rays, it is useful to compare the physical principles on which they are based compared to those of conventional methods. As already anticipated in Chapter 2, traditional techniques exploit the absorption of radiation in the sample, while the phase methods allow highlighting the phase shifts suffered by the electromagnetic waves passing through the sample.

When calculating the refraction effects of X-rays penetrating matter, one can calculate both absorption and phase shift of the X-ray wave from the complex index of refraction $n = 1 - \delta + i\beta$ (eq.(2.2))[4]. The radiation phase shifts are proportional to the term δ, while the absorption coefficient, responsible for the formation of the contrast in the conventional imaging, is proportional to the imaginary term β.

Numerically, n deviates only slightly from unity, δ and β being extremely small for X-rays. However, for many materials (in particular low attenuating materials) and in the energy range typically used for X-ray imaging, δ is considerably larger than β, by up to three orders of magnitude (as we show in Figure 3.1). Therefore, when the absorption is very weak or undetectable, improved contrast can be achieved if the imaging system is sensitive to δ changes.

Furthermore, for hard X-ray, it should be noted that δ and β do not depend on energy in the same way; in fact, $\delta \propto 1/E^2$ while $\beta \propto 1/E^4$. This suggests that the improvement due to phase contrast can be maintained at higher energies.

It is not possible to measure the phase directly since X-ray detectors will only measure the intensity of the beam. To do phase-contrast imaging, the imaging system must be able

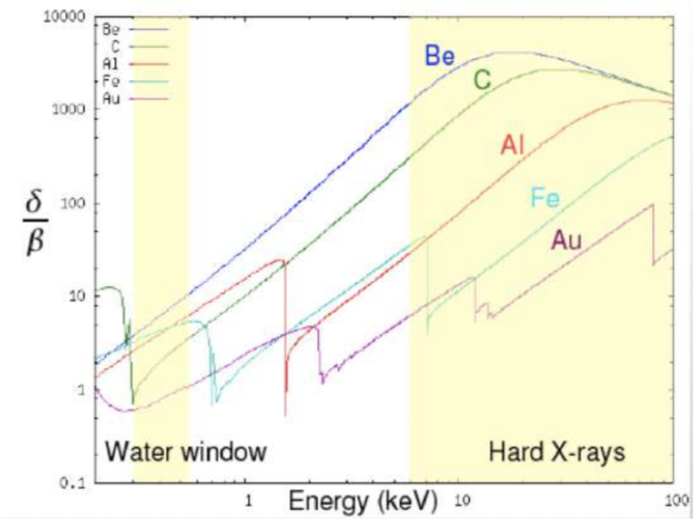

Figure 3.1 The trend of the δ/β ratio for beryllium (Be), carbon (C), aluminum (Al), iron (Fe) and gold (Au) as a function of energy in the energy range $0.1 - 100keV$. We can observe how for elements such as carbon the δ/β ratio increases by three orders of magnitude, where the factor δ is directly linked to the phase variation.

to convert the phase shift into intensity variations. This can be achieved by two different approaches.

The first one is based on the detection of interference patterns, in general, this can be achieved by positioning the detector at an increased distance away from the object, thus allowing the beam to propagate and obtaining an interference pattern.

The second approach involves the detection of X-ray refraction by using interferometry or grating systems. The local distortion of wavefront due to the phase shifts introduced by the object results in a change in the direction of X-ray propagation. The angle by which the X-ray is deviated (*refraction angle*) can be expressed as [13]:

$$\alpha(x,y,\lambda) \simeq -\frac{\lambda}{2\pi}\nabla_{x,y}\phi(x,y,\lambda) \tag{3.1}$$

where $\nabla_{x,y}$ indicates the 2-dimensional gradient, resulting in the two transverse components of the refraction angle, and ϕ is the phase modulation provided by eq. (2.12).

In this chapter, we provide an overview and the physical principles of the X-ray Phase Contrast Imaging Techniques (XPCT). The associated advantages and limitations of each method will be highlighted. Furthermore, information about the most common algorithms used to retrieve phase information ("Phase Retrieval" algorithms) will be provided.

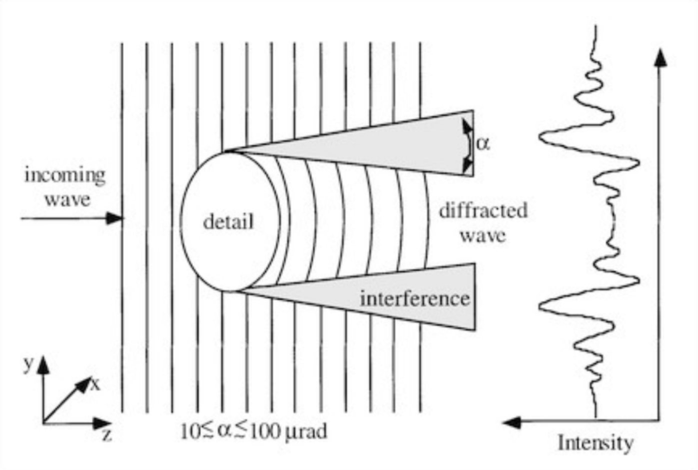

Figure 3.2 Interference of the phase-shifted wave with the unrefracted waves. α is the refraction angle. Figure adapted from [3].

3.1 Coherence

The concept of coherence in X-ray Phase Contrast imaging is very important.
Coherence is the property that describes the capability that a field has to form stable interference fringes [4, 13, 62].

Mathematically, a *mutual coherence function* ($\Gamma(\mathbf{x}_1, \mathbf{x}_2, \tau)$) is used as a measure of the degree of the correlation which exists between the field (E) at observation points $\mathbf{x}_1$ and $\mathbf{x}_2$:

$$\Gamma(\mathbf{x}_1, \mathbf{x}_2, \tau) \equiv \langle E(\mathbf{x}_1, t+\tau) E^*(\mathbf{x}_2, t) \rangle \tag{3.2}$$

where τ is the time delay and the angular brackets denote an expectation value, or a time average of the indicated product.

It is often convenient to introduce the normalized mutual coherence function, known as the *complex degree of coherence* ($\gamma(\mathbf{x}_1, \mathbf{x}_2, \tau)$) as:

$$\gamma(\mathbf{x}_1, \mathbf{x}_2, \tau) \equiv \frac{\Gamma(\mathbf{x}_1, \mathbf{x}_2, \tau)}{\sqrt{\Gamma(\mathbf{x}_1, \mathbf{x}_1, \tau=0)\Gamma(\mathbf{x}_2, \mathbf{x}_2, \tau=0)}} = \frac{\Gamma(\mathbf{x}_1, \mathbf{x}_2, \tau)}{\sqrt{I(\mathbf{x}_1)I(\mathbf{x}_2)}} \tag{3.3}$$

It is a properly normalized correlation coefficient, so that $\gamma(\mathbf{x}_1, \mathbf{x}_1, \tau=0) = \gamma(\mathbf{x}_2, \mathbf{x}_2, \tau = 0) = 0$. This indicates that the field at a point in space must always be perfectly coherent with itself.

For the existence of interference fringes, a necessary condition is that a correlation between the radiation at $\mathbf{x}_1$ and $\mathbf{x}_2$ must exist. Perfect correlation implies a ‘perfect’ interference pattern (‘perfect’ in the sense that the interference fringes achieve their maximal visibility) and perfect coherence. Zero correlation implies no interference pattern and incoherence. Real sources are neither fully coherent nor fully incoherent, but rather are partially coherent.

When dealing with coherence, it is customary to introduce the *regions of coherence* and the *coherence time*, i.e., spatial and temporal measures over which the fields are well correlated.

In cases where there is a well-defined direction of propagation, it is convenient to decompose the region of coherence into one component in the direction of propagation and one component transverse to it.

In the direction of propagation it is common to introduce a longitudinal, or temporal, coherence length (l_{long}) over which phase relationships are maintained:

$$l_{long} = \frac{\lambda^2}{2\Delta\lambda} \tag{3.4}$$

where λ is the wavelength and $\Delta\lambda$ is the spectral width. l_{long} is associated to the monochromaticity $\Delta\lambda/\lambda$ of the X- ray beam. Therefore improving the monochromaticity of the beam is equivalent to increasing the temporal coherence.

Transverse, or spatial, coherence is related to the finite source size and the characteristic emission (or observation) angle of the radiation. The lateral, or spatial, coherence length (l_{tran}) is defined as:

$$l_{tran} = \frac{\lambda z_{so}}{2S} \tag{3.5}$$

where z_{so} and S represent the source-to-object distance and the transverse dimension of the source. From eq. (3.5), it is clear that to improve spatial coherence, it is necessary to decrease the size of the source (S) or increase the distance between the source and the sample (z_{so}).

3.2 X-ray Phase Contrast Imaging Techniques

Several techniques exist for X-ray phase-contrast imaging. The techniques may be grouped into three categories (1) Analyzer Based Imaging (ABI), (2) Grating Interferometry (GI), and (3) Propagation Based Imaging (PBI). The three imaging methods are schematically shown in Figure 3.3.

For each of these techniques, the contrast in the final image will depend on the spatial resolution of the detector, the image formation mechanism and the X-ray energy. Then there is no valid technique for any type of problem: each has its area of application.

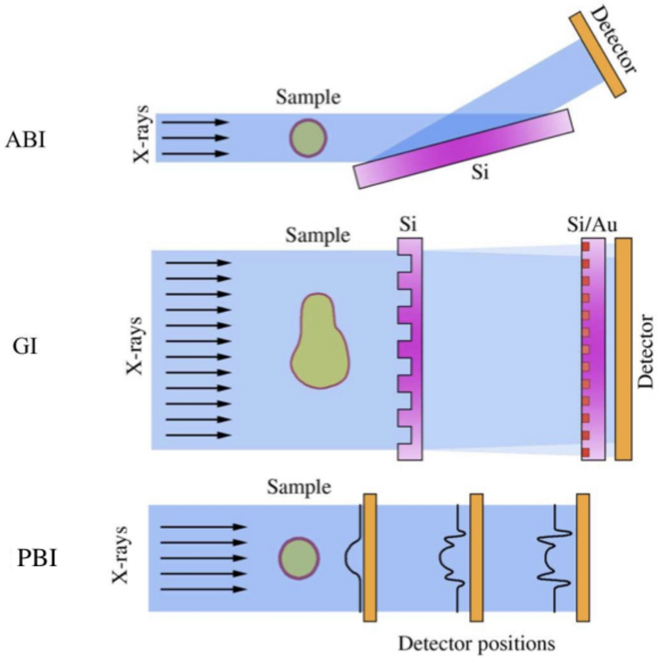

Figure 3.3 Schematic drawings of Analyzer Based Imaging (ABI), Grating Interferometry (GI), and Propagation Based Imaging (PBI). Figure adapted from [7].

In the following, we will give a short review of these methods by focusing in particular on the Propagation based imaging, which is the used method in this thesis work.

3.2.1 Analyzer Based Imaging

The ABI technique consists of the use of a parallel quasi-monochromatic X-ray beam to irradiate the sample and of a perfect crystal, called analyzer crystal (AC), placed between the sample and the detector (see Figure 3.3) [35, 43, 30, 22].

The AC acts as an angular filter on the radiation emerging from the sample: only X-rays that have passed through the sample and that meet the Bragg law of diffraction are selected. X-rays that have an angle that does not check Bragg's law will not contribute to the signal on the detector because they are not reflected. This angle corresponds to the peak of the AC reflectivity curve (rocking curve). The rocking curve is obtained in this way: in the absence of the sample, rotating the crystal in the proximity of the Bragg angle and measuring at each

step the value of the intensity of the X-ray flow on the detector and after the AC is fixed at a certain angle and the sample is inserted.
Due to the presence of the AC, the ABI technique has the advantage of high phase sensitivity, only in the direction perpendicular to the analyzer crystal. Furthermore, the presence of the AC intrinsically affects the spatial resolution of the technique.

3.2.2 Grating Interferometry

The GI or X-ray Talbot interferometry is an X-ray phase-contrast imaging technique based on the use of grating interferometers [29, 55, 65].
The technique is based on an optical phenomenon discovered by H.F. Talbot in 1830 [34]. When a grating is coherently illuminated, a diffraction pattern identical to the grating is formed at a regular distance behind the grating, known as Talbot distances ($d_T = 2p^2/\lambda$,where p is the period of the grating). The wavefront of the emerging field is in phase for every d_T. While at a fraction of the Talbot distance, the image appears blurred.

The standard method consists (see Figure 3.3) of a first lattice known as phase grating, i.e., which has the characteristic of phase-shifting the incident rays, and a second lattice known as absorption grating (also called analyzer), which has its own the characteristic of absorbing incident beams.
The first grating has the function of spreading the beam (beam splitter) and dividing the incoming beam essentially in the first two orders of diffraction. It is generally made of a low absorbent material such as silicon.
When an object is inserted before or after the phase grid, the field is modified and local interference fringes appear, due to the refraction induced on the incident beam.
By measuring the variation that the sample has produced on the interference fringes, it is possible to mathematically reconstruct an image of the sample in the form of a phase map. However, since the step of the phase grid, and therefore of the fringes, is of the order of a few microns, a high-resolution detector is required to measure the variations. This is not always available and the second grating is introduced in front of the detector, which is used as an analyzer and consists of absorbent material (generally gold).

The phase effects can be separated from the object's attenuation by a method called "Phase Stepping" [88]. In this method, the phase grating is translated laterally and an image is acquired at each grating position. The displacement in the intensity oscillation in each pixel over the scan, compared to the case where the object is absent, is related directly to the differential phase shift of the wavefront. Stepping simultaneously yields three different signals: absorption, phase shift and dark field.

This technique, like the previous one, is particularly sensitive, i.e., it can distinguish details of similar density.

3.3 Propagation Phase Contrast Imaging

A different approach to phase imaging is Propagation Based phase contrast [83].
This technique consists of the X-ray source, the sample and the detector in line with each other (see Figure 3.3). This methodology of investigation takes the name of Free Space Propagation. In sufficiently coherent source conditions, phase effects can be observed without the aid of any optics.
Unlike the previous illustrated techniques, the detector is not placed immediately behind the sample. The distance between the sample and the detector is necessary to allow the radiation refracted by the sample to interact with the transmitted beam but which does not cross the sample, thus forming the diffraction fringes [13] (see Figure 3.2). The measured intensity fringes is thus not a direct measure of the phase like the crystal interferometer, but rather the Laplacian of the phase front [26].
The very simple experimental setup and the great stability make this technique particularly advantageous.

The theoretical foundations of this technique and the phase reconstruction methods will be analyzed below.

3.3.1 Theoretical basis

As described in Chapter 2, the wavefront will change inside the sample due to the interaction with matter. But the wavefront also changes during propagation through free space.
In the case of standard X-ray imaging, the detector (or image plane) is positioned immediately behind the sample, and it is safe to assume that nothing happened to the X-ray wavefront during the free space propagation from sample to the detector. Instead, for phase-contrast imaging, free space propagation is important.
A propagated wave-front may be calculated using *Huygens- Fresnel principle*. According to it, each point on a wavefront serves as the source of a spherical secondary wavelet with the same frequency as the primary wave. The amplitude at any point is the superposition of these wavelets. This theory was put on a sounder mathematical basis by Kirchoff, who showed that the *Huygens- Fresnel principle* may be regarded as an integral form, which expresses the solution of the wave equation, at an arbitrary point in the field $\mathbf{x}_0$, in term of both the solution and its first derivatives at all points on an arbitrary closed surface surrounding $\mathbf{x}_0$.

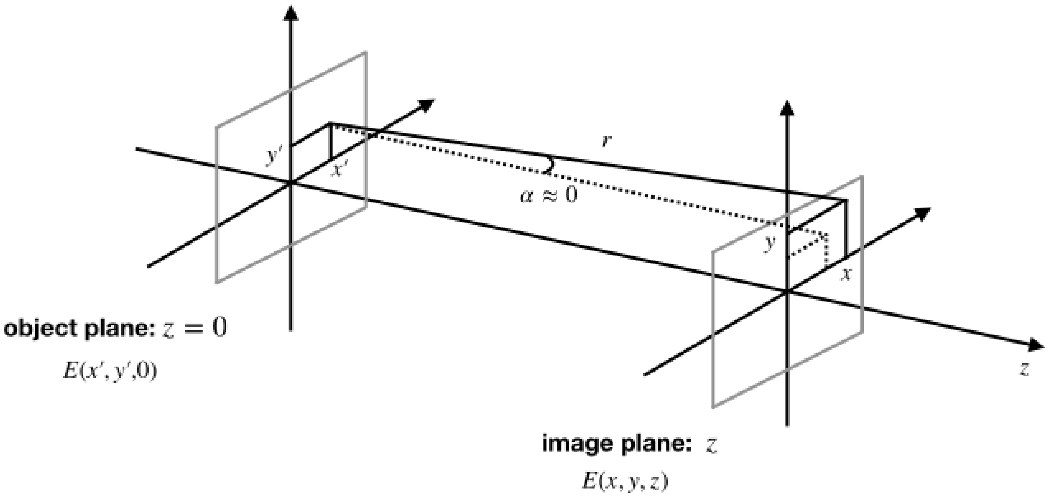

Figure 3.4 Schematic representation of the reference systems in the object plane and the image plane.

Applying *Green's theorem* to the waves that are solutions of the Helmholtz equation (V) and following the arguments by Born and Wolf [13], we obtain the expression known as the *integral theorem of Helmholtz and Kirchhoff*:

$$V(\mathbf{x}_0) = \frac{1}{4\pi} \iint_S \left[V \frac{\partial}{\partial n} \left(\frac{e^{ik|\mathbf{x}-\mathbf{x}_0|}}{|\mathbf{x}-\mathbf{x}_0|} \right) - \frac{\partial V}{\partial n} \left(\frac{e^{ik|\mathbf{x}-\mathbf{x}_0|}}{|\mathbf{x}-\mathbf{x}_0|} \right) \right] dS \tag{3.6}$$

where $\partial/\partial n$ denotes differentiation along the inward normal to the surface of integration S. To describe, in detail, what happens to the elastically diffused wave, after interacting with the sample, we start from eq. (3.6) and rewrite it assuming the condition of *paraxial approximation*:

$$V(x,y,z) = \iint_{z'=0} V(x',y',0) \frac{e^{ikr}}{i\lambda r} dx' dy' \tag{3.7}$$

this is so-called *Fresnel-Kirchhoff integral.*

In eq. (3.7), $(x',y',0)$ and (x,y,z) are the coordinates of the object plane and of the detector plane, respectively, λ is the wavelength and $r = \sqrt{(x-x')^2 + (y-y')^2 + z^2}$ is the ray vector (see Figure 3.4).

Despite the accuracy of the Fresnel-Kirchhoff theory, its calculation is exceedingly difficult due to the highly oscillatory function in the integrand. Hence further simplifications have been sought and developed.

Fresnel regime

We can simplify the algebraic expression by introducing the following substitution:

$$\rho^2 = (x-x')^2 + (y-y')^2 \tag{3.8}$$

to express r as:

$$r = \sqrt{\rho^2 + z^2} = z\sqrt{1 + \frac{\rho^2}{z^2}} \simeq z + \frac{\rho^2}{2z} - \frac{\rho^4}{8z^3} + \ldots \tag{3.9}$$

where the last equality follows from Taylor series development. Moreover, we consider Fresnel approximation, that consists of $\rho \ll z$; so we can approximate r at the first-order:

$$r \simeq z + \frac{(x-x')^2 + (y-y')^2}{2z} \tag{3.10}$$

and replacing this expression in the eq. (3.7), we obtain:

$$V(x,y,z) = \frac{i}{\lambda}\frac{e^{ikz}}{z} \iint V(x',y',0) \exp\left\{ ik \frac{\left[(x-x')^2 + (y-y')^2\right]}{2z} \right\} dx'\, dy' \tag{3.11}$$

this is the *Fresnel diffraction integral.*
It may be seen that the convolution integral is the same

$$V(x,y,z) = \iint V(x',y',0) P_z(x-x', y-y')\, dx'\, dy' \tag{3.12}$$

where the function $P_z(x,y)$ is:

$$P_z(x,y) = \frac{i}{\lambda z} \exp\left\{ \frac{i\pi}{\lambda z}(x^2 + y^2) \right\} \tag{3.13}$$

Hence, considering that the transmission function, except for a phase factor, is $V(x',y',0) = T(x',y')$,

$$V(x,y,z) = T(x,y) \otimes P_z(x,y) \tag{3.14}$$

where $\otimes$ denotes two dimensional convolution. This equation shows that the diffraction pattern is given by the convolution between the *transmission function* of the sample ($T(x,y)$)

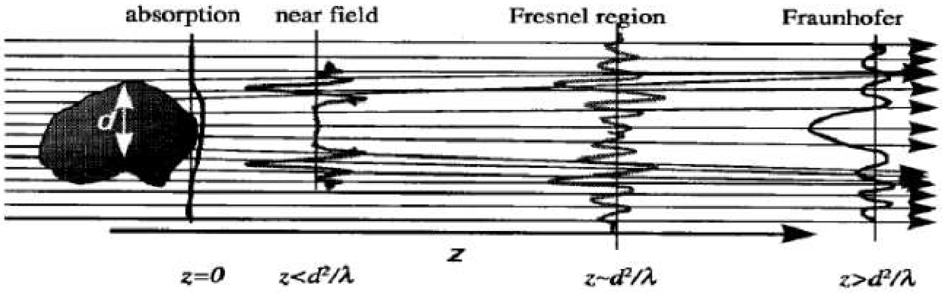

Figure 3.5 Schematic representation of the refraction regions as a function of the distance from the object.

and a parabolic wave originating from the sample, called the *Fresnel propagator*, propagating in the z-direction ($P_z(x,y)$).

Fraunhofer regime

For propagation distances much larger than a Fresnel reference distance (d_F), defined as:

$$d_F = d^2/\lambda \tag{3.15}$$

where d defines the linear dimension of the object, we have the so-called *Fraunhofer regime* (see Figure 3.5).

Converting k into $k = \dfrac{2\pi}{\lambda}$ and expanding the squares of the exponent in the integral in eq. (3.11):

$$\begin{aligned} V(x,y,z) =& \frac{i}{\lambda}\frac{e^{ikz}}{z}\exp\left\{i\frac{\pi}{\lambda z}(x^2+y^2)\right\}\iint T(x',y')\exp\left\{-i\frac{2\pi}{\lambda z}(xx'+yy')\right\} \\ & \exp\left\{i\frac{\pi}{\lambda z}(x'^2+y'^2)\right\}dx'\,dy' \end{aligned} \tag{3.16}$$

if

$$z \gg \frac{\pi(x'^2+y'^2)}{\lambda} \tag{3.17}$$

the third exponential in the integral can be set to unity and we obtain the *Fraunhofer approximation* or *far field approximation*:

$$V(x,y,z) = \frac{i}{\lambda}\frac{e^{ikz}}{z}\exp\left\{i\frac{\pi}{\lambda z}(x^2+y^2)\right\}\iint T(x',y')\exp\left\{-i\frac{2\pi}{\lambda z}(xx'+yy')\right\}dx'dy' \quad (3.18)$$

this is the *Fraunhofer diffraction integral.*
Unlike the Fresnel field (i.e., eq.(3.14) with eq.(3.13)), the Fraunhofer field (eq.(3.18)) increases its transversal dimensions linearly with the propagation distance z. This starts to occur when z reaches a high value compared to the Fresnel distance d_F.

3.3.2 Contrast Transfer Function

We may make use of the convolution theorem, stating that the Fourier transform of the convolution of two functions is equal to the product of their Fourier trasforms. In the Fourier space eq. (3.14) can be rewritten as:

$$\mathscr{F}\{V(x,y,z)\} = \mathscr{F}\{T(x,y)\otimes P_z(x,y)\} = \mathscr{F}\{T(x,y)\}\mathscr{F}\{P_z(x,y)\} \quad (3.19)$$

By expressing the Fourier transform of P_z and indicating the functions in the Fourier space with the " $\sim$ " for simplicity, we have:

$$\tilde{V}_z(f_x,f_y) = \tilde{T}(f_x,f_y)\exp\left\{i\pi\lambda z(f_x^2+f_y^2)\right\} \quad (3.20)$$

where the function $\exp\left\{i\pi\lambda z(f_x^2+f_y^2)\right\} = \exp\{i\chi\}$ is called the *Optical Transfer Function* (OPF) for the Fresnel diffraction. It can be seen as a filter that acts on transmitted frequencies. Using eq. (2.25) in calculating $\tilde{T}(f_x,f_y)$, one finds:

$$\tilde{V}_z = \left[\delta - \tilde{\mu}_t + i\tilde{\phi}\right]\exp\{i\chi\} = \delta - \tilde{\phi}\sin\chi - \tilde{\mu}_t\cos\chi + i\left(\tilde{\phi}\cos\chi - \tilde{\mu}_t\sin\chi\right) \quad (3.21)$$

where δ is the unit impulse function and for compactness we have omitted the dependence on (f_x,f_y).
The intensity, by retaining only first order terms in $\tilde{\phi}$ and $\tilde{\mu}_t$, is:

$$\tilde{I}_z = |\tilde{V}_z|^2 \approx \delta - 2\tilde{\mu}_t\cos(\pi\lambda z(f_x^2+f_y^2)) - 2\tilde{\phi}\sin(\pi\lambda z(f_x^2+f_y^2)) \quad (3.22)$$

The first term (Dirac delta function) corresponds to a homogeneous background in the image due to the non-interacting beam. The terms with sin and cos are called phase and amplitude contrast transfer function (CTF) and are plotted against the reduced variable $\sqrt{\lambda z}u$ in Figure

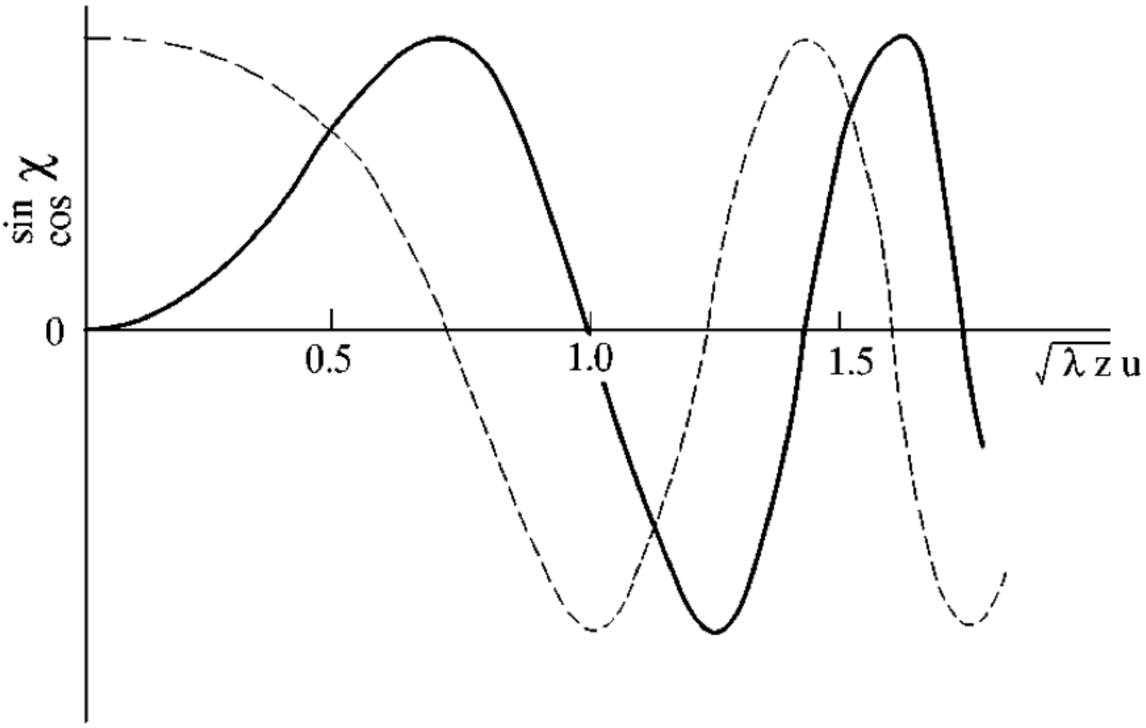

Figure 3.6 Fresnel approximation transfer functions vs. reduced spatial frequency $\sqrt{\lambda z}u$. The dashed line represents the absorption contribution (cos-term), and the solid line the phase contribution (sin-term) [67].

3.6. The sin-term represents an intensity modulation due to phase variations, while the cos is linked to absorption phenomena. By introducing a distance between the sample and the detector (z), it is possible to observe a phase modulation due to the interaction with the object in terms of intensity modulation.

The graphic in Figure 3.6 is useful for determining the distance z. If we set the parameter $\sqrt{\lambda z}u$ to be able to maximize the phase contrast and minimize the contribution in absorption, given the source energy, we can calculate z.

3.3.3 Regions of image formation

The image formed on the detector, obtained as a modulation of the intensity caused by the phase variation, is called the defocused image. It is common to introduce an effective propagation distance called *defocusing distance*, defined as:

$$z = \frac{z_{so} z_{od}}{(z_{so} + z_{od})} \tag{3.23}$$

where z_{so} and z_{od} are the source-object planes distance and the object-detector planes distance, respectively. The eq. (3.23) expresses how out-of-focus the image is on the detector.

Different regimes of imaging can be exploited as a function of the defocusing distance and the object size. They can be roughly discriminated comparing the defocusing distance (3.23) with the Fresnel distance (3.15). To do this is usually to introduce the Fresnel number:

$$N_F = \frac{d_F}{z} \tag{3.24}$$

According to the Fresnel number, fixing wavelength and object size, it is possible to distinguish three different diffraction regimes according to the distance z (see Figure 3.5): absorption, near field, and holographic regime.

Absorption

In this case $z = 0$, there is no wave propagation. Consequently, only the attenuation of the incident wave is measured. The expression for I is reduced to eq. (2.27), i.e., the intensity in absorption imaging.

Near field regime

In this case $z \ll d_F$ or equivalently $N_F \gg 1$. The intensity in the real space can be calculated as:

$$I(x) = I_{abs}\left[1 + \frac{\lambda z}{2\pi}\Delta\phi(x)\right] \tag{3.25}$$

It describes an absorption image (first term) with an additional contribution from the Laplacian of the object phase distribution, i.e., proportional to the second derivate of phase shift.

The contrast of the image depends on the phase shift induced by the object on the transmitted wave. In this regime, interference fringes appear at the rapid variations of the real part of the refraction index, for example at the edges of the structures. This phenomenon is called *edge-enhancement*.

Two important features may highlight in the eq. (3.25):

- the contrast in the image increases directly with z;
- the wavelength appears only as a separable factor. The geometric features of the contrast do not depend on wavelength. Polychromatic radiation may equally well be used and the factor λ is then replaced by a spectrally weighted sum. This result allows

us to understand that in phase-contrast imaging, one of the key properties of the source is lateral spatial coherence, while longitudinal coherent (temporal) is less important.

Holographic regime

If the defocusing distance increases further, the intensity distribution tends to lose resemblance with the original object and usually, the corresponding intensity distribution is called hologram. A hologram is an image obtained by phase contrast, and which can be acquired both in the *Fresnel region* ($z \approx d_F$ or equivalently $N_F \approx 1$) where the field is given by eq. (3.14), and in the *Fraunhofer regime* (when $z \gg d_F$ or $N_F \ll 1$) where the field is given by eq. (3.18).

3.3.4 Spatial resolution and coherence requirements

Spatial resolution is the ability of an instrument to produce distinct images of two objects that are very close together. The main factors influencing spatial resolution are detector resolution, source coherence, and diffraction limit.

We will now analyze the characteristics indicated above in detail.

Detector resolution

A very important part of a phase-contrast experiment is the X-ray detector. A major criterion that influences the choice of a detector is the point-spread function (PSF). This function tells how a single point will be spread and thus it is a measure for the achievable resolution. We can assume a gaussian trend for the ideal PSF.

In a space-invariant system, i.e., the PSF is the same everywhere in the imaging space, the image by a detector ($I_{detector}$) is the result of the convolution of the incident signal (I_{in}) with the PSF acquisition system:

$$I_{detector} = (PSF) \otimes I_{in} \tag{3.26}$$

A quantity that is typically stated to quantify the detector resolution ($r_{detector}$) is the full-width at half maximum (FWHM) of the PSF.

Source coherence

A non-coherent source that illuminates an object will lead to an image blurring because all points of the source will add up inconsistently. To avoid that the coherence of the source limits the spatial resolution, the resolution due to the coherence of the source (r_{source}) must be less than the detector resolution:

$$r_{source} < r_{detector} \tag{3.27}$$

Considering a source of size s at a distance z_{os} from an object, the eq. (3.27) turns into:

$$s < \frac{z_{os}}{z} r_{detector} \tag{3.28}$$

where z is the defocusing distance (see eq. (3.23)).
As it is possible to observe from eq.(3.28), as the distance of defocusing (z) increases, the condition on the linear dimension of the source becomes more stringent. To obtain a good spatial resolution, it is, however, possible to increase z_{os}.

Diffraction limit

The diffraction limit is an effect introduced by focus defects, i.e., the angle under which the object subtends the source aperture. Introducing the expression for the first Fresnel zone:

$$r_1 = \sqrt{\lambda z}, \tag{3.29}$$

we can define a resolution limit due to diffraction: if two objects are separated by a distance $r > r_1$, two beams diffracted by the two objects will not interfere in the image plane and can be solved separately. Conversely, objects very close such that $r < r_1$ will produce diffraction fringes blurred on the image plane. It is possible to avoid this deteriorating effect by positioning the sample in $z = 0$, as happens for acquisitions in absorption.

The phase-contrast method is based instead on the blur produced by the diffraction, through which, by evaluating the modulation of the intensity caused by the interference, it is possible to reconstruct the phase of the object.

3.3.5 Phase retrieval

The purpose of this section is to find the unknown phase starting from the measured intensity. The numerical process of solving the phase problem is known as *phase retrieval*. The phase map allows a quantitative analysis of the examined sample, precisely because the phase shift introduced is directly proportional to the electronic density of the structures inside the sample.

Several phase retrieval algorithms are available in the state of the art [16]; the choice to use one or the other depends on the characteristics of the sample (absorbing / transparent object), the diffraction regime (near field / far-field) and the experimental system (with optics / without optics).

In this section we will provide an overview of the different available non-iterative methods that use only one image at each projection angle.

Bronnikov algorithm

This was the first method derived. Bronnikov derived this method for tomography of pure phase objects, i.e., the absorption is assumed to be zero.

In PBI, the intensity recorded by the detector in the near-field is proportional to the second derivative of the phase function. This can be modeled through the transport of intensity equation (TIE) [39, 67, 84, 85]:

$$\nabla_{x,y} \cdot (I(x,y,z)\nabla_{x,y}\phi(x,y,z)) = -\frac{2\pi}{\lambda}\frac{\partial I(x,y,z)}{\partial z} \tag{3.30}$$

The left-hand side of eq.(3.30) is:

$$\nabla_{x,y} \cdot (I(x,y,z)\nabla_{x,y}\phi(x,y,z)) = I(x,y,z)\nabla^2_{x,y}\phi(x,y,z) + \underbrace{\nabla_{x,y}I(x,y,z) \cdot \nabla_{x,y}\phi(x,y,z)}_{=0} \tag{3.31}$$

where the second summand is zero for a pure phase object.
Furthermore, for a pure phase object, the intensity directly behind the object corresponds to the illumination that we again assume to be a plane wave with intensity I_0, i.e., $I(x,y,z=0) = I_0 = const$. If we further consider a small propagation distance d, the eq. (3.30) can be approximated by:

$$\begin{aligned} \nabla^2_{x,y}\phi(x,y) &\simeq -\frac{2\pi}{\lambda}\frac{I_d(x,y)-I_0}{I_0 d} \\ &= -\frac{2\pi}{\lambda d}\left(\frac{I_d(x,y)}{I_0}-1\right) \end{aligned} \tag{3.32}$$

The right-hand side of the eq. (3.32) can directly be measured. Thus, phase retrieval can be achieved by inverting the lateral Laplacian $\nabla^2_{x,y}$:

$$\phi(x,y) = -\frac{2\pi}{\lambda d}\nabla^{-2}_{x,y}\left(\frac{I_d(x,y)}{I_0}-1\right) \tag{3.33}$$

To reconstruct the phase map, the differential equation (3.33) is solved using the Fourier analysis and the inverse lateral Laplacian can be defined:

$$\nabla_{x,y}^{-2} = -\frac{1}{4\pi}\mathscr{F}^{-1}\left(\frac{1}{f_x^2+f_y^2}\mathscr{F}\right) \tag{3.34}$$

where $\mathscr{F}$ denotes the 2D Fourier transform and $\mathscr{F}^{-1}$ the in inverse 2D Fourier transform. Note that in this equation a singularity at $\mathbf{f} = (0,0)$ is present, then a regularization parameter α is introduced:

$$\nabla_{x,y}^{-2} = -\frac{1}{4\pi}\mathscr{F}^{-1}\left(\frac{1}{f_x^2+f_y^2+\alpha}\mathscr{F}\right) \tag{3.35}$$

Eq. (3.33) and eq. (3.35) can be implemented as a fast algorithm for phase retrieval that is known as *modified Bronnikov algorithm* [37]. It is called *modified* because term α is added to the original formulation [14] to account for what little absorption there might be.

Phase-attenuation duality method

Another method to reconstruct phase-contrast images was proposed by Wu *et al.* [89, 90]. For their algorithm, it is assumed that phase and absorption (eq. (2.12) and eq. (2.13)) are proportional to each other:

$$\phi(x,y) = -\lambda r_e \int \rho_e(x,y,z)\,dz \tag{3.36}$$

$$\mu_t(x,y) = \frac{\sigma_{KN}}{2}\int \rho_e(x,y,z)\,dz \tag{3.37}$$

In the literature, this effect is often called *phase-attenuation duality*.
In eq. (3.37), $\rho_e(x,y,z)$ is the material's electron density, and

$$\sigma_{KN} = 2\pi r_e^2\left\{\frac{1+\eta}{\eta^2}\left[\frac{2(1+\eta)}{1+2\eta}-\frac{1}{\eta}\ln(1+2\eta)\right]+\frac{1}{2\eta}\ln(1+2\eta)-\frac{(1+3\eta)}{(1+2\eta)^2}\right\} \tag{3.38}$$

is the Klein-Nishina formula for the total cross-section for x-ray photon Compton scattering from a single free electron. This holds where Compton scattering is the main contributor to μ (eq. (2.6) and eq. (2.7)), such as for light materials and photon energies of $60-500keV$. In eq. (3.38), $\eta = E/m_ec^2$, we denote the X-ray energy E, $m_ec^2 = 511keV$ is the resting electron energy, and r_e is the classical electron radius.
Under such conditions, remembering the eq. (2.26) can be substituted in the TIE (3.30) the expressions for $\phi(x,y)$ and $\mu_t(x,y)$ (eq. (3.36) and eq. (3.37)).

The phase-shift map can be retrieved from just a single-phase sensitive image as:

$$\phi(x,y) = \frac{\lambda r_e}{\sigma_{KN}} \ln\left(\mathscr{F}^{-1}\left\{\frac{\mathscr{F}\left[I_d(x,y)/I_0\right]}{2\pi\frac{r_e\lambda^2 d}{\sigma_{KN}}(f_x^2+f_y^2)+1}\right\}\right) \tag{3.39}$$

Paganin algorithm

Perhaps the most widely used phase retrieval method in single-image PBI is by Paganin *et al.* [63]. Also for their algorithm, it is assumed phase-attenuation duality. If one defines the projected thickness of an object $T(x,y)$, it is:

$$\phi(x,y) = -\frac{2\pi}{\lambda}\delta T(x,y) \tag{3.40}$$

$$\mu(x,y) = \frac{2\pi}{\lambda}\beta T(x,y) \tag{3.41}$$

where β and δ are the attenuation coefficient and refractive index decrement, respectively. Following the reasoning of the previous method, eq. (3.30) can be rearranged and solved for $T(x,y)$:

$$T(x,y) = -\frac{1}{\mu} \ln\left(\mathscr{F}^{-1}\left\{\frac{\mathscr{F}\left[I_d(x,y)/I_0\right]}{4\pi^2 d\frac{\delta}{\mu}(f_x^2+f_y^2)+1}\right\}\right) \tag{3.42}$$

This is achieved by making the following approximations:

- the object imaged is assumed *homogeneous object*. This means that the δ/μ-ratio is constant across the whole object;
- the incident wave is monochromatic;
- the incident wave is a plane (or only midly curved) wave;
- $z \ll d_F$ (near- field regime).

It often provides good qualitative results also in cases when the object is not strictly homogeneous but can be approximated as quasi-homogeneous.

Phase retrieval using eq. (3.42) can also be considered for the case of polychromatic or partially laterally coherent radiation [63].

Chapter 4

Virtual unfolding of Herculaneum papyri with X-ray

Recent advances in computer technology in the field of digital document restoration have led to the fast-growing interest in the virtual study of historical documents and the cultural heritage objects inaccessible without destruction or considerable damage. In most cases, ancient manuscripts are in a bad state of preservation, often rolled up or/and folded and highly distorted, as in the case of carbonized papyrus rolls such as those from Herculaneum.

A pioneer on scanning and virtual unfolding Herculaneum papyri has been Brent Seales [78]. Using micro-computed tomography (μ-CT), Seales *et al.* showed a tortured shape with minimal separation between layers along all three axes, which makes automated segmentation nearly impossible. Therefore, the processing required time-consuming manual segmentation, which succeeded in displaying small parchment portions with no visible text or ink.

Bukreeva *et al.* [15] proposed a computational platform for 'virtual unrolling' Herculaneum papyri leading to the revealing of traces compatible with letters, words, and portions of the Greek text. However, to minimize the impact of complex papyrus sheet geometry on text recognition, the investigated areas of the scrolls were limited to the least damaged parts of manuscripts and the papyrus sheet configuration close to the developed surface, i.e., the surface that can be virtually flattened without distortions.

In the last few years, many research groups have been working on the topic of recovery information from scanned documents using X-ray tomography other than Herculaneum papyri.

The standard virtual unwrapping pipeline involves the following steps: parchment layer segmentation, surface flattening, ink projection. The parchment layer virtual segmentation is the most challenging step due to physical damage, compression, etc. Samko *et al.* [76] elaborated a segmentation routine based on Graph Cut [91], in which a novel shape prior optimization and local geometric constraints are included. This routine identifies the damaged areas (avoiding over segment) and divides the tightly connected levels (avoiding under segment) at the same time.

Later, Seales *et al.* [79] developed algorithms for the digital unfolding of the extremely fragile charred scrolls from En-Gedi. A semi-automatic segmentation has been applied that enabled them to process much larger amounts of data than before [78]. The digital unfolding of the En-Gedi scroll and successive analysis of the hidden text is one of the most significant historical and cultural events of the last years. In this work, the physics-based material modeling (MM) algorithm was used for flattening. The mesh is represented as a mass-spring system, where each vertex of the mesh has a mass, and the connections between vertices are treated as springs with associated stiffness coefficients.

Subsequently, Liu *et al.* [52] built up a framework to virtually unroll Bressingham scroll. For this work, the method presented by Samko *et al.* [76] is adopted as a reference. Their image segmentation method involves: connecting layers of the parchment which are broken; detecting and matching junction sections; separating fused regions into several layers. To virtually unroll parchments, the extracted skeletons are aligned using dynamic programming based global optimisation. However, this technique has several drawbacks: (i) the thickness of the parchment layer must be identical everywhere and known a priori; (ii) separates a region composed of multiple layers by a curve that is as parallel as possible to the preserved boundary without considering the shape of the region; (iii) does not use the information from the previous portion processed to initialize the current segmentation.

An extension of this method is proposed by Rosin *et al.* [74]. The segmentation step, in this work, is entirely novel and mostly automatic and overcome the drawbacks of the work described above: (i) thickness of the parchment layers should be approximately locally uniform, so (ii) the locations of reconstructed missing boundary, in the regions composed of multiple fused layers curves, are optimized; (iii) the skeleton segments from the previously processed image are used to determined how to connect broken and missing layers.

In this chapter, we present advanced algorithms - illustrated by the pipeline shown in Figure 4.1- for the virtual unfolding of the Herculaneum papyri starting from non-invasive X-ray acquisitions.

4.1 Mathematical steps from a theoretical point of view

Our pipeline, shown in Figure 4.1, involves the following steps: surface segmentation, meshing, and reconstructing surface and mesh parameterization (i.e., flattening).

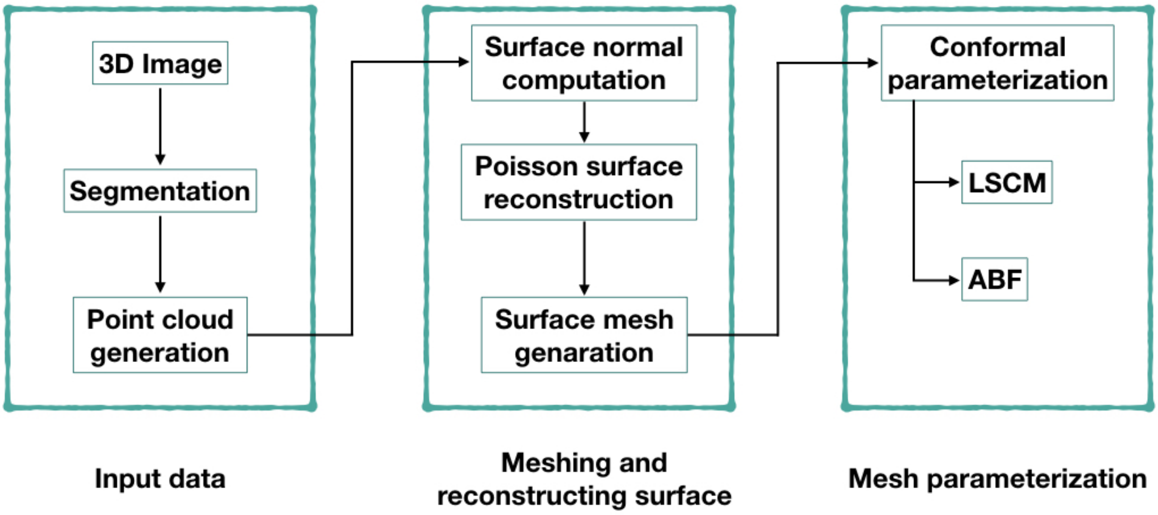

Figure 4.1 Pipeline of virtual unfolding.

The main goal of the developed pipeline has been the virtual segmentation and flattening of a single papyrus sheet, a challenging task for carbonized papyrus rolls.

4.1.1 Segmentation

The goal of the segmentation step is to define a 3D surface through the no structured scan volume. Important to note is that the segmentation step is effectively post-processing step, i.e., it is solely based on the finished reconstructed image. Image noise, low contrast, and scanning artifacts have a clear effect on the accuracy of the segmentation.
The precision and quality of the segmentation then significantly influences all subsequent steps.

Due to the complexity of the papyrus geometry, we can divide our procedure for the papyrus layer segmentation into two steps: one automatic segmentation and one manual postprocessing.

Automatic segmentation

Segmentation refers to the act of classifying image pixels into a few distinct and homogeneous classes based on a certain characteristic. The union of all the segmented classes must form the starting image.

In literature, there is a multitude of segmentation algorithms. Some methods are region-based, e.g. watershed segmentation [9] and region growing [94]. In other methods, object structures are modeled with active contours or snakes [23, 93]. The simplest yet effective technique to separate the object from the background is thresholding. All these techniques differ in the definition of the homogeneity criterion between the regions and for the algorithm used to create these regions. A good overview of them is given in [81].

Given the high quality of the images analyzed, the segmentation has been performed using a simple thresholding method. In this type of segmentation, the accuracy of the segmented images is determined by the chosen adequate threshold of gray level.
In an ideal case, the histogram has a deep and sharp valley between two peaks representing object and background, respectively. The threshold can be chosen at the bottom of the valley. In the real case, it is not possible to easily attribute the pixels to either the object or the background, because the valley is flat and broad, or noise or the two peaks are unequal in height. A multitude of solutions to this problem has been proposed in the literature [81]. They are, for example, histogram shape-based methods, which consider the shape properties (peaks, valleys, and curvatures) of the histogram [73, 80, 60, 69, 38]. Another class of methods clusters the gray-level samples into two parts (object and background) with numerous approaches. With modeled histogram as a mixture of two Gaussians [24]. With the iterative Otsu's clustering method [61], where the within-class variance is minimized, or the between-class scatter is maximized. Another class is entropy-based methods, which maximize the entropy between the object and background pixels [68] or to minimize the cross-entropy between the reconstruction and the segmentation [51].

Papyrus and air are automatically labeled using the Otsu's segmentation, implemented in ImageJ [75] (an open-source and free software).
The optimal threshold k^* for Otsu's algorithm is obtained, as mentioned above, maximizing the between-class variance ($\sigma_B^2(k^*)$):

$$\sigma_B^2(k^*) = \max_{1\leq k\leq L} \sigma_B^2(k) = \max_{1\leq k\leq L} \frac{[\mu_T \omega(k) - \mu(k)]^2}{\omega(k)\,[1-\omega(k)]} \tag{4.1}$$

where:

$$\omega(k) = \sum_{i=1}^{k} p_i \qquad \text{is the cumulative probability function;}$$

$$\mu(k) = \sum_{i=1}^{k} ip_i \qquad \text{is the first-order cumulative moment (mean);}$$

$$\mu_T = \mu(L) = \sum_{i=1}^{L} ip_i \qquad \text{is the total mean level of the original image.}$$

The probability distribution of the image is indicated by p_i, with $i = [0, 1, 2, ..., L]$, i.e., the gray-value range extends from 0 to L.

The output of the thresholding operation is a binary volume. Since dense material absorbs X-rays, the voxels representing the object (papyrus) are brighter than those corresponding to empty, so in the binary image the background (air) can be represented by 0, which is black, and the object by 255 in 8-bit images.

Manual postprocessing

The different sheets that form the papyrus appear convoluted and difficult to distinguish one from the other. Single sheet thickness is not homogeneous and has deformations at small and large scale, hence it is difficult to find portions even only locally uniform.
A general segmentation algorithm, like the one used above, may not identify the damaged papyrus areas and fail to split tightly connected sheets. Therefore, the process needs user interaction, which requires time and great accuracy. The idea is to identify the boundaries of the sheet from binary-valued segmentation volume and then follow the 3D surface.
Using ImageJ, we make full the volume - to lose the boundaries of the sheets – and smooth the surface - to have not holed 3D surface. Subsequently, we consider the external volume boundaries and the segmentation is complete.
The parchment boundaries are shifted to find the next sheets.

4.1.2 Meshing and reconstructing the surface

Having the 3D parchment sheet, we investigate its shape by reconstructing its surface using meshing. Meshing is a subdivision of a large continuous region into smaller discrete geometric and topological cells or elements. The goal is to create a mesh that accurately captures the input geometry without so many cells to make complex calculations.
Two types of 2D cell shapes are commonly used: triangle and quadrilateral. The choice of which mesh type to use will depend on the application, taking into account setup time and

the computational expense.
The sheets have a complex geometry. The creation of structured mesh (quadrilateral mesh) can be extremely time-consuming if not impossible. Therefore, setup time for complex geometry is the major motivation for using unstructured mesh employing triangular cells. Other risks using structured mesh with complicated geometry include the oversimplification of the geometry, mesh quality issues, and a less efficient mesh distribution (for example, fine resolution in areas of less importance) that results in a high number of cells.
A triangular mesh can be created with a lower number of cells than the equivalent quadrilateral mesh because it will force cells to be placed in a region where they are not needed. Therefore, for complex geometry with triangular mesh, convergence will be faster and possibly saving some computational expense.

A 3D triangulated surface mesh S embedded in R^3 is the union of a set of surface triangles: $S = \{T_1, ..., T_n\}$, where T_i represents the i-th triangle with its vertexes defined in 3D space as x_i, y_i, z_i.
An edge is defined as the line segment between two distinct points and two distinct vertices are called neighbors if they are the endpoints of some edge.

Before generating a mesh, the surface must be reconstructed because the segmentation step produces an array of 3D points. The process of 3D surface generation from a point cloud is a well-studied problem in computer graphics and there are many techniques. Several approaches are based on combinatorial structures, such as Delaunay triangulations [12, 47], alpha shapes [31, 5], or Voronoi diagrams [1]. These schemes typically create a triangle mesh that interpolates all or most points. Other schemes directly reconstruct an approximate surface, typically represented in implicit form. They can be classified into global approaches and local approaches. Global fitting methods commonly define the implicit function as the sum of radial basis functions centered at the points [59, 18, 86, 45]. Local fitting methods consider subsets of nearby points at a time [41].

In the next section, we will focus on Poisson reconstruction [45], which combines the advantages of global and local schemes. It is a global approach that considers all data at once, without resorting to heuristic partitioning or blending, in contrast to the local approach. Thus, its algorithm reconstructs a smooth surface that robustly approximates noisy data. Moreover, the Poisson problem admits a simple hierarchy of locally supported functions that results in a well-conditioned sparse linear system. However, this technique tends to over-smooth the data and so important features would be missed. To fix this problem, the Poisson reconstruction algorithm is modified to incorporate positional constraints [46]. This new approach is called Screened Poisson Surface Reconstruction, where the term “screen” corresponds to a constraint that encourages the reconstructed isosurface to pass through the input points. Moreover, we show this new screened Poisson formulation.

Poisson surface reconstruction is a technique for creating surfaces from oriented point samples, so before showing the technique, let's see how to compute normal to point cloud.

Surface normal computation

For surface reconstruction over a 3D point cloud, each point has 3D coordinates and surface normals. The problem of determining the surface normal to a point from its coordinates is approximated by the problem of estimating the normal of a plane tangent to the surface. The solution for estimating the surface normal is therefore reduced to the Principal Component Analysis (PCA). PCA is used to find out the eigenvector and eigenvalues of a covariance matrix created from the nearest neighbors of the point in the point cloud. More specifically, for each point x_i, we calculate the covariance matrix Σ as follows:

$$\Sigma = \frac{1}{k}\sum_{i=1}^{k}(x_i - \bar{x}_i)\cdot(x_i - \bar{x}_i)^T \tag{4.2}$$

where k is the number of neighbors considered in the neighborhood of x_i and $\bar{x}_i = \frac{1}{k}\sum_{i=1}^{k} x_i$ is the 3D centroid of the nearest neighbors. T is the transpose operator.
The solution to the PCA problem may be defined as:

$$V^{-1}\Sigma V = D \tag{4.3}$$

where V is the matrix of eigenvectors which diagonalizes the covariance matrix Σ. D is the diagonal matrix of eigenvalues of Σ, where

$$\begin{cases} D_{jl} = \lambda_j & \text{for } j = l \\ D_{jl} = 0 & \text{for } j \neq l \end{cases}$$

λ_j is the j-th eigenvalue of the covariance matrix Σ. The eigenvalues and eigenvectors are ordered and paired, i.e., the j-th eigenvalue corresponds to the j-th eigenvector. The surface normal is the eigenvector of Σ with the smallest eigenvalue.

Poisson surface reconstruction

The surface reconstruction can be expressed as the solution of the Poisson equation [45]. This approach solves the surface reconstruction problem using the implicit function that

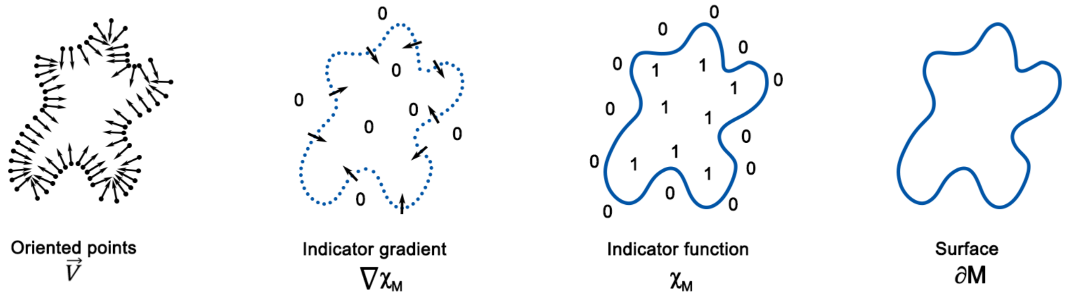

Figure 4.2 Illustration of Poisson reconstruction in 2D.

corresponds to the model's indicator function χ_M and extracting the iso-surface.

The key idea is that there is a relationship between the oriented points and the indicator function: the gradient of indicator function (Figure 4.2).

The 3D indicator function is defined as 1 at points inside the model, and as 0 at points outside it. The gradient of the indicator function is non-zero only at points near the surface as those areas have changes in the value of χ_M. Thus, the oriented point samples can be viewed as samples of the gradient of the model's indicator function. The indicator function is a piecewise constant function, and its gradient field is a vector field with unbounded values at the surface boundary. To fix this problem, Kazhdan *et al.* [45] smooth the indicator function calculating the convolution of itself with a smoothing filter and consider the gradient field of the new smoothed function. The relationship between the gradient of the smoothed indicator function and the surface normal field ($\overrightarrow{N}$) is formalized by the following lemma:

$$\nabla(\chi_M * F)(q_0) = \int_{\partial M} F_p(q_0)\overrightarrow{N}_{\partial M}(p)\,dp \tag{4.4}$$

where $F(q)$ is a smoothed filter, and $F_p(q) = F(q-p)$ its translation to the point p. $P = \{s_i = (p_1, n_1), \ldots, s_N = (p_N, n_N)\}$ is the input-oriented point set, that consists of a sample s_i with a position $s.p$ and an inward-facing normal $s.n$, assumed to lie on or near the boundary ∂M of an unknown model M.

The eq. (4.4) can be easily proved by considering each component. Here we will calculate only the spatial derivative along x and, similarly, do for y and z components.

$$
\begin{aligned}
\left.\frac{\partial}{\partial x}\right|_{q_0}(\chi_M * F) &= \left.\frac{\partial}{\partial x}\right|_{q=q_0}\int_M F(q-p)\,dp \\
&= \int_M \left(-\frac{\partial}{\partial x}F(q_0-p)\right)dp \\
&= -\int_M \nabla\cdot\left(F(q_0-p),0,0\right)dp \\
&= \int_{\partial M}\left\langle (F_p(q_0),0,0)\,,\overrightarrow{N}_{\partial M}(p)\right\rangle dp
\end{aligned}
\tag{4.5}
$$

the last equality follows from the Divergence Theorem.
Moreover, the gradient field of eq. (4.4) is approximated with a discrete summation:

$$
\begin{aligned}
\nabla(\chi_M * F)(q) &= \sum_{s\in S}\int_{P_S} F_p(q)\overrightarrow{N}_{\partial M}(p)\,dp \\
&\approx \sum_{s\in S}|P_S|F_{s.p}(q)s.\overrightarrow{N} \equiv \overrightarrow{V}(q)
\end{aligned}
\tag{4.6}
$$

where $P_s \subset \partial M$, is the area of the patch in which ∂M is partitioned and the integral over a patch P_s is approximated by the value at point sample $s.p$.
So, the problem is reduced to finding out the smoothed indicator function $\widehat{\chi}$, whose gradient is the best-fit of the vector field $\overrightarrow{V}$ defined by the input point cloud:

$$
\nabla\widehat{\chi} = \overrightarrow{V} \tag{4.7}
$$

However, an exact solution of eq. (4.7) does not generally exist because $\overrightarrow{V}$ is generally not integrable (i.e., $\overrightarrow{\nabla} \times \overrightarrow{V} \neq 0$). To find the solution, the divergence operator is applied to both sides of the equation to convert it to a standard Poisson problem:

$$
\Delta\widehat{\chi} = \nabla\cdot(\nabla\widehat{\chi}) = \nabla\cdot\overrightarrow{V} \tag{4.8}
$$

To solve the eq. (4.8), a Galerkin formulation is used [96] to transform this into a finite-dimensional system. The indicator function, χ, needs to be represented using an adaptive octree in 3D space, rather than a regular 3D grid. This provides an accurate representation of the implicit function only near the reconstructed surface.
The positions of the sample points are used to define an octree O. A trivariate B-spline function F_i, centered on the node i and stretched by the size of i, is associated with each octree node $i \in O$. The B-spline F_i is translated to the node center and scaled by the size of the node, and the span F of the translated and scaled B-splines defines the function-space

over which the eq. (4.8) is solved. Concerning this basis, we let:

$$\widehat{\chi}(q) = \sum_{i=1}^{N} x_i B_i(q) \tag{4.9}$$

the coefficients $\{x_i\}$ of the solution reduces to solving the linear system $Lx = b$, where:

$$L_{ij} = \int \left\langle \nabla B_i(q), \nabla B_j(q) \right\rangle dq \tag{4.10}$$

$$b_j = \int \left\langle \nabla B_i(q), \overrightarrow{V}(q) \right\rangle dq \tag{4.11}$$

Screened Poisson surface reconstruction

Some years later, the same authors of Poisson Surface Reconstruction [45] defined the Screened Poisson Surface Reconstruction [46], that improved the first algorithm by reducing the computation time and creating higher-quality surface reconstructions.
In this new formulation, the coefficients $\{x_i\}$ of the solution χ with the basis $F = \{F_1, F_2, ..., F_N\}$ are again obtained by solving the linear system $Lx = b$, in which:

$$L_{ij} = \int \left\langle \nabla B_i(q), \nabla B_j(q) \right\rangle dq + \alpha \sum_{p} B_i(p) B_j(p) \tag{4.12}$$

where α is the Screening Parameter, for which Kazhdan *et al.* [46] have found empirically that a value of $\alpha = 4$ works well for many types of datasets. Concerning eq. (4.10), a dualized screening term has been added to eq. (4.12). This added term corresponds to a soft constraint that support the reconstructed surface to pass through the input point. Conversely, the b term in eq. (4.11) is unchanged.
The new linear system can be interpreted as a screened Poisson equation:

$$(\Delta - \alpha I)\widehat{\chi} = \nabla \cdot \overrightarrow{V} \tag{4.13}$$

where I is the identity operator.

4.1.3 Mesh parameterization

The transformation of a 3D surface into a 2D map is known as the surface parameterization process. If the surface is a mesh, the problem is known as mesh parameterization. The output of this process is a uv-map where each vertices coordinate (x,y,z) of the 3D mesh is associated with a coordinate (u,v) in the uv-map.

In the following sections, we will describe two mesh parameterization algorithms that compute uv-maps. Before we go into the details of algorithms, let us quickly review some of the basic properties from differential geometry that will be essential for understanding the motivation behind the methods described later.

Metric distortion

Parameterizations almost always introduce distortion in angles or areas because there is a loss of information when moving from a higher to a lower-dimensional space [33, 42]. A good parameterization is one that minimizes these distortions. Only the developable surface, such as flat plane, cone, and cylinder, can be mapped from 3D to 2D without error, i.e., without metric distortions, displayed as stretching and shearing in the images. To quantify the metric distortion, we take some basic theory of differential geometry.

Suppose a surface $S \subset R^3$ which has the following parametric representation:

$$f(u,v) = (x(u,v), y(u,v), z(u,v))$$

for point (u,v) in the parameter domain Ω in R^2. Let's assume that the function $x(u,v), y(u,v)$ and $z(u,v)$ are differentiable as many time as we need and the vectors

$$f_u = \frac{\partial f}{\partial u}, \qquad f_v = \frac{\partial f}{\partial v} \tag{4.14}$$

are linearly independent at every point (i.e.: $f_u \times f_v \neq 0$) and span the local tangent plane of S and by simply taking their cross product and normalizing the result we get the surface normal (n_f):

$$n_f = \frac{f_u \times f_v}{||f_u \times f_v||} \tag{4.15}$$

To mathematically define the metric distortion, let us see what happens to the surface point $f(u,v)$ when we move by an infinitesimal amount $(\Delta u, \Delta v)$ away from (u,v) in the parameter domain. The new surface point $f(u+\Delta u, v+\Delta v)$ is approximately given by the first-order Taylor expansion $\widetilde{f}$ of f around (u,v):

$$\begin{aligned} \widetilde{f}(u+\Delta u, v+\Delta v) &= f(u,v) + f_u(u,v)\Delta u + f_v(u,v)\Delta v \\ &= f(u,v) + \mathbf{J}_f(u,v)\begin{pmatrix}\Delta u \\ \Delta v\end{pmatrix} \end{aligned} \tag{4.16}$$

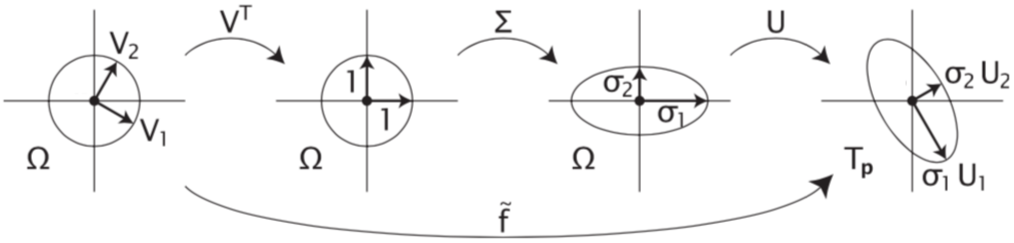

Figure 4.3 SVD decomposition of the mapping $\widetilde{f}$.

where $\mathbf{J}_f(u,v) = (f_u, f_v)$ is a 3x2 matrix known as the Jacobian of f, i.e., a matrix with the partial derivatives of f as column vectors. Using the singular value decomposition (SVD) of the Jacobian:

$$\mathbf{J}_f = \mathbf{U}\Sigma\mathbf{V}^T = \mathbf{U}\begin{pmatrix}\sigma_1 & 0\\ 0 & \sigma_2\\ 0 & 0\end{pmatrix}\mathbf{V}^T \tag{4.17}$$

with singular values $\sigma_1 \geq \sigma_2 > 0$ and orthonormal matrices $U \in R^{3x3}$ and $V \in R^{2x2}$. We can split up the linear transformation $\widetilde{f}$ as shown in Figure 4.3:

1. the transformation V^T first rotates all points around (u,v) such that the vectors V_1 and V_2 are in alignment with the parameter domain axes;

2. the transformation Σ then stretches everything by the factor σ_1 in u- and by σ_2 in v-direction;

3. the transformation U maps the unit vectors to the vectors U_1 and U_2 in the tangent plane T_p at $f(u,v)$.

This transformation of circles into ellipses is called a local metric distortion of the parameterization. All information about this local metric distortion is hidden in the singular values σ_1 and σ_2.

The singular values of $\mathbf{J}_f$ can be calculated as the square roots of the eigenvalues of the matrix $\mathbf{J}_f^T\mathbf{J}_f$:

$$\mathbf{J}_f^T\mathbf{J}_f = \begin{pmatrix}f_u^T\\ f_v^T\end{pmatrix}(f_u f_v) = \begin{pmatrix}f_u\cdot f_u & f_u\cdot f_v\\ f_v\cdot f_u & f_v\cdot f_v\end{pmatrix} = \begin{pmatrix}E & F\\ F & G\end{pmatrix} = \mathbf{I} \tag{4.18}$$

$\mathbf{J}_f^T\mathbf{J}_f$ is the first fundamental form, where the product between the partial derivatives is the usual dot product in R^3. Now we can easily compute the two eigenvalues λ_1 and λ_2 of this symmetric matrix by:

$$\lambda_{1,2} = \frac{1}{2}\left((E+G) \pm \sqrt{4F^2 + (E-G)^2}\right) \tag{4.19}$$

We summarize the main properties that a parameterization can have locally:

$$\begin{aligned}
f\text{is isometric or length-preserving} &\iff \sigma_1 = \sigma_2 = 1 &&\iff \lambda_1 = \lambda_2 = 1\\
f\text{is conformal or angle-preserving} &\iff \sigma_1 = \sigma_2 &&\iff \lambda_1 = \lambda_2\\
f\text{is equiareal or area-preserving} &\iff \sigma_1\sigma_2 = 1 &&\iff \lambda_1\lambda_2 = 1
\end{aligned}$$

Isometric parameterization is ideal but rare. In practice, conformal, equireal and some balance between them are used.

We now review two different methods that compute a conformal parameterization: Least Square Conformal Mapping and Angle Based Flattening.

Least Squares Conformal Mapping (LSCM)

Developed by Levi *et al.* [50], the Least Square Conformal Mapping (LSCM) is a conformal parameterization technique that computes parameterized coordinates (u, v) for each vertex (x, y, z) such that the Cauchy-Riemann equations are minimized in the least-squares sense. A conformal mapping f satisfies the Cauchy- Riemann conditions:

$$\frac{\partial u}{\partial x} = \frac{\partial v}{\partial y}, \qquad \frac{\partial u}{\partial y} = -\frac{\partial v}{\partial x} \tag{4.20}$$

In general, however, for piecewise linear functions such as triangulated meshes, there are no conformal mappings. To fix this problem, Levy *et al.* [50] defined the conformal energy, that is a measure of non-conformality of the application, for triangle t, E_t, as:

$$E_t = (\sigma_{1,t} - \sigma_{2,t})^2 \tag{4.21}$$

This energy is invariant to arbitrary translations and rotations in the parametric space. LSCM minimizes the energy for all triangles in a mesh, so the equation to minimize is:

$$\sum_{t \in T} E_t A_t \tag{4.22}$$

where T is the set of triangles in the mesh and A_t is the area of each triangle t. To have a unique minimizer, it is required to fix at least two vertices on the boundary of the mesh. This

request affects the results significantly.
Eq. (4.22) satisfies eq. (4.20) and leads to a linear system that can be solved straightforwardly. The solution of eq. (4.22) yields the coordinates (u,v) for every vertex.

Angle Based Flattening (ABF)

While LSCM defines a planar parameterization in terms of vertex coordinates, the Angle Based Flattening (ABF) method defines it in terms of the angles of the triangles.
To find a set of 2D coordinates, Sheffer *et al.* [82] used the 3D angles to find a set of 2D angles which are then used to compute the 2D coordinates to form a *uv*-map. The algorithm uses an objective function to minimize the relative error between the parameterized angles (θ) of the output and a set of the original 3D angles (α) of the mesh. This objective function is:

$$\sum_{t\in T}\sum_{i=1}^{3} w_i^t \left(\theta_i^t - \alpha_i^t\right)^2, \qquad w_i^t = \frac{1}{\left(\alpha_i^t\right)^2} \tag{4.23}$$

At eq (4.23), to maintain the connectivity and validity of the resulting parameterized angles, the following constraints must be imposed:

- for each triangle $t \in T$:

  $\theta_1^t + \theta_2^t + \theta_3^t - \pi = 0$

  where θ_i^t is the *i*th angle of the triangle;

- for each internal vertex v in the final triangulation:

  $\sum_{(t,k)\in\theta(v)} \theta_k^t - 2\pi = 0$

  where $\theta(v)$ is the set of angles incident to vertex v;

- ensure that edge shared by pair of triangles have the same length:

  $\prod_{(t,k)\in\theta(v)} \sin(\theta_{k+1}^t) - \prod_{(t,k)\in\theta(v)} \sin(\theta_{k-1}^t) = 0$

  where the indices $k+1$ and $k-1$ denotes the next and the previous angle within the triangle t.

It is necessary to set the position and size of a single edge in the parameterized space to determine the (u,v) coordinates of all vertices in the mesh. This placement, in combination with final computed angles, is enough to have the parameterized mesh.

Chapter 5

Results

5.1 Experiments of Herculaneum papyri rolls and fragments

With the kind cooperation of the *Biblioteca Nazionale di Napoli*, two experiments were planned and undertaken in September 2015 in Grenoble and in November 2018 in Bari.

5.1.1 X-ray Phase Contrast Tomography experiment

The first experiment was performed on September 2015 at the ID17 biomedical beamline of the European Synchrotron Radiation Facility (ESRF) in Grenoble (France) (see Figure 5.1).

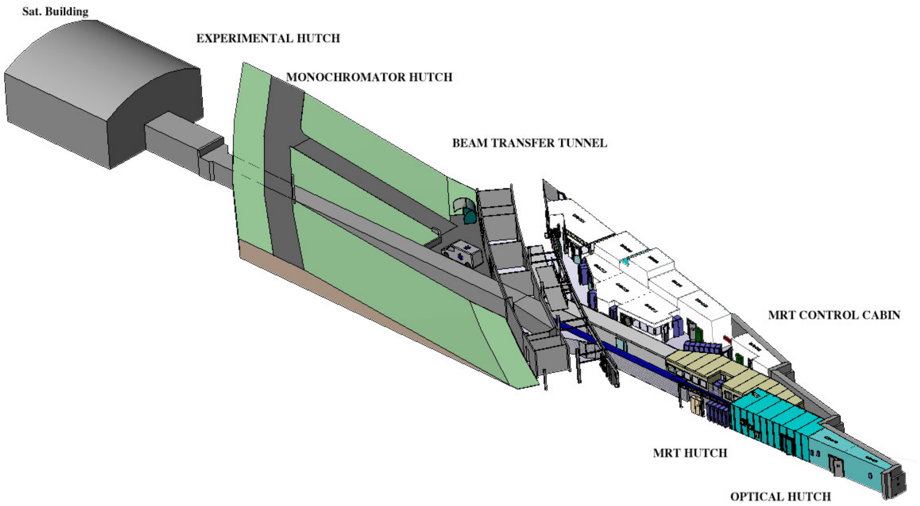

Figure 5.1 ID17 layout.

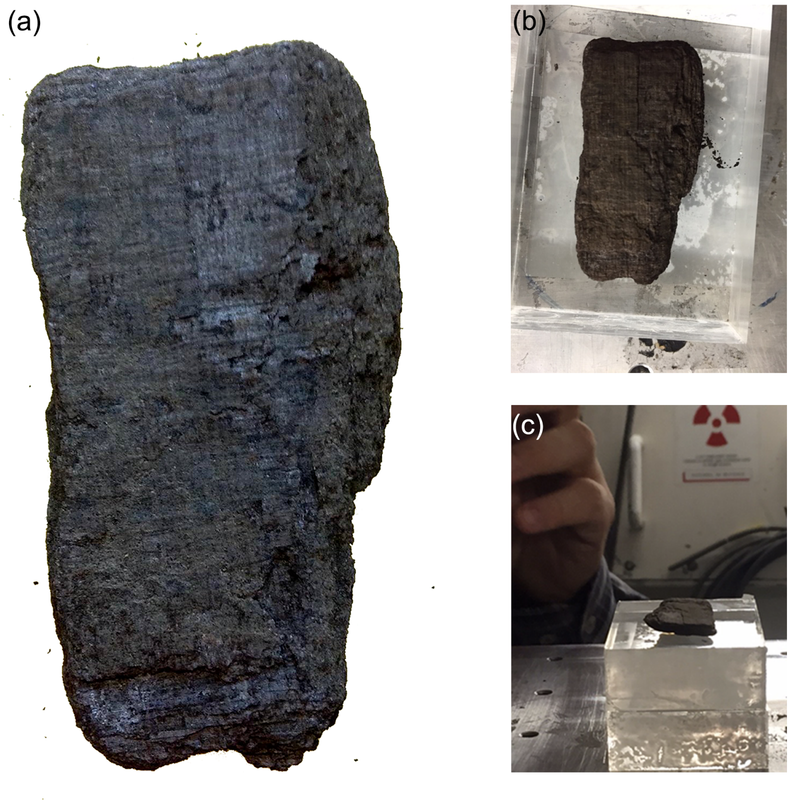

Figure 5.2 Contrast and brightness enhanced photographs of the *PHerc.1103*.

During the XPCT experiment two fragments, *PHerc.1103* (see Figure 5.2) and *PHerc.1105* (see Figure 5.3) and two original papyrus rolls, *PHerc.375* and *PHerc.495* (whose results are not the subject of this thesis) were investigated.
The analyzed fragments are mounted in two different cornice, housed in the *Officina dei Papiri Ercolanesi* at the *Biblioteca Nazionale* in Naples (Italy).
According to the "Catalogo dei papiri ercolanesi" [36], *PHerc.1103* and *PHerc.1105* are two *scorze*. The name *scorze* refers to the last layers of papyrus peeled from the lumps of carbonized papyri. *Scorza* is the most damaged part of papyrus due to thermal shock and pressure and to handling after their discovery. It deserves an in-depth analysis: the very precious information relating to the author, the title and the length of the work often were reported at the end of the roll, therefore they could be contained right in this portion of the papyrus.

Both *scorze* consist of several papyrus layers fused weighing less than $7g$ and their dimensions are approximately $3 \times 5,5cm^2$ (*PHerc.1103*) and $2 \times 1,2cm^2$ (*PHerc.1105*). They are in extremely poor condition and are illegible.

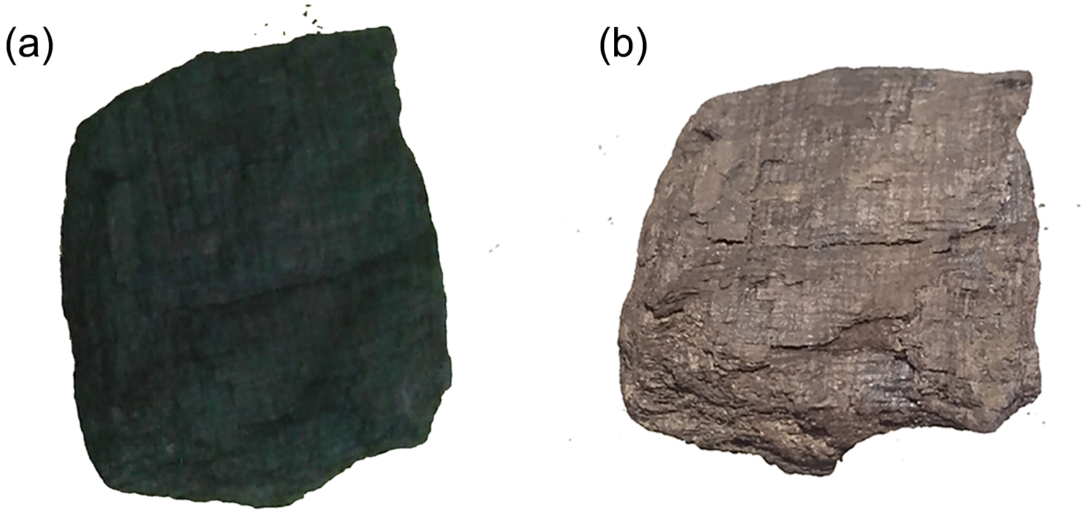

Figure 5.3 Contrast and brightness enhanced photographs of the *PHerc.1105*.

The experiment consisted of free-space propagation that was described previously (see Section 3.3) and a schematic of the set-up is shown in Figure 5.4.

To achieve an optimal contrast, multi-energy scans were performed. The X-ray beam was monochromatized at three different energies, $30, 51, 80 keV$, using a Si (111) crystal system. The imaging detector was a Fast Readout Low Noise (FReLoN) 2k charge-coupled device camera (CCD) with an effective pixel size of $47 \times 47 \mu m^2$. The field of view (FOV) was approximately $1mm$ (vertical) $\times 75mm$ (horizontal). Because of limited vertical FOV, multiple vertical scanning required to cover the full volume of the sample. This was achieved by acquiring about a $1mm$ thick full data set of the sample at a given vertical position, then shifting the sample vertically by less than $1mm$, to create a small overlap and avoid missing information. The procedure was repeated four times to cover the entire length.
The samples were placed downstream of the monochromator, on the translation and rotation stage. The object-to-detector distance was approximately $10m$. Since the samples were carbonized and extremely fragile, to avoid their physical damage, we have simply placed them horizontally on the rotation stage (see, for example, Figure 5.2(c)).
For each energy, 2000 projections were recorded for each vertical position, covering a total angle range of 180°, with an acquisition time of 0.05 seconds per point. Furthermore, for each scan, a dark field image (acquired when the X-ray source is turned off) and 20 flat field images (i.e., images acquired when the X-ray source is turned on but without the sample) were taken. The flat field images were averaged and, with the dark field image, used to normalized the projections for beam and detector non-uniformities.

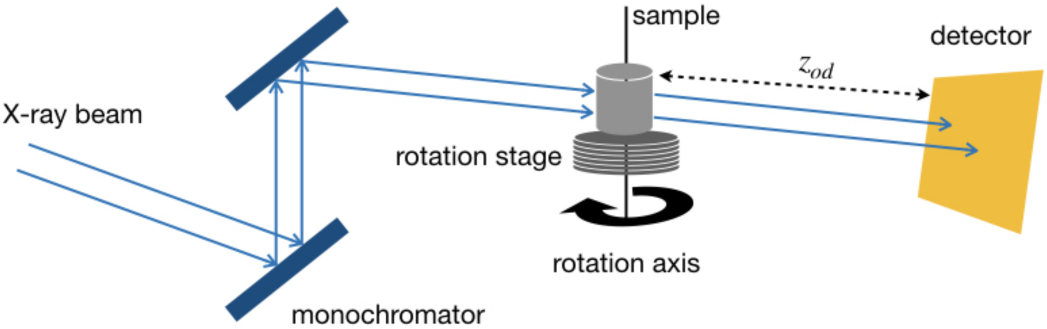

Figure 5.4 The schematization of an experimental set-up for the Free Space Propagation technique.

5.1.2 X-ray-micro-computed Tomography experiment

The second experiment took place in November 2018 at Laboratory of *Università degli Studi di Bari "Aldo Moro"*.

During the μX-CT experiment, one fragment of *PHerc.110* (see Figure 5.5) was investigated.

According to the “Catalogo dei papiri ercolanesi” [36], *PHerc.110* was partially unrolled in September 1867 by Vincenzo Corazza through the Piaggio machine. Six fragments of similar sizes for a total length of 1.741m were obtained from this operation.

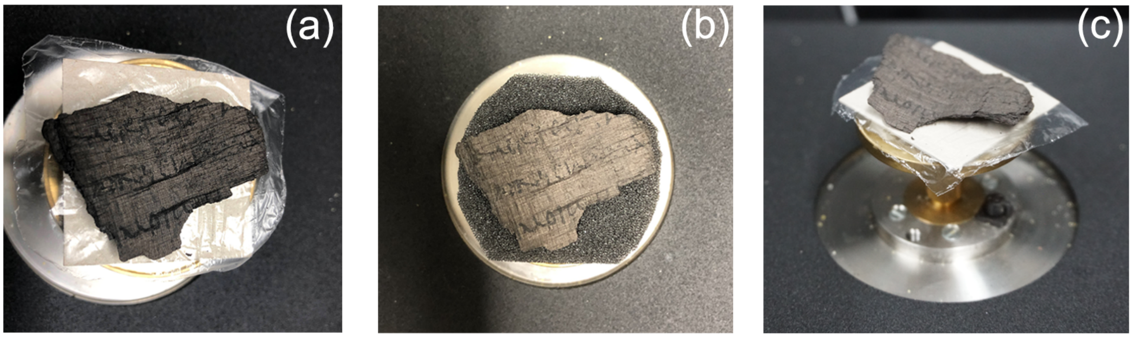

Figure 5.5 Contrast and brightness enhanced photographs of the *PHerc.110*.

Figure 5.6 Bruker SkyScan 1172 high-resolution μX-CT scanner.

These fragments are mounted in three cornice, housed in the *Officina dei Papiri Ercolanesi* at the *Biblioteca Nazionale* in Naples (Italy).
The analyzed fragment is approximately $4 \times 4cm^2$. It consists of several compressed and illegible papyrus layers.

X-ray imaging was carried out using a Bruker SkyScan 1172 high-resolution μX-CT scanner (see Figure 5.6 and Figure 5.7).
The system is equipped with a polychromatic microfocus X-ray tube and it employed a cooled CCD camera with a pixel size of $12 \times 12\mu m^2$. The field of view (FOV) was $50mm$ whereby a single scan was enough to image the whole thickness.
To improve image quality, the manufacturer suggests that the minimum value of transmittance should be $30-40\%$ because a low value would produce a dark image, while a high value would provide a blurred image. The optimal value of the minimum transmittance is obtained by changing the current-voltage and inserting filters. The scan was performed at $60kV$ and $167mA$ with added filtration (0.5 Al). The exposure time was $2,4s$.

Also, in this case, we placed the fragment horizontally on the rotation stage inside the scan chamber (see Figure 5.5) to avoid the physical damage of the sample.

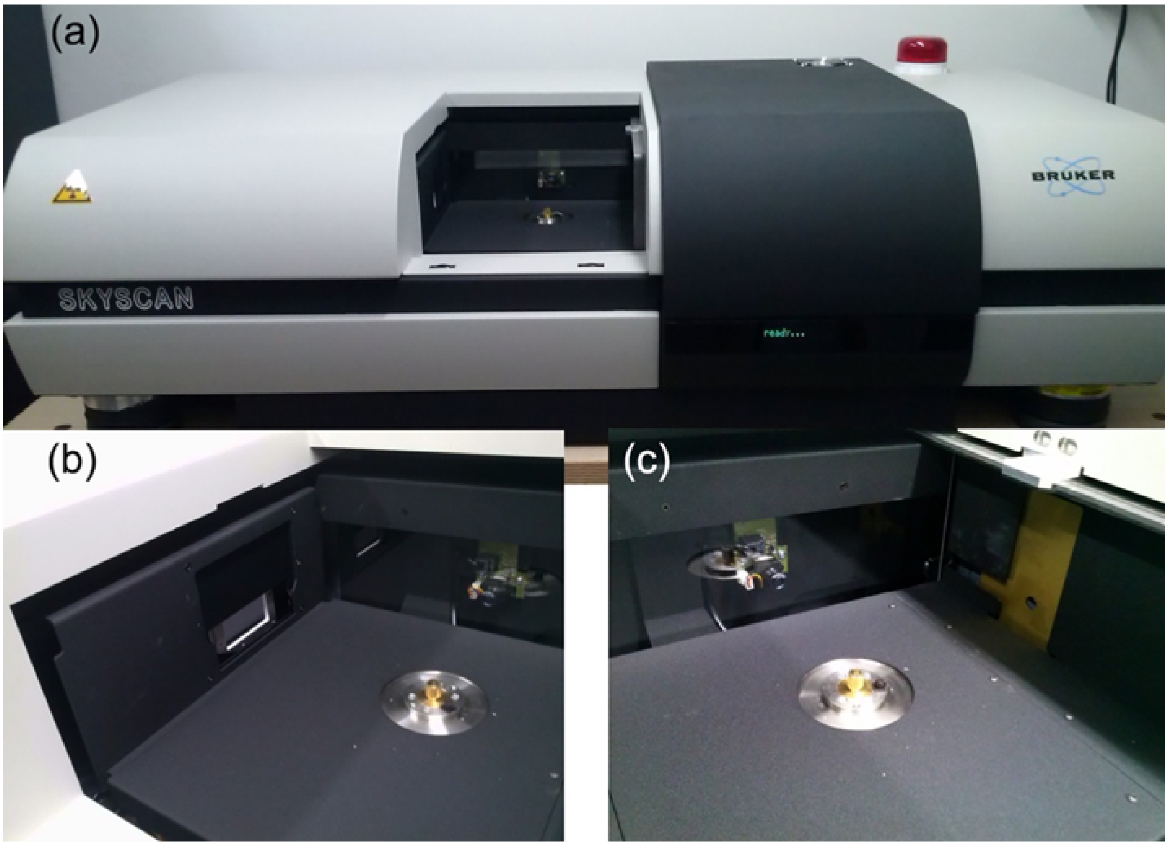

Figure 5.7 Components of the SkyScan 1172 scanner: a) sample holder; b) acquisition system; c) X-ray generator.

5.2 Different Phase retrival approaches

Projection images acquired with an XPCT experiment (Section 5.1.1) contain mixed information related to both the object's attenuation and refraction properties. The latter causes a phase variation in the incident beam. To extract the phase information, over the years, different phase retrieval methods were developed. An overview of the methods is given in [16].

In this thesis work, I tested three methods: modified Bronnikov algorithm [37], phase-attenuation duality [89, 90], and Paganin algorithm [63]. All these three methods follow the same workflow (outlined in Figure 5.8):

$$\phi(x,y) = f\left(\mathscr{F}^{-1}\left\{H_p(u,v)\cdot\mathscr{F}\left[g(I(x,y))\right]\right\}\right) \tag{5.1}$$

where the functions are tabulated in Table 5.1. For more detail see Section 3.3.5.

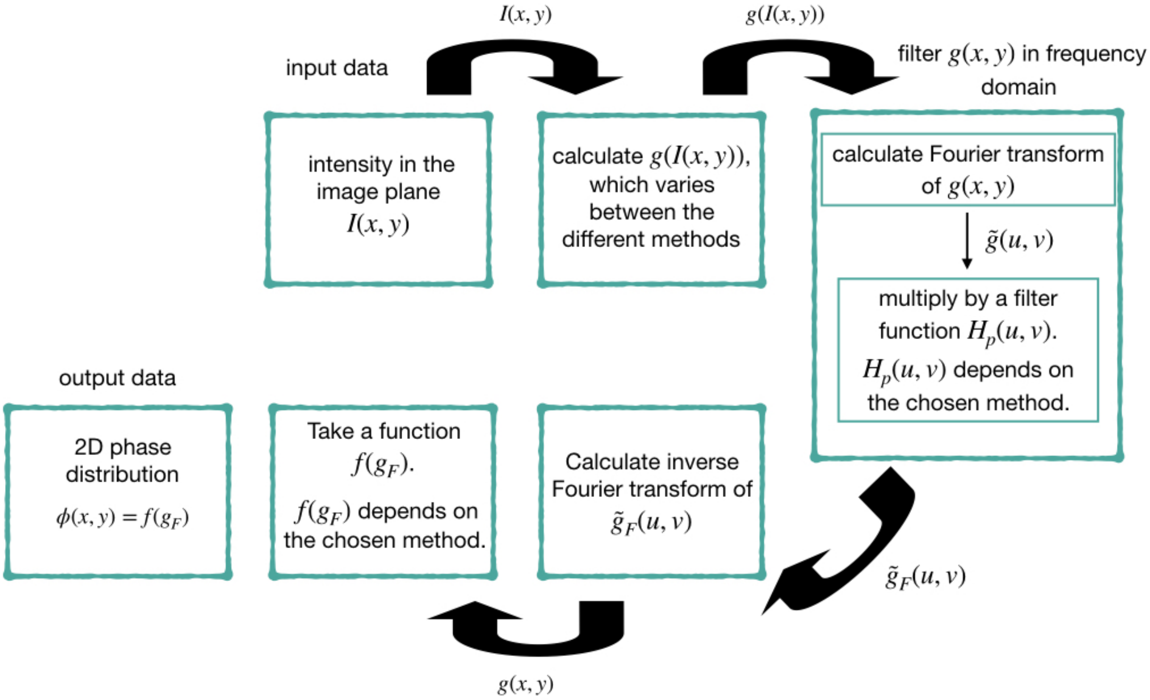

Figure 5.8 General process of phase retrieval.

The implementation of the three algorithms is designed by me in the Python language. The Python programming language was chosen to facilitate interaction with the existing TomoPy [40]. This Python-based framework for the analysis of synchrotron tomographic data, is open-source, platform- and data-format-independent. TomoPy includes several pre-processing and post-processing algorithms commonly used.

NumPy (http://numpy.scipy.org) is used for data manipulation. It is part of the "Scientific Computing Tools For Python" or SciPy (https://scipy.org) package available in Python. For example, Fourier transformations are performed using the numpy.fft package. In particular, the rfft2 and irfft2 functions. These functions compute the 2-dimensional discrete Fourier transform (and inverse Fourier transform) with the efficient Fast Fourier Transform (FFT) algorithm [28].

Data of *PHerc.1103*, at energy $80 keV$, was used to compare the performance of the three retrieval methods. Figure 5.9 presents reconstructed XPCT images of the *PHerc.1103*, processed with the (a) modified Bronnikov algorithm, (b) phase-attenuation duality algorithm, and (c) Paganin algorithm.

For modified Bronnikov and Paganin approaches, several different values of the algorithm

Method	$g(I(x,y))$	$H_p(u,v)$	$f(g_F(x,y))$
Modified Bronnikov	$\frac{I_d}{I_0}-1$	$\frac{1}{2\pi\lambda d(f_x^2+f_y^2)+\alpha}$	g_F
Phase-attenuation duality	$\frac{I_d}{I_0}$	$\frac{1}{2\pi\frac{r_e\lambda^2 d}{\sigma_{KN}}(f_x^2+f_y^2)+1}$	$\frac{\lambda r_e}{\sigma KN} ln g_F$
Paganin	$\frac{I_d}{I_0}$	$\frac{1}{4\pi^2 d\delta/\mu(f_x^2+f_y^2)+1}$	$-\frac{1}{\mu} ln g_f$

Table 5.1 The functions $g(I(x,y))$, $H_p(u,v)$, and $f(g_F(x,y)$ of eq.(5.1) for modified Bronnikov, phase-attenuation duality, and Paganin algorithm.

parameter (α and δ/μ, respectively) were tried. Here we show the results with the optimal parameters.

The phase-attenuation duality image in Figure 5.9 (b) is not as sharp as the others, and the smallest structures are not reconstructed. The modified Bronnikov method (Figure 5.9 (a)) and the Paganin method (Figure 5.9 (c)) both give good results. Though derived differently, they are very similar and will give similar results.

For subsequent analyses, Paganin's algorithm is chosen to phase retrieve our data.

5.3 Multi-energy analysis

Multi-energy scans were performed on the fragments: incident X-ray beam was monochromatized at three different energies: 30, 51, and $80keV$. Figure 5.10 shows a single slice reconstructed at different energies: (a) $330keV$, (b) $51keV$, and (c) $80keV$.

The multi-energy analysis provides information related to the varying response of materials to X-rays of different energies. Material differentiation and elemental decomposition thus become possible with the application of different energy.

Figure 5.10 shows that for high energies, the fibers are more visible. These, as we will see in the next paragraphs, are essential to understand if our sheet identification and the unrolling procedure are correct. Furthermore, the choice of energy is one of the essential conditions to achieve a suitable contrast in the final recorded images. Figure 5.10 (c), the one with energy equal to $80keV$, shows the best contrast. Therefore, the data acquired at $80keV$ will be used in the next analysis concerning the *PHer.1103*.

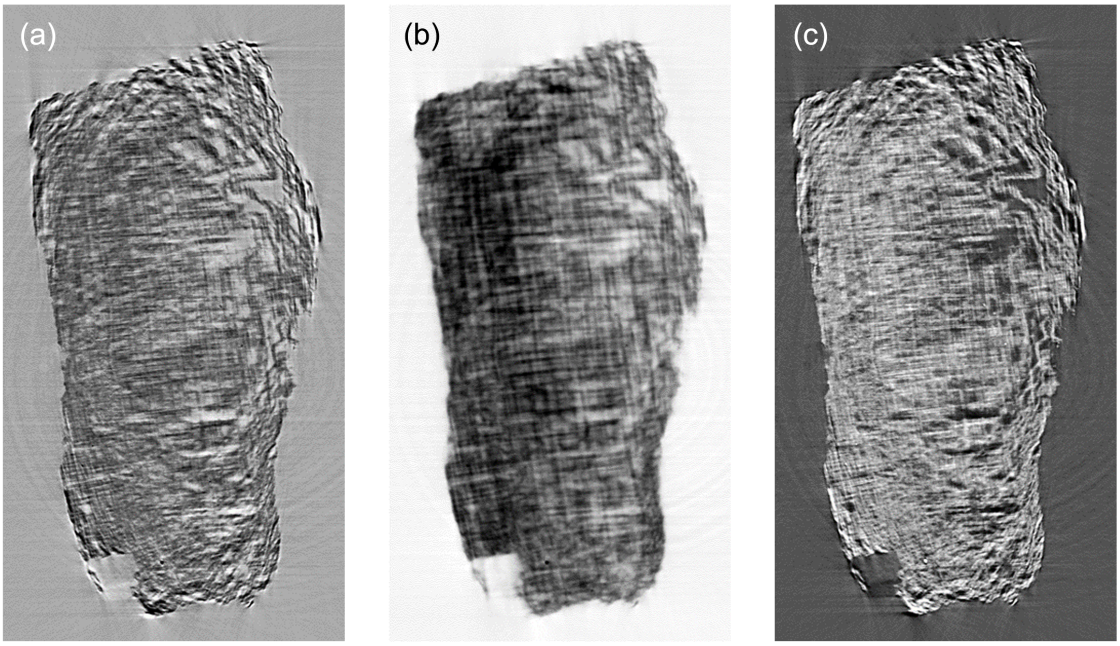

Figure 5.9 The retrieved phase of *PHerc.1103*. The phase is retrieved using (a) the modified Bronnikov method, (b) the phase-attenuation duality, (c) the Paganin algorithm.

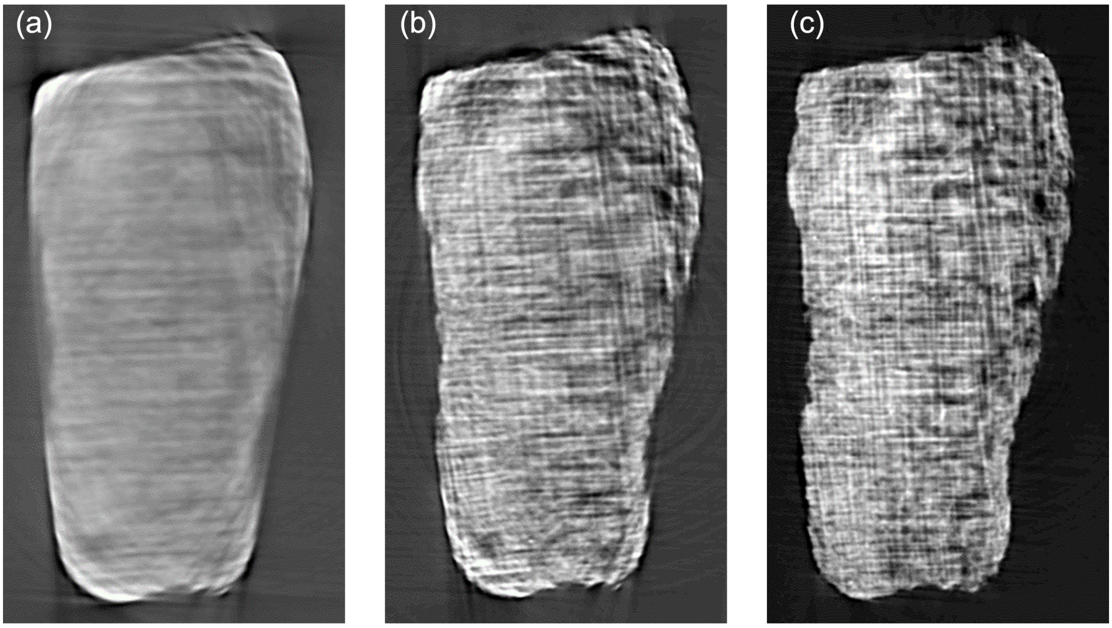

Figure 5.10 A single slice of *PHerc.1103* at different energy (a) $30 keV$, (b) $51 keV$, and (c) $80 keV$.

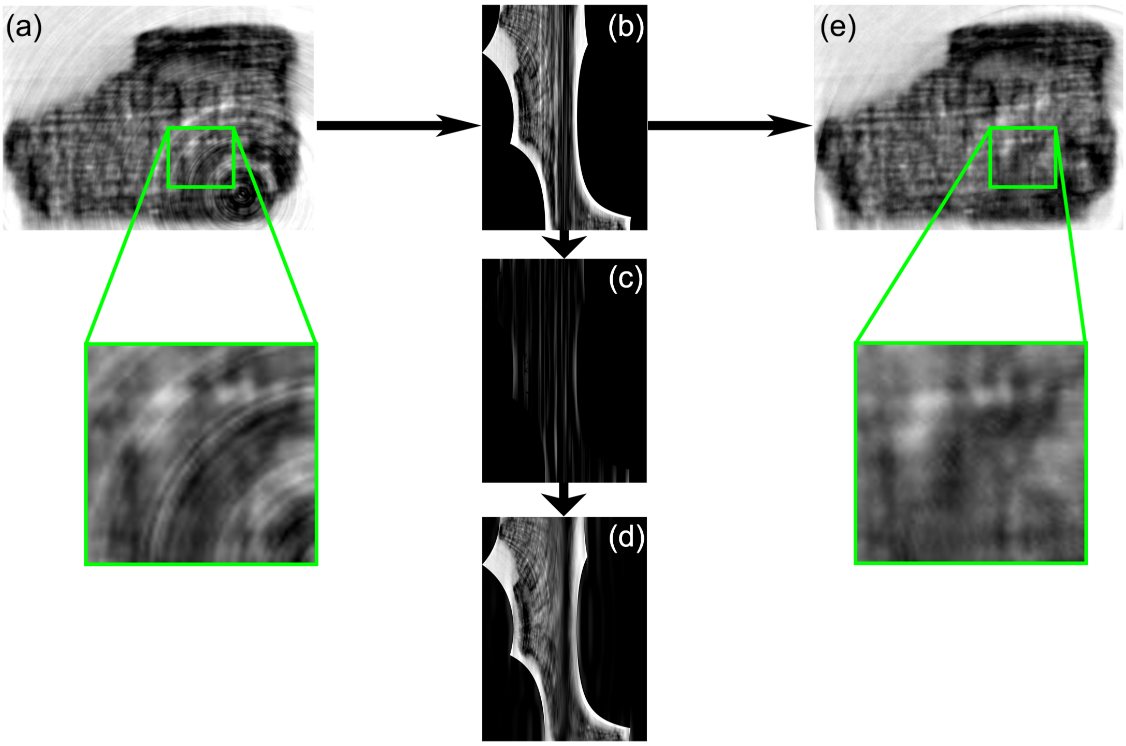

Figure 5.11 Ring artifacts removal: (a) shows a reconstructed slice without the application of any ring correction algorithm. Inset: zoom of an image portion to display the effect of the artifact; (b) slice transform into polar coordinates so that the artifact becomes a vertical line: (c) isolated, and (d) eliminated applying a wavelet-based filtering approach; (e) shows the same slice after the transformation into cartesian coordinates. Inset: zoom of an image portion to display the effect of the stripe filtering.

5.4 Artifact removal

In the image processing pipeline for phase-contrast tomography, a flat-field and a dark-field correction are always performed (see Section 2.7). It corrects offsets and sensitivity differences between pixels assuming that the response is linear and not altered by other factors. These constraints are, however, not always fulfilled, and ring artifacts still occur in the reconstruction that disturbs the image impression.

Two types of image processing techniques for the removal of ring artifacts exist i) the first type acts on the sinogram before reconstruction; ii) the second acts on the reconstructed images.

For our samples, it is important not to use other pre-filtering algorithms to avoid losing important information, such as writing. Thus the ring removal process performed on the images of this thesis belongs to the second type, i.e., post-reconstruction type.

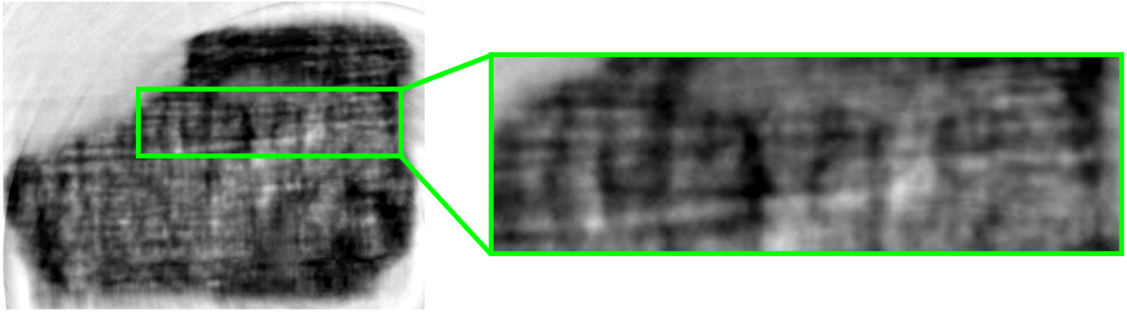

Figure 5.12 Zoom of a line: word recognizable through the ring artifacts removal.

A suitable approach to remove such artifacts is to filter the image. For this thesis, an ImageJ macro was used to remove the rings. The approach is as follows (Figure 5.11): the image that presents the artifact is considered (Figure 5.11(a)); it is transformed into polar coordinates, with the center of the transformation coinciding with the center of the rings (Figure 5.11(b)) so that the artifact becomes a vertical line making its removal easier.
Striping artifacts are erased by a technique based on the combination of wavelet and Fourier transform [58]. This algorithm is included in 'Xlib' plugins for ImageJ (https://imagej.net/Xlib). This filtering approach is then used to isolate the artificial lines (Figure 5.11(c)), that will be subtracted from the initial image (Figure 5.11(d)). In particular, Daubechies 15 tap wavelets were used and the first six components are filtered with $\sigma = 4$. Finally, the image transformation in the Cartesian coordinates is done, and the result of the ring removal process is visible in Figure 5.11(e).

The artifacts removal process allows the visualization of clean slices and helps to reveal traces compatible with writing (see Figure 5.12). A distinct word, compatible with $\delta\eta\mu o\sigma$ (dèmos) were detected in the zoom of Figure 5.12.

5.5 Unfolding

The use of the XPCT or the μX-CT provides a digital copy of papyrus fragments as 3D volumetric objects, see Figure 5.13 (right) for *PHerc.1103*, and Figure 5.14 (right) for *PHerc.110*. These two historical papyrus fragments, belonging to different scrolls of Herculaneum, are different in properties, dimensions, and geometries.

Upon first glance at cross-sections of these papyri, the compactness of the several papyrus layers is immediately apparent (Figure 5.13 (left) for *PHerc.1103*, and Figure 5.14 (left) for *PHerc.110*). So the Herculaneum papyri present unique challenges.
We employed the data of these two fragments to develop an unfolding procedure.

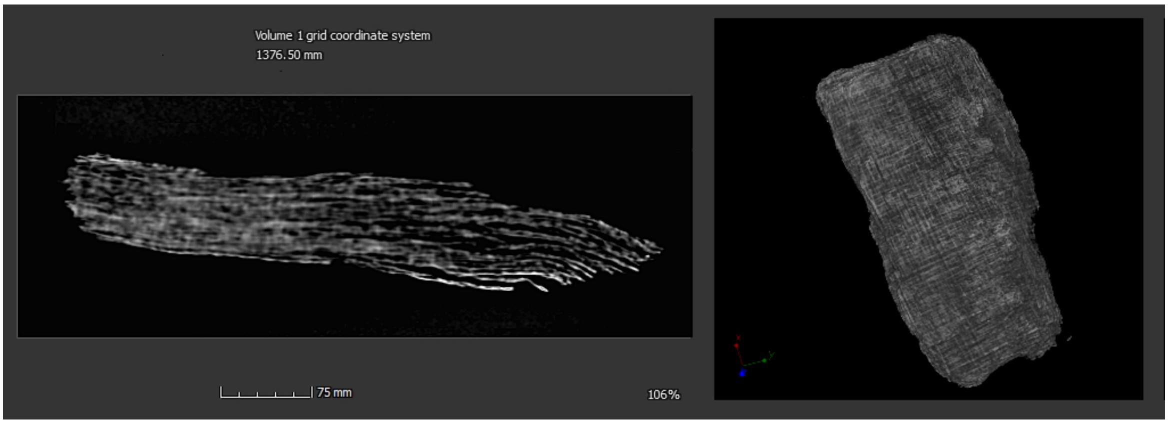

Figure 5.13 *PHerc.1103*: cross-section (left) and 3D rendering (right).

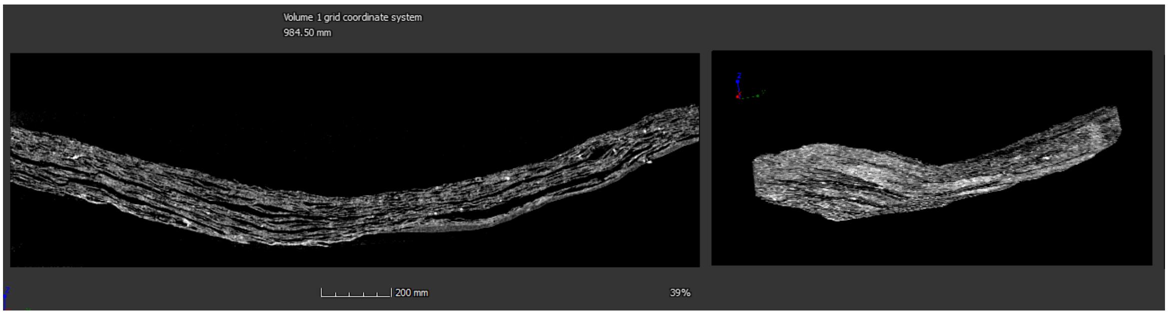

Figure 5.14 *PHerc.110*: cross-section (left) and 3D rendering (right).

The pipeline for the virtual 3D unfolding of the Herculaneum papyri fragments is schematized in Figure 4.1 and involves the following steps: surface segmentation, meshing and reconstructing the surface, mesh parameterization, and texture mapping (for the detailed description of the pipeline see Section 4.1).

The remainder of this chapter is organised as follows. Section 5.5.1 addresses the segmentation stages. Section 5.5.2 details its surface modelling, followed by the flattening stage in Section 5.5.3. In this last section, we consider related problems to fragments unfolding in more detail and evaluate our algorithm.

5.5.1 Surface segmentation

The identification of the 3D papyrus sheet starting from 3D volume is one of the main steps for the unfolding procedure. Figure 5.13 (left) and Figure 5.14 (left) show the cross-section of the tomographic volume of *PHerc.1103* and *PHerc.110*, respectively. As can be observed, the different sheets that form the fragments appear convoluted and difficult to distinguish one from the other. Due to deformations at a small and large scale, it is arduous to find sheet

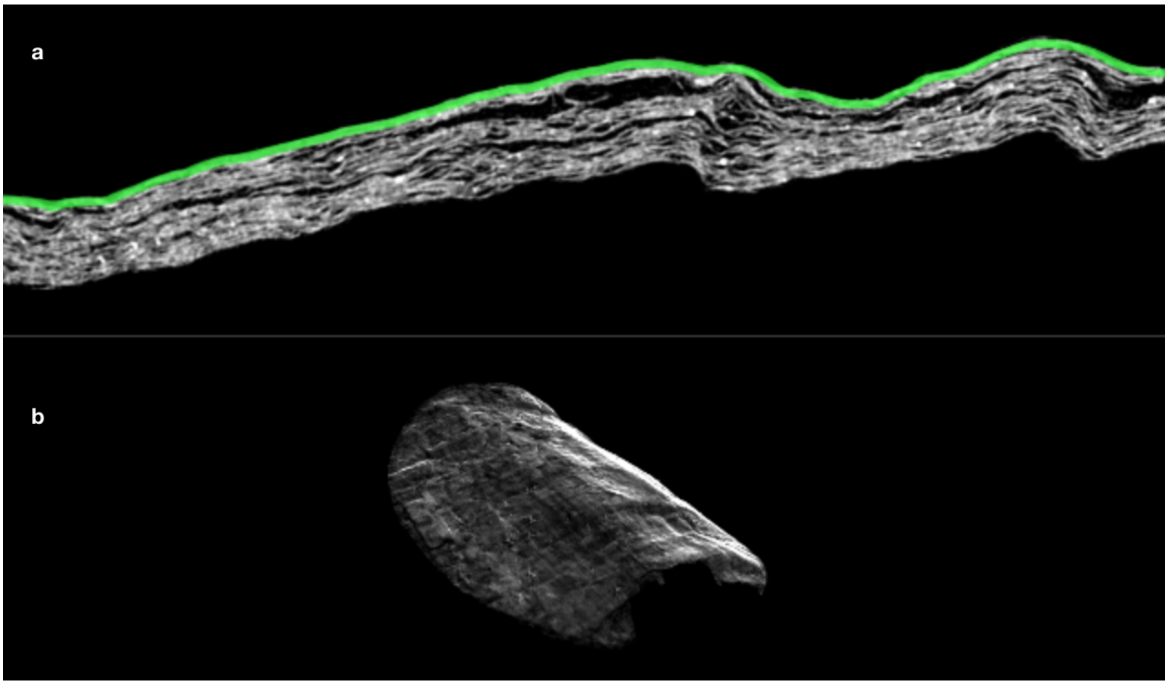

Figure 5.15 (a) The cross-section of the tomographic volume of *PHerc.110* overlaid with its segmented sheet (green line) and (b) 3D image of the sheet of the fragment *PHerc.110* segmented.

portions even only locally uniform.

The surface extraction, i.e., the segmentation of a single papyrus sheet, was performed by a semi-manual procedure (described in detail in Section 4.1.1), because of the complicated structure and arrangement of the sheets. I have developed macros and codes using image processing program ImageJ and Python for this procedure.

The segmentation results are illustrated in Figure 5.15(a) for *PHerc.110*. The segmentation results are quite similar for all slices of the same fragment, so the picture is representative of the segmentation performance for the whole data set.

Thanks to this step we can identify and isolate the sheet, whose 3D rendering is shown in Figure 5.15(b) of *PHerc.110*. The same segmentation procedure was applied as well on XPCT data of fragment *PHerc.1103* (the images of the segmentation procedure of fragment *PHerc.1103* are not present because they are similar to those shown in Figure 5.15(a)).

5.5.2 Meshing and reconstructing the surface

The previous step produces a set of 3D data points in space characterized by the intensity value associated with them, i.e., a colored point cloud. Starting from this point cloud, I investigate the sheet shape by approximating its surface using meshing.

Figure 5.16 Representation of the mesh of *PHerc.1103*. The figure displays a schematic representation of the mesh (the triangular density is less than in the real mesh).

Several open-source software tools allow you to manipulate point clouds and convert them into 3D triangular meshes such as MeshLab [25].
Surface reconstruction from point sets in MeshLab is a sequential process with the following steps:

- Clean the point cloud by removing any outliers and irrelevant data. It also reduces the number of points to be processed.
- Compute vertex normals and orientations. We have used default meshlab parameters for computing the normals.
- Apply Poisson Reconstruction to surface reconstruction. To obtain good results, you have to experiment with different octree depth values.
- Add intensity values to all 3D points.

For more details on the algorithms for normal estimation and surface reconstruction, see Section 4.1.2.

Figure 5.16 displays a schematic representation: the mesh density is reduced for better visualization.

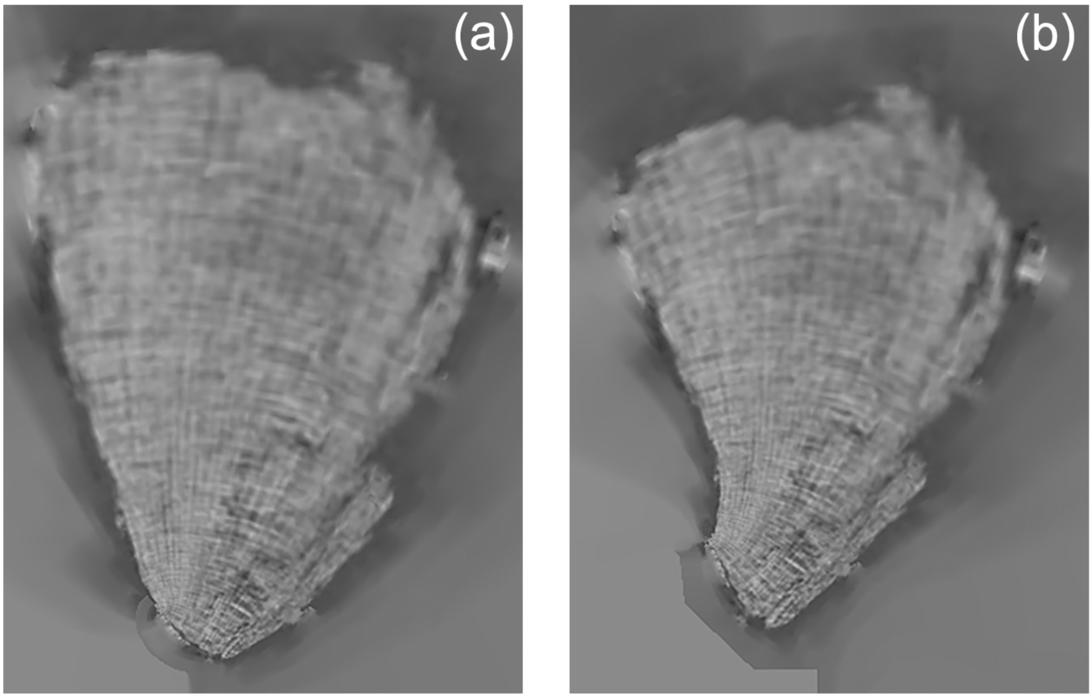

Figure 5.17 Automatic parameterization of *PHerc.1103*: (a) using and LSCM (b) using ABF.

5.5.3 Mesh parameterization

In this section we examine the 2D representations obtained from the application of the mesh parameterization methods from Section 4.1.3, i.e., Least Squares Conformal Maps (LSCM) and Angle-Based Flattening (ABF).
We then used another open-source software, Blender [Blender Online Community], to compute the LSCM and ABF parameterizations as well as the metric distortion presented in Section 4.1.3.

In the first instance, we apply the automatic mesh parameterization. Figure 5.17 and Figure 5.18 show the results of automatic parameterization of *PHerc.1103* and *PHerc.110*, respectively. In particular, the panels (a) show parameterization results using the LSCM method and the panels (b) using the ABF.

In terms of intuitive interpretation, it is clear that applying automatic mesh parameterization, the resulting map not be cohesive and thus still be counterintuitive to interpret.

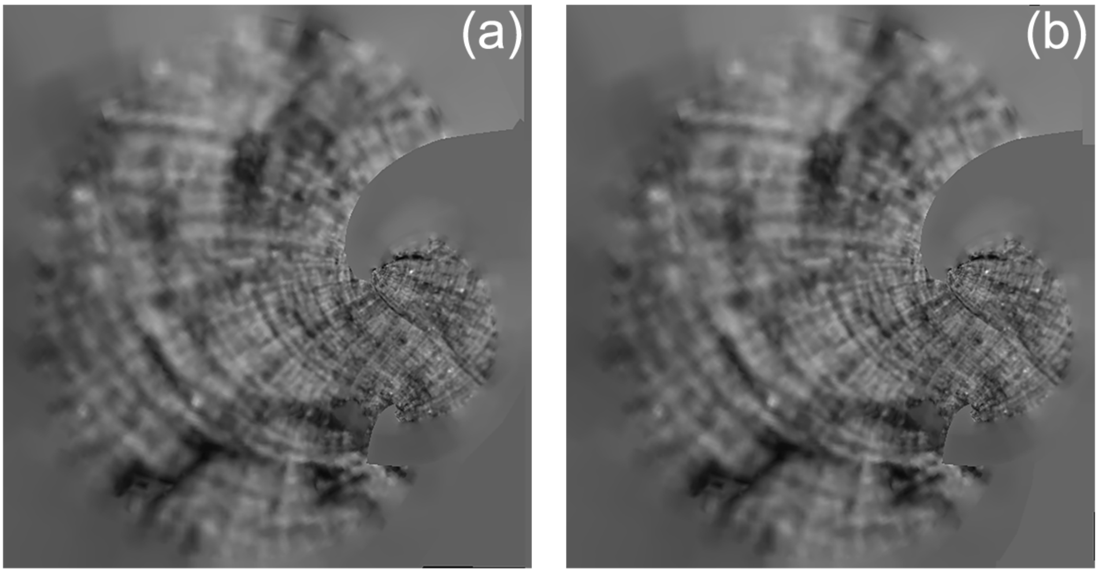

Figure 5.18 Automatic parameterization of *PHerc.110*: (a) using and LSCM (b) using ABF.

Seam cutting

As noted in Figure 5.17 and Figure 5.18, greater surface complexity usually increases parameterization distortion, independent of the parameterization technique used. To achieve acceptable distortion, the surface must be cut before parameterization to reduce the complexity of surface shape. We generated such cuts manually using a network of edges.
We use automatic parameterization results to facilitate the cutting process. We first parameterize the surface using one of the parameterization methods. We then find the point of maximal parametric distortion on the mapping and generate the shortest cut from the surface boundary to that point. We repeat the process until the distortion falls below an acceptable level. Figure 5.19 show an example of the seams (red lines) used for cutting *PHerc.1103* (a) and *PHerc.110* (b).
One problem this method face is the appearance of visible discontinuities along with the cuts created to facilitate the parameterization. Since cuts introduce discontinuities into the parameterization, a balance between the conflicting goals of small distortion and short cuts has to be achieved.

Measuring distortion

To provide a quantitative measurement of the performance of the 2D mapping produced and visualized in the figure, we computed the stretch and angular distortion metrics.

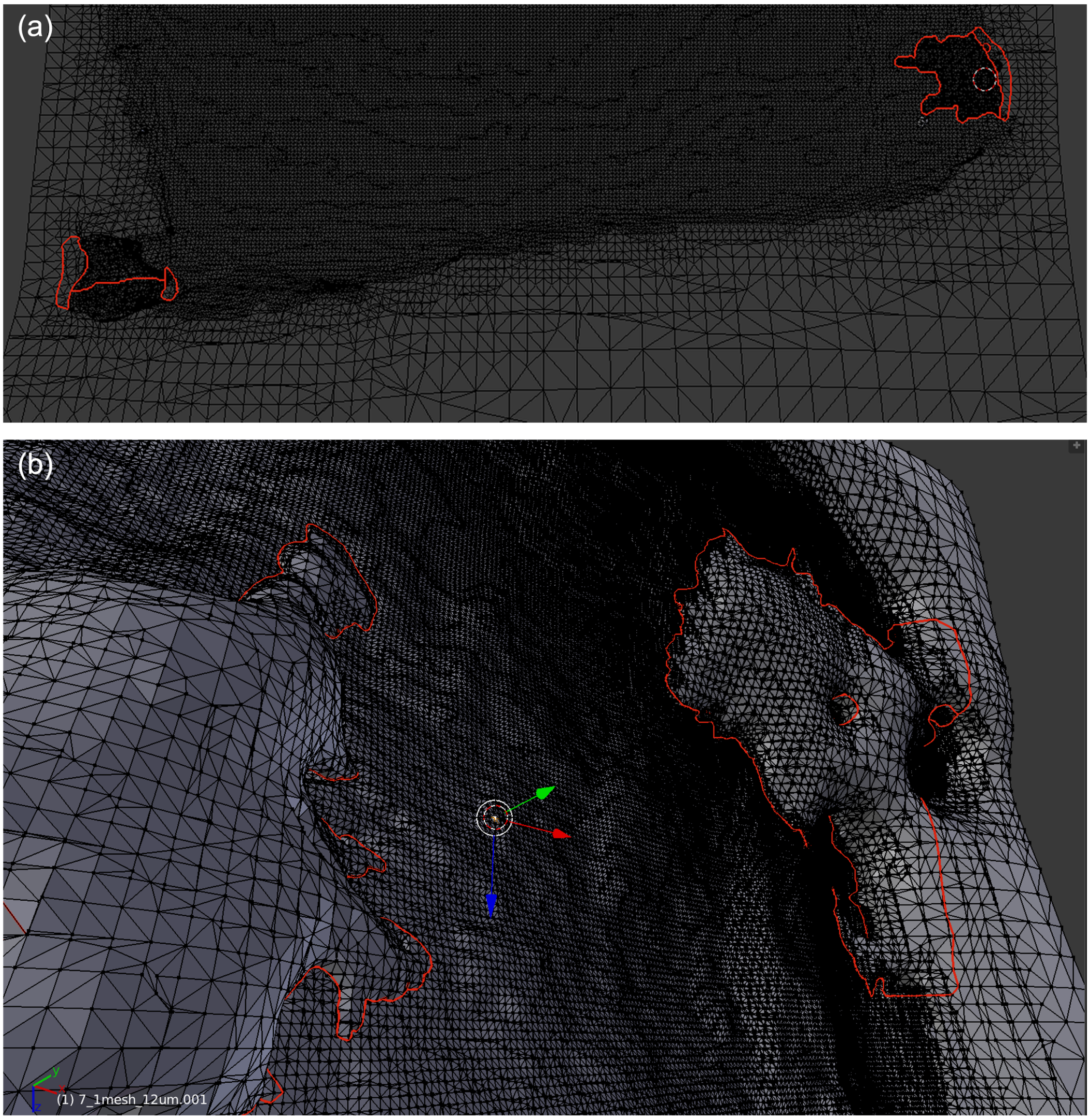

Figure 5.19 An example of the seams used for cutting *PHerc.1103* (a) and *PHerc.110* (b).

As we saw in Section 4.1.3, there are essentially only two quantities to consider minimizing in a mapping: angle distortion and area distortion.

Figure 5.20 and Figure 5.21 visualize the distribution pattern for the angular error across the parameterized surface using (a) LSCM and (b) ABF. In particular, blue means undistorted and red means fully distorted. Both mesh parameterization methods produce a mapping that minimize conformal error, i.e., angular distortion. So the result shown in Figure 5.20 and Figure 5.21 for *PHerc.1103* and *PHerc.110*, respectively, is not surprising.

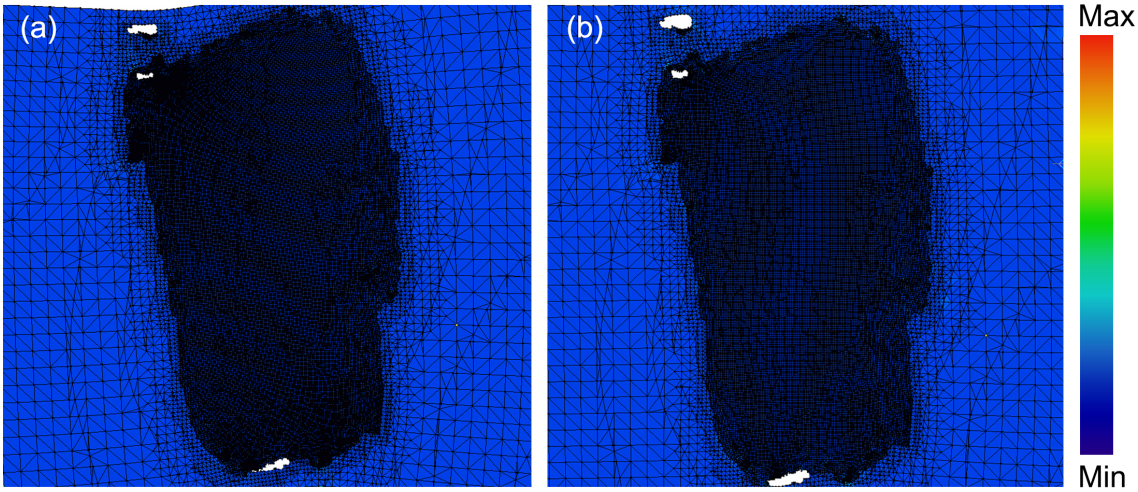

Figure 5.20 Distribution of Angular Error for *PHerc.1103*: (a) LSCM, (b) ABF.

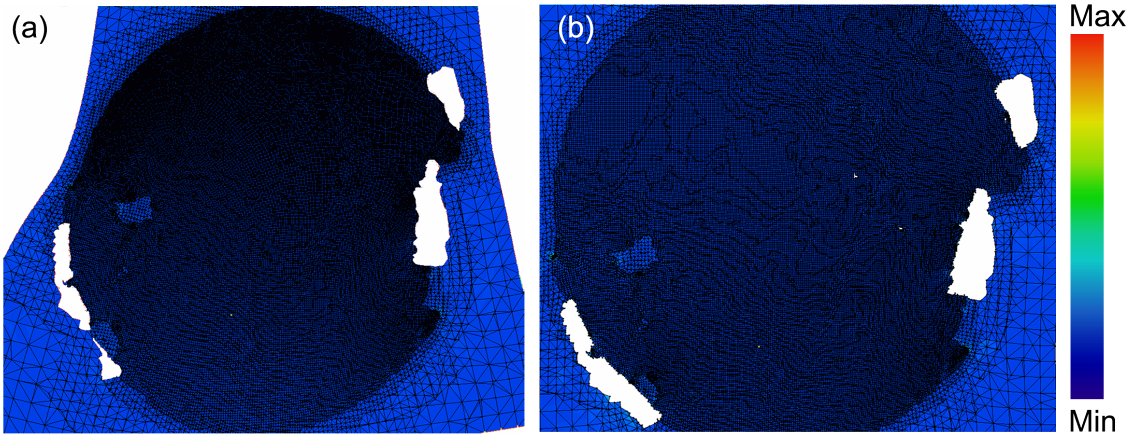

Figure 5.21 Distribution of Angular Error for *PHerc.110*: (a) LSCM, (b) ABF.

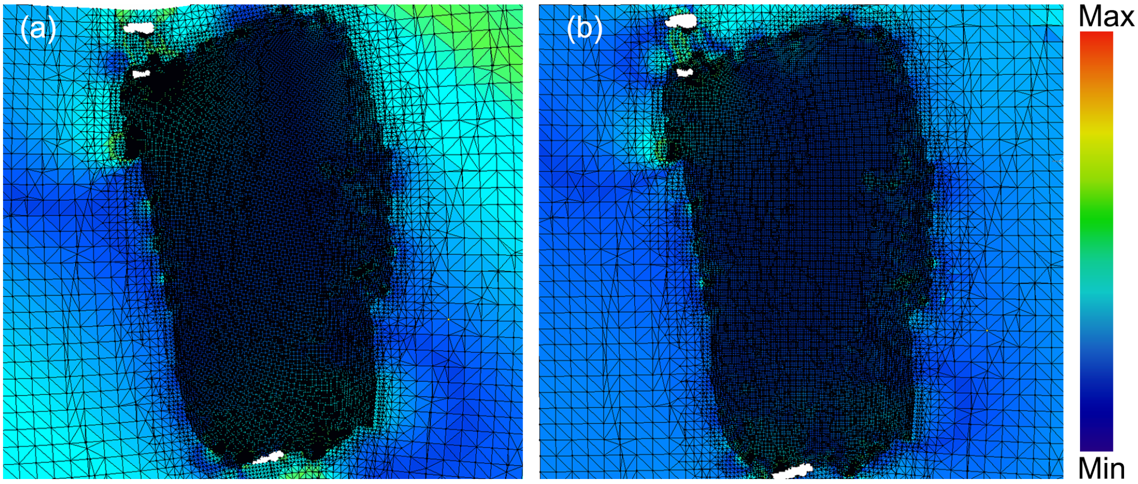

Figure 5.22 Distribution of Area Error for *PHerc.1103*: (a) LSCM, (b) ABF.

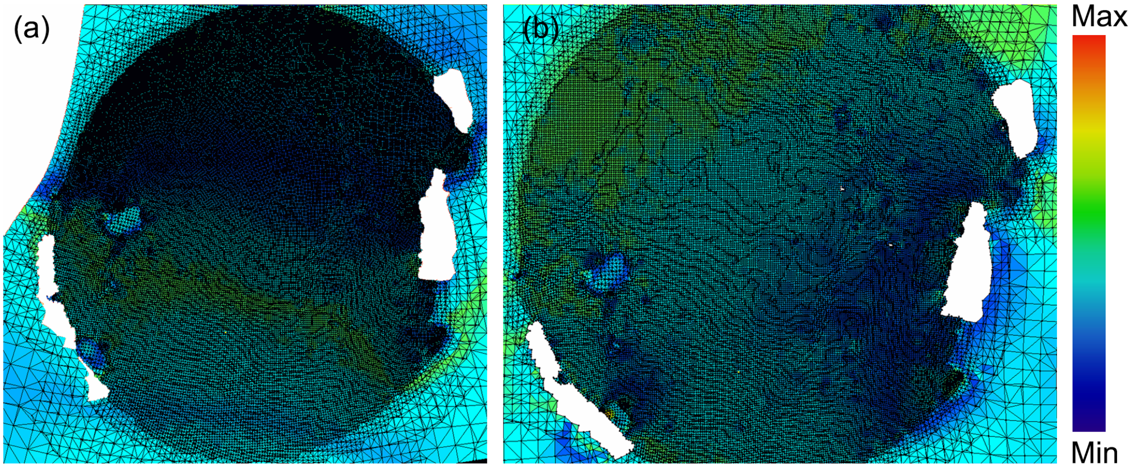

Figure 5.23 Distribution of Area Error for *PHerc.110*: (a) LSCM, (b) ABF.

The error and resulting visual distortion are represented by the isometric error metrics, as evidenced by visual inspection of Figure 5.22 and Figure 5.23 for *PHerc.1103* and *PHerc.110*, respectively. In both images, blue means undistorted and red means fully distorted.
In Figure 5.22 area distrortion is present at the edges of the parametrization. LSCM parameterization performed similary to ABF for *PHerc.1103*. On the contrary, for *PHerc.110*, LSCM parameterization performed much worse area distortion to ABF (see Figure 5.23). This resulted in very noticeable feature in the images.

2D flattened texture images

Finally, we used the resulting parameterizations to generate flattened texture images. Figure 5.24 and Figure 5.25 shown 2D texture images using the LSCM method (panels (a)) and the ABF method (panels (b)) for *PHerc.1103* and *PHerc.110*, respectively.

Figure 5.26 shows a magnification of the best previous results for *PHerc.1103* (panel (a)) and *PHerc.110* (panel (b)). The segmented sheets display a crisscrossed fibers' structure. This means that single sheets from both *PHerc.1103* and *PHerc.110* were segmented and flattened. Fibers, placed at a right angle relative to each other, as highlights Figure 5.26, are used as a guideline for single papyrus sheet identification. Therefore, we can state that our procedure of flattening is correct.

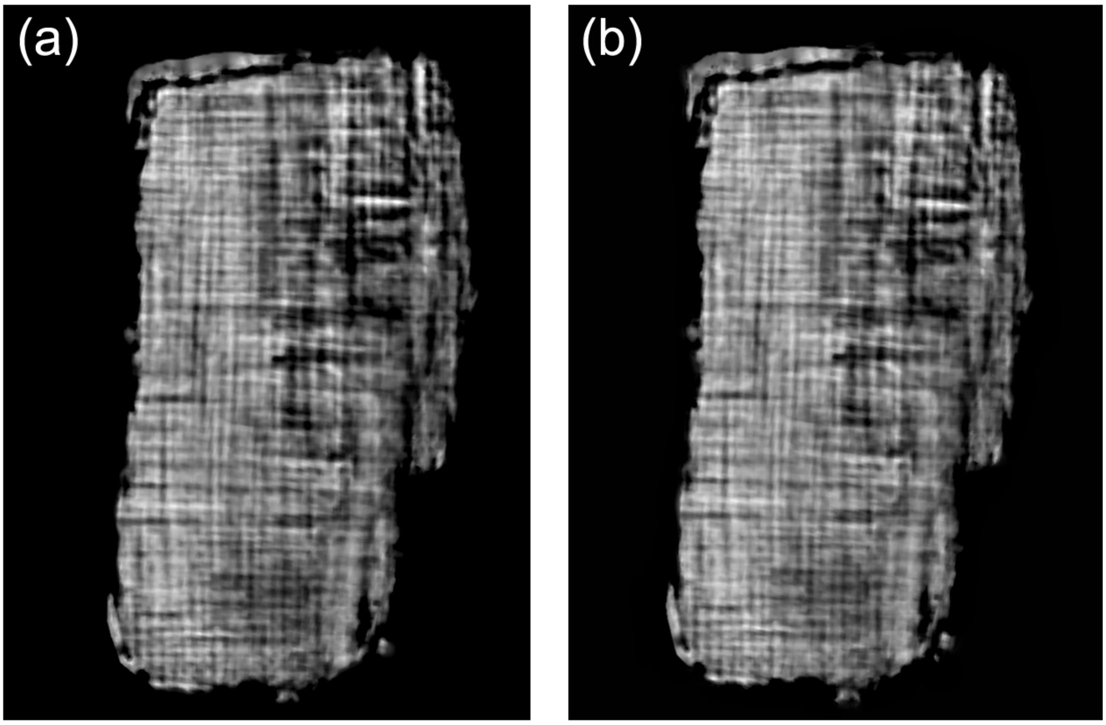

Figure 5.24 2D texture mapping using LSCM (a) and using ABF (b) for *PHerc.1103*.

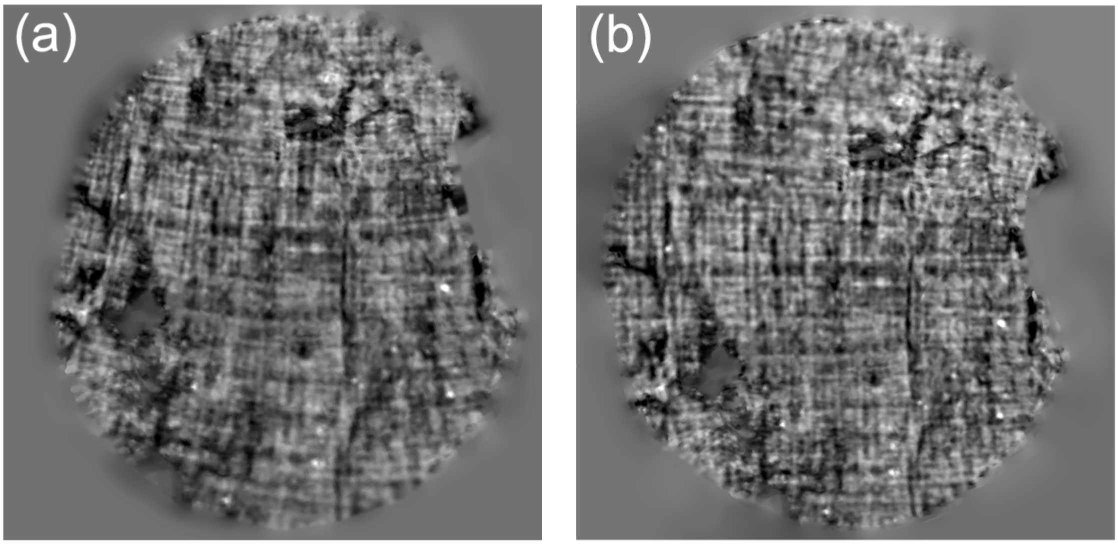

Figure 5.25 2D texture mapping using LSCM (a) and using ABF (b) for *PHerc.110*.

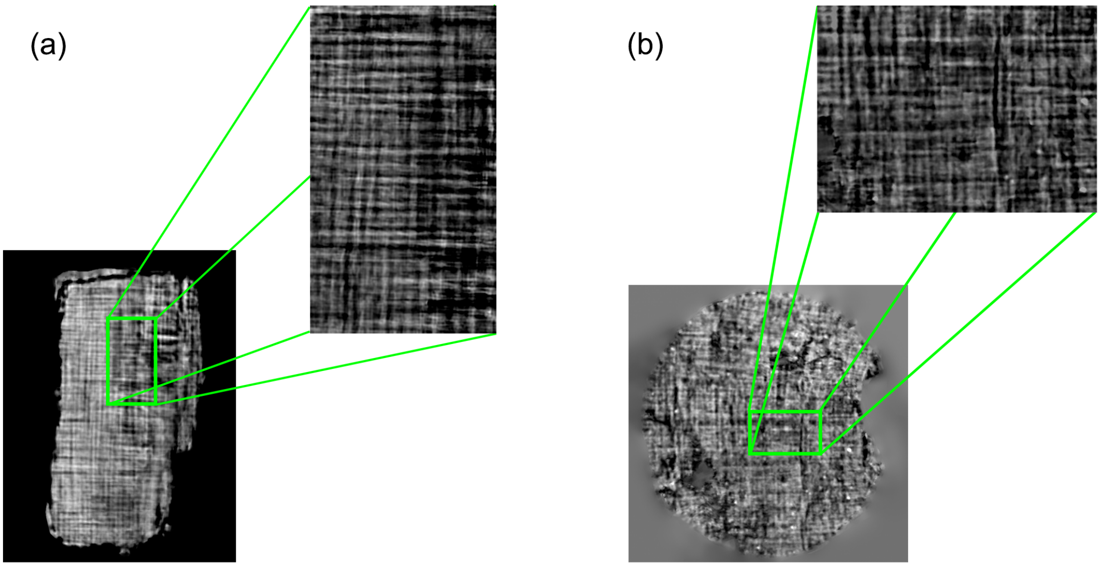

Figure 5.26 The crisscrossed fiber structure of the sheets of *PHerc.1103* (panel (a)) and *PHerc.110* (panel (b)).

Chapter 6

Conclusions

The papyrus-rolls, recovered from the Villa of the Papyri in Herculaneum, consist of two kinds: a small but unique collection of Latin papyri, and a much larger but equally unique Greek library, including works of the Epicurean Philodemus. The recovery of this library caused enormous excitement, which was replaced by terrible disappointment once it became clear that these were illegible or legible only with the greatest difficulty and only in part due to the damaged conditions.

Modern conservation principles impose to preserve the integrity of historical documents, and any attempt to open them must be avoided if there is a risk of losing the information they contain, also at the cost of leaving them untouched for an indefinite period.

In this scenario, X-ray imaging techniques represent a powerful non-destructive investigation method, capable of displaying in a three-dimensional way the volume and the internal structure of the papyri, also thanks to modern 3D rendering techniques.

In this work, in particular, two different X-ray imaging techniques are used: X-ray-micro-computed tomography (μX-CT) and X-ray Phase Contrast Tomography (XPCT). In μX-CT, the image formation is based on the partial absorption of the radiation. Since we supposed to have the C-based ink on Herculaneum carbonized papyri, the use of μX-CT is limited because the linear attenuation coefficient of the sample is nearly uniform, hence the image shows insufficient absorption contrast. To overcome this limit, we used XPCT that can measure the X-ray phase shift due to the interaction with the sample and can hence lead to a deeper understanding of the analyzed sample.

Although XPCT provides better results, both techniques have produced good results: structure and fibers of the papyrus sheet are visible in both fragments *PHerc.110* (scanned via μX-CT) and in *PHerc.1103* and *PHerc.1105* (scanned via XPCT). In the future, the optimization parameters, including high detector resolution, could improve image quality.

Before dealing with the virtual unfolding of papyri, I made a series of analysis: i) to identify the best method for phase retrieval for XPCT and ii) to understand what was the X-ray beam energy to achieve a suitable contrast and to differentiate the materials.
For the first point, I have evaluated three different algorithms, that I implemented in Python: the modified Bronnikov method, the phase-attenuation duality, and the Paganin algorithm. The phase-attenuation duality algorithm produced a reconstructed image were the smallest structures are not reconstructed. While, the modified Bronnikov method and the Paganin method both give good results, but for this thesis, Paganin's algorithm is chosen.
For the second point, I have evaluated three different energy beam. I have found that with increasing energy, the contrast in the image increases, and therefore the fibers of the papyrus can be better identified.
Once I have chosen the right parameters and the most appropriate phase retrieval algorithm, I have reconstructed the entire papyrus fragments. However, I found ring artifacts that disturbed the image quality. An ImageJ macro was written to delete these artifacts. The artifact removal process allowed the visualization of clean slices and helped to reveal traces compatible with writing in *PHerc.1105*. This important result demonstrates the potential of the XPCT technique in reading the carbonized Herculaneum papyri.

We then moved to the heart of this thesis: the virtual unfolding of Herculaneum papyri. We have proposed a computational platform for the virtual unfolding procedure, and I have shown the relative results of its application on two Herculaneum papyrus fragments. The pipeline involves the following steps: surface segmentation, meshing and reconstructing surface and mesh parameterization (i.e., flattening).
I have considered related problems to all of these steps for fragment unfolding in more detail and I have evaluated the algorithms by applying them to two different fragment data sets, which vary in the parchment's properties, condition, size and number of layers. *PHerc.110* belonged to a scroll partially unrolled in 1867, while *PHerc.1103* is a part of scorza, which is usually the most damaged part and in some places it appears as a dense crust. These results are important because scorza could contain the very precious information relating to the author, title and length of the work and encourage further research to discover the priceless contents hidden inside.
To validate the accuracy of our flattening pipeline, I took advantage of the high contrast of the fibrous structure image that can be used as a guideline for single papyrus layer identification. The identification of the papyrus sheet surface is a crucial point for the tracing of the writing. The scroll sheet has a crisscross pattern due to how the papyrus sheet was produced. A papyrus sheet is composed of two layers of plant strips with parallel fibers placed at the right angle relative to each other. The sheet comprises the internal layer called recto, where

commonly the text was written (writing surface), and the external layer, verso, useful for rolling the sheet (supporting layer). The crisscrossed fibers' structure found demonstrates that single sheets from both *PHerc.1103* and *PHerc.110* were segmented and flattened. Fibers, placed at a right angle relative to each other, are used as a guideline for single papyrus sheet identification. Therefore, our experiments demonstrate that our pipeline is able to successfully unfold the fragments.

The basic steps for the procedures of segmentation and flattering have been performed using free software. We provide an accessible algorithm that can be reproduced, optimize, and improved.

As future perspectives, the most important step of the entire pipeline, i.e., surface segmentation, could be made automatic. With an automatic surface segmentation, the analysis times and error caused by the user would be greatly reduced. The flattening step is another point where improvements can be made by trying and performing a comparative analysis between different mapping schemes, for example, the physics-based material modeling (MM) algorithm [64].

Bibliography

[1] Amenta, N., Bern, M., and Kamvysselis, M. (1998). A new voronoi-based surface reconstruction algorithm. In *Proceedings of the 25th Annual Conference on Computer Graphics and Interactive Techniques*, SIGGRAPH '98, pages 415–421, New York, NY, USA. ACM.

[2] Anegeli, A. (1994). *Lo svolgimento dei papiri carbonizzati.*, volume 3. PLup.

[3] Arfelli, F., Bonvicini, V., Bravin, A., Cantatore, G., Castelli, E., Palma, L., Di Michiel, M., Fabrizioli, M., Longo, R., Menk, R. H., Olivo, A., Pani, S., Pontoni, D., Poropat, P., Prest, M., Rachevski, A., Ratti, M., Rigon, L., Tromba, G., and Zanconati, F. (2000). Mammography with synchrotron radiation: Phase-detection techniques1. *Radiology*, 215:286–93.

[4] Attwood, D. and Sakdinawat, A. (2017). *X-Rays and Extreme Ultraviolet Radiation: Principles and Applications*. Cambridge University Press, 2 edition.

[5] Bajaj, C., Bernardini, F., and Xu, G. (2001). Automatic reconstruction of surfaces and scalar fields from 3d scans. *Proceedings of the ACM SIGGRAPH Conference on Computer Graphics*, 29.

[6] Baumann, R., Carr Porter, D., and Brent Seales, W. (2008). The use of micro-ct in the study of archaeological artifacts.

[7] Bech, M. (2009). *X-ray imaging with a grating interferometer*. PhD thesis, The Graduate School of Science, Faculty of Science, Niels Bohr Institute, University of Copenhagen, Denmark.

[8] Bettuzzi, M., Casali, F., Morigi, M. P., Brancaccio, R., Carson, D., Chiari, G., and Maish, J. (2015). Computed tomography of a medium size roman bronze of cupid. *Applied Physics A*, 118.

[9] Beucher, S. and Meyer, F. (1993). *The morphological approach to segmentation: The watershed transformation*, volume Vol. 34, pages 433–481.

[Blender Online Community] Blender Online Community. Blender. http://www.blender.org.

[11] Boin, M. and Haibel, A. (2006). Compensation of ring artefacts in synchrotron tomographic images. *Opt. Express*, 14(25):12071–12075.

[12] Boissonnat, J.-D. (1984). Geometric structures for three-dimensional shape representation. *ACM Trans. Graph.*, 3(4):266–286.

[13] Born, M., Wolf, E., Bhatia, A. B., Clemmow, P. C., Gabor, D., Stokes, A. R., Taylor, A. M., Wayman, P. A., and Wilcock, W. L. (1999). *Elements of the theory of diffraction*, page 412–516. Cambridge University Press, 7 edition.

[14] Bronnikov, A. V. (1999). Reconstruction formulas in phase-contrast tomography. *Optics Communications*, 171(4):239 – 244.

[15] Bukreeva, I., Mittone, A., Bravin, A., Giulia, F., Alessandrelli, M., Coan, P., Formoso, V., Agostino, R., Giocondo, M., Ciuchi, F., Fratini, M., Massimi, L., Lamarra, A., Andreani, C., Bartolino, R., Gigli, G., Ranocchia, G., and Cedola, A. (2016). Corrigendum: Virtual unrolling and deciphering of herculaneum papyri by x-ray phase-contrast tomography. *Scientific Reports*, 6:30364.

[16] Burvall, A., Lundström, U., A C Takman, P., Larsson, D., and M Hertz, H. (2011). Phase retrieval in x-ray phase-contrast imaging suitable for tomography. *Optics express*, 19:10359–76.

[17] Capasso, M. (1991). *Manuale di papirologia ercolanese*. Dipartimento di Filologia Classica e Medievale: Testi e studi. Congedo Editore.

[18] Carr, J. C., Beatson, R. K., Cherrie, J. B., Mitchell, T. J., Fright, W. R., McCallum, B. C., and Evans, T. R. (2001). Reconstruction and representation of 3d objects with radial basis functions. In *Proceedings of the 28th Annual Conference on Computer Graphics and Interactive Techniques*, SIGGRAPH '01, pages 67–76, New York, NY, USA. ACM.

[19] Cavallo, G. (1983). *Libri, scritture, scribi a Ercolano.* Macchiaroli.

[20] Cavallo, G. (1984). *I rotoli di Ercolano come prodotti scritti. Quattro riflessioni.* S & C.

[21] Cavallo, G. (2014). I papiri di ercolano come documenti per la storia delle biblioteche e dei libri antichi.

[22] Chapman, D., Thomlinson, W., Johnston, R. E., Washburn, D., Pisano, E., GmÃŒr, N., Zhong, Z., Menk, R., Arfelli, F., and Sayers, D. (1997). Diffraction enhanced x-ray imaging. *Physics in Medicine and Biology*, 42(11):2015–2025.

[23] Chenyang Xu and Prince, J. L. (1998). Snakes, shapes, and gradient vector flow. *IEEE Transactions on Image Processing*, 7(3):359–369.

[24] Cho, S., Haralick, R., and Yi, S. (1989). Improvement of kittler and illingworth's minimum error thresholding. *Pattern Recogn.*, 22(5):609–617.

[25] Cignoni, P., Callieri, M., Corsini, M., Dellepiane, M., Ganovelli, F., and Ranzuglia, G. (2008). MeshLab: an Open-Source Mesh Processing Tool. In Scarano, V., Chiara, R. D., and Erra, U., editors, *Eurographics Italian Chapter Conference*. The Eurographics Association.

[26] Cloetens, P., Pateyron-Salomé, M., Buffiere, J.-y., Peix, G., Baruchel, J., Peyrin, F., and Schlenker, M. (1997). Observation of microstructure and damage in materials by phase sensitive radiography and tomography. *Journal of Applied Physics*, 81:5878–5886.

[27] Comparetti, D. and De Petra, G. (1883). *La villa ercolanese dei Pisoni*. La villa ercolanese dei Pisoni. E. Loescher.

[28] Cooley, J. W. and Tukey, J. W. (1965). An Algorithm for the Machine Calculation of Complex Fourier Series. *Math. Comput.*, 19:297–301.

[29] David, C., Nöihammer, B., Solak, H. H., and Ziegler, E. (2002). Differential x-ray phase contrast imaging using a shearing interferometer. *Applied Physics Letters*, 81(17):3287–3289.

[30] Davis, T. J. (1996). X-ray diffraction imaging using perfect crystals. *Journal of X-Ray Science and Technology*, 6:317–342.

[31] Edelsbrunner, H. and Mücke, E. P. (1994). Three-dimensional alpha shapes. *ACM Trans. Graph.*, 13(1):43–72.

[32] Feldkamp, L. A., Davis, L. C., and Kress, J. W. (1984). Practical cone-beam algorithm. *J. Opt. Soc. Am. A*, 1(6):612–619.

[33] Floater, M. S. and Hormann, K. (2005). Surface parameterization: a tutorial and survey. In *Advances in Multiresolution for Geometric Modelling*.

[34] F.R.S., H. T. E. (1836). Lxxvi. facts relating to optical science. no. iv. *The London, Edinburgh, and Dublin Philosophical Magazine and Journal of Science*, 9(56):401–407.

[35] Förster, E., Goetz, K., and Zaumseil, P. (1980). Double crystal diffractometry for the characterization of targets for laser fusion experiments. *Kristall und Technik*, 15(8):937–945.

[36] Gigante, M. (1979). *Catalogo dei papiri ercolanesi*. Bibliopolis.

[37] Groso, A., Abela, R., and Stampanoni, M. (2006). Implementation of a fast method for high resolution phase contrast tomography. *Opt. Express*, 14(18):8103–8110.

[38] Guo, R. and Pandit, S. M. (1998). Automatic threshold selection based on histogram modes and a discriminant criterion. *Machine Vision and Applications*, 10:331–338.

[39] Gureyev, T. E., Roberts, A., and Nugent, K. A. (1995). Phase retrieval with the transport-of-intensity equation: matrix solution with use of zernike polynomials. *J. Opt. Soc. Am. A*, 12(9):1932–1941.

[40] Gursoy, D., Carlo, F., Xiao, X., and Jacobsen, C. (2014). Tomopy: A framework for the analysis of synchrotron tomographic data. *Journal of Synchrotron Radiation*, 21.

[41] Hoppe, H., DeRose, T., Duchamp, T., McDonald, J., and Stuetzle, W. (1992). Surface reconstruction from unorganized points. *SIGGRAPH Comput. Graph.*, 26(2):71–78.

[42] Hormann, K., Levy, B., and Sheffer, A. (2008). Mesh parameterization: Theory and practice. *ACM SIGGRAPH 2007 Papers - International Conference on Computer Graphics and Interactive Techniques*, 2.

[43] Ingal, V. N. and Beliaevskaya, E. A. (1995). X-ray plane-wave topography observation of the phase contrast from a non-crystalline object. *Journal of Physics D Applied Physics*, 28:2314–2317.

[44] Kak, A. and Slaney, M. (2001). *Principles of Computerized Tomographic Imaging*. Society for Industrial and Applied Mathematics.

[45] Kazhdan, M., Bolitho, M., and Hoppe, H. (2006). Poisson surface reconstruction. In *Proceedings of the Fourth Eurographics Symposium on Geometry Processing*, SGP '06, pages 61–70, Aire-la-Ville, Switzerland, Switzerland. Eurographics Association.

[46] Kazhdan, M. and Hoppe, H. (2013). Screened poisson surface reconstruction. *ACM Transactions on Graphics (TOG)*, 32(3):29.

[47] Kolluri, R., Shewchuk, J. R., and O'Brien, J. F. (2004). Spectral surface reconstruction from noisy point clouds. In *Proceedings of the 2004 Eurographics/ACM SIGGRAPH Symposium on Geometry Processing*, SGP '04, pages 11–21, New York, NY, USA. ACM.

[48] LANDAU, L. and LIFSHITZ, E. (1984). Chapter ix - the electromagnetic wave equations. In LANDAU, L. and LIFSHITZ, E., editors, *Electrodynamics of Continuous Media (Second Edition)*, volume 8 of *Course of Theoretical Physics*, pages 257 – 289. Pergamon, Amsterdam, second edition edition.

[49] Leach, B. and Tait, J. (2000). Papyrus. In Nicholson, P. T. and Shaw, I., editors, *Ancient Egyptian materials and technology*, pages 227–253. Cambridge University Press, Cambridge.

[50] Lévy, B., Petitjean, S., Ray, N., and Maillot, J. (2002). Least squares conformal maps for automatic texture atlas generation. *ACM Trans. Graph.*, 21(3):362–371.

[51] Li, C. H. and Tam, P. K. S. (1998). An iterative algorithm for minimum cross entropy thresholding. *Pattern Recogn. Lett.*, 19(8):771–776.

[52] Liu, C., Rosin, P. L., Lai, Y.-K., and Hu, W. (2018). Robust virtual unrolling of historical parchment xmt images. *IEEE Transactions on Image Processing*, 27:1914–1926.

[53] Mills, D., Davis, G., Lai, Y.-K., and Rosin, P. (2014). Apocalypto - revealing lost text with xmt. *Proceedings of SPIE - The International Society for Optical Engineering*, 9212.

[54] Mocella, V., Brun, E., Ferrero, C., and Delattre, D. (2015). Revealing letters in rolled herculaneum papyri by x-ray phase-contrast imaging. *Nature communications*, 6:5895.

[55] Momose, A., Kawamoto, S., Koyama, I., Hamaishi, Y., Takai, K., and Suzuki, Y. (2003). Demonstration of x-ray talbot interferometry. *Japanese Journal of Applied Physics*, 42(Part 2, No. 7B):L866–L868.

[56] Morigi, M. P., Casali, F., Bettuzzi, M., Bianconi, D., Brancaccio, R., Cornacchia, S., Pasini, A., Rossi, A., Aldrovandi, A., and Cauzzi, D. (2013). Ct investigation of two paintings on wood tables by gentile da fabriano. *Nuclear Instruments and Methods in Physics Research Section A Accelerators Spectrometers Detectors and Associated Equipment*, 580:735–738.

[57] Morigi, M. P., Casali, F., Bettuzzi, M., Brancaccio, R., and D'Errico, V. (2010). Application of x-ray computed tomography to cultural heritage diagnostics. *Applied Physics A*, 100:653–661.

[58] Münch, B., Trtik, P., Marone, F., and Stampanoni, M. (2009). Stripe and ring artifact removal with combined wavelet — fourier filtering. *Opt. Express*, 17(10):8567–8591.

[59] Muraki, S. (1991). Volumetric shape description of range data using “blobby model”. *SIGGRAPH Comput. Graph.*, 25(4):227–235.

[60] Olivo, J. (1994). Automatic threshold selection using the wavelet transform. *CVGIP: Graphical Models and Image Processing*, 56(3):205 – 218.

[61] Otsu, N. (1979). A threshold selection method from gray-level histograms. *IEEE Transactions on Systems, Man, and Cybernetics*, 9(1):62–66.

[62] Paganin, D. (2006). *Coherent x-ray optics*. Oxford University Press.

[63] Paganin, D., Mayo, S. C., Gureyev, T. E., Miller, P. R., and Wilkins, S. W. (2002). Simultaneous phase and amplitude extraction from a single defocused image of a homogeneous object. *Journal of Microscopy*, 206(1):33–40.

[64] Parker, C. S., Seales, W. B., and Shor, P. (2016). Quantitative distortion analysis of flattening applied to the scroll from en-gedi. In *Art & Archaeology, 2nd International Conference*.

[65] Pfeiffer, F., Weitkamp, T., Bunk, O., and David, C. (2006). Phase retrieval and differential phase-contrast imaging with low-brilliance x-ray sources. *Nature Physics*, 2(4):258–261.

[66] Piaggio, A. (1769-1771). *Memorie*.

[67] Pogany, A., Gao, D., and Wilkins, S. W. (1997). Contrast and resolution in imaging with a microfocus x-ray source. *Review of Scientific Instruments*, 68(7):2774–2782.

[68] Pun, T. (1980). A new method for grey-level picture thresholding using the entropy of the histogram. *Signal Processing*, 2:223–237.

[69] Ramesh, N., Yoo, J., and Sethi, I. (1995). Thresholding based on histogram approximation. *Vision, Image and Signal Processing, IEE Proceedings -*, 142:271 – 279.

[70] Raven, C. (1998). Numerical removal of ring artifacts in microtomography. *Review of Scientific Instruments*, 69(8):2978–2980.

[71] Re, A., Albertin, F., Avataneo, C., Brancaccio, R., Corsi, J., Cotto, G., De Blasi, S., Dughera, G., Durisi, E., Ferrarese, W., Giovagnoli, A., Grassi, N., Lo Giudice, A., Mereu, P., Mila, G., Nervo, M., Pastrone, N., Prino, F., Ramello, L., Ravera, M., Ricci, C., Romero, A., Sacchi, R., Staiano, A., Visca, L., and Zamprotta, L. (2014). X-ray tomography of large wooden artworks: the case study of "doppio corpo" by pietro piffetti. *Heritage Science*, 2(1):19.

[72] Roentgen, W. C. (1898). Ueber eine neue art von strahlen. *Annalen der Physik*, 300(1):12–17.

[73] Rosenfeld, A. and De La Torre, P. (1983). Histogram concavity analysis as an aid in threshold selection. *IEEE Transactions on Systems, Man, and Cybernetics*, SMC-13(2):231–235.

[74] Rosin, P., Lai, Y.-K., Liu, C., Davis, G., Mills, D., Tuson, G., and Russell, Y. (2018). Virtual recovery of content from x-ray micro-tomography scans of damaged historic scrolls. *Scientific Reports*, 8.

[75] Rueden, C. T., Schindelin, J., Hiner, M. C., DeZonia, B. E., Walter, A. E., Arena, E. T., and Eliceiri, K. W. (2017). Imagej2: Imagej for the next generation of scientific image data. *BMC Bioinformatics*, 18(1):529.

[76] Samko, O., Lai, Y.-K., Marshall, D., and Rosin, P. L. (2014). Virtual unrolling and information recovery from scanned scrolled historical documents. *Pattern Recognition*, 47(1):248 – 259.

[77] Sbordone, F. (1971). *Recenti tentativi di svolgimento dei papiri ercolanesi.*, volume 1. CErc.

[78] Seales, W. B. and Delattre, D. (2013). Virtual unrolling of carbonized herculaneum scrolls: Research status (2007–2012). *Cronache Ercolanesi*, 43:191–208.

[79] Seales, W. B., Parker, C. S., Segal, M., Tov, E., Shor, P., and Porath, Y. (2016). From damage to discovery via virtual unwrapping: Reading the scroll from en-gedi. *Science Advances*, 2(9).

[80] Sezan, M. I. (1990). A peak detection algorithm and its application to histogram-based image data reduction. *Computer Vision, Graphics, and Image Processing*, 49(1):36 – 51.

[81] Sezgin, M. and Sankur, B. (2004). Survey over image thresholding techniques and quantitative performance evaluation. *J. Electronic Imaging*, 13:146–168.

[82] Sheffer, A. and de Sturler, E. (2001). Parameterization of faceted surfaces for meshing using angle-based flattening. *Engineering with Computers*, 17(3):326–337.

[83] Snigirev, A., Snigireva, I., Kohn, V., Kuznetsov, S., and Igor, S. (1996). On the possibilities of x-ray phase contrast microimaging by coherent high-energy synchrotron radiation. *Review of Scientific Instruments*, 66:5486 – 5492.

[84] Teague, M. R. (1982). Irradiance moments: their propagation and use for unique retrieval of phase. *J. Opt. Soc. Am.*, 72(9):1199–1209.

[85] Teague, M. R. (1983). Deterministic phase retrieval: a green's function solution. *J. Opt. Soc. Am.*, 73(11):1434–1441.

[86] Turk, G. and O'Brien, J. F. (2002). Modelling with implicit surfaces that interpolate. *ACM Trans. Graph.*, 21(4):855–873.

[87] Vo, N. T., Drakopoulos, M., Atwood, R. C., and Reinhard, C. (2014). Reliable method for calculating the center of rotation in parallel-beam tomography. *Opt. Express*, 22(16):19078–19086.

[88] Weitkamp, T., Diaz, A., David, C., Pfeiffer, F., Stampanoni, M., Cloetens, P., and Ziegler, E. (2005). X-ray phase imaging with a grating interferometer. *Opt. Express*, 13(16):6296–6304.

[89] Wu, X. and Liu, H. (2005). X-ray cone-beam phase tomography formulas based on phase-attenuation duality. *Opt. Express*, 13(16):6000–6014.

[90] Wu, X., Liu, H., and Yan, A. (2005). X-ray phase-attenuation duality and phase retrieval. *Opt. Lett.*, 30(4):379–381.

[91] Y. Boykov, Y. and Jolly, M.-p. (2001). Interactive graph cuts for optimal boundary & region segmentation of objects in n-d images. *Proceedings. Eighth IEEE International Conference on Computer Vision: 2001. Vol.1*, 1:105–112.

[92] Yale University Library Special Collections Conservator Unit, P. D. (2012). *Medieval Manuscripts, Some Ink and Pigment Recipes*. Yale University.

[93] Yezzi, A. J., Kichenassamy, S., Kumar, A., Olver, P. J., and Tannenbaum, A. R. (1997). A geometric snake model for segmentation of medical imagery. *IEEE Transactions on Medical Imaging*, 16:199–209.

[94] Yu, X. and Yla-Jaaski, J. (1991). A new algorithm for image segmentation based on region growing and edge detection. In *1991., IEEE International Sympoisum on Circuits and Systems*, volume 1, pages 516–519.

[95] Zanella, E., Gurioli, L., Pareschi, M. T., and Lanza, R. (2007). Influences of urban fabric on pyroclastic density currents at pompeii (italy): 2. temperature of the deposits and hazard implications. *Journal of Geophysical Research: Solid Earth*, 112(B5).

[96] Zienkiewicz, O. C. (1985). Computational galerkin methods, c. a. j. fletcher, springer verlag, n. y./berlin/heidelberg, 1984 (309 pages $32.90 or dm. 88). *International Journal for Numerical Methods in Engineering*, 21(2):385–385.

Appendix A

Complex Index of Refraction

To study the refractive index of a material, our point of departure is the vector wave equation, follows directly from Maxwell's equations:

$$\left(\frac{\partial^2}{\partial t^2} - c^2\nabla^2\right)\mathbf{E}(\mathbf{r},t) = -\frac{1}{\varepsilon_0}\left[\frac{\partial \mathbf{J}(\mathbf{r},t)}{\partial t} + c^2\nabla\rho(\mathbf{r},t)\right] \tag{A.1}$$

where $\mathbf{E}(\mathbf{r},t)$ is the electric field vector, $\mathbf{J}(\mathbf{r},t)$ is the current density, ρ is the charge density and $c = 1/\sqrt{\mu_0\varepsilon_0}$ is the phase velocity of a electromagnetic wave propagating in a vacuum, with ε_0 the permittivity (dielectric constant) of free space, and μ_0 the magnetic permeability. Eq. (A.1) describe the propagation of electromagnetic waves, it covers electromagnetic phenomena extending from very long wavelengths to radio waves, microwaves, infrared, visible, ultraviolet, X-rays, and beyond.

Considering the propagation of transverse waves, in which the field $\mathbf{E}(\mathbf{r},t)$ is orthogonal to vector $\mathbf{k}$, $\nabla\rho$ and the longitudinal component of $\mathbf{J}(\mathbf{r},t)$ do not contribute. Thus for transverse electromagnetic waves, eq. (A.1) becomes:

$$\left(\frac{\partial^2}{\partial t^2} - c^2\nabla^2\right)\mathbf{E}_T(\mathbf{r},t) = -\frac{1}{\varepsilon_0}\frac{\partial \mathbf{J}_T(\mathbf{r},t)}{\partial t} \tag{A.2}$$

where the subscript T denotes a transverse direction to $\mathbf{k}$ but that we will no longer report in our discussion.

To calculate the current density $\mathbf{J}(\mathbf{r},t)$, we take into account a microscopic model. We consider the Lorentz model, according to which the electron is bound to the massive positively charged nucleus of the atom by a force that behaves according to Hooke's Law.
An applied electromagnetic wave of frequency ω would then interact with the charge of the electron, causing an oscillatory electron motion of the same frequency. The equation of

motion can then be written as follows:

$$\frac{d^2\mathbf{x}}{dt^2} - \gamma\frac{d\mathbf{x}}{dt} + \omega_s^2\mathbf{x} = \frac{-e}{m}(\mathbf{E} + \mathbf{v}\times\mathbf{B}) \tag{A.3}$$

where e, m and ω_s are the charge, mass and resonance frequency of the elecrtons, respectively. On the left-hand side of eq. (A.3), the first term is the acceleration, the second term is a dissipative force and the third term is the spring force, while on the right-hand side we have the Lorentz force, where $(\mathbf{v}\times\mathbf{B}) \simeq 0$ for non-relativistic oscillation velocities $\mathbf{v}$ and $\mathbf{B}(\mathbf{r},t)$ is the magnetic field.
The solution of the eq. (A.3) is:

$$\mathbf{x}(\mathbf{r},t) = \frac{e}{m}\frac{\mathbf{E}(\mathbf{r},t)}{(\omega^2 - \omega_s^2) + i\gamma\omega} \tag{A.4}$$

and for small amplitude oscillations, the oscillation velocity is:

$$\mathbf{v}(\mathbf{r},t) = \frac{e}{m}\frac{1}{(\omega^2 - \omega_s^2) + i\gamma\omega}\frac{\partial\mathbf{E}(\mathbf{r},t)}{\partial t} \tag{A.5}$$

The contribution to the current density must consider the contribution of every single electron of every single atom. It is possible to write the electron distribution function within the atom and so the current density such as:

$$n_e(\mathbf{r},t) = \sum_{s=1}^{Z}\delta[\mathbf{r} - \Delta\mathbf{r}_s(t)] \tag{A.6}$$

$$\mathbf{J}(\mathbf{r},t) = -e\sum_{s=1}^{Z}\delta[\mathbf{r} - \Delta\mathbf{r}_s(t)]\mathbf{v}_s(t) \tag{A.7}$$

where $\mathbf{r}$ represents the coordinate of the nucleus and $\Delta\mathbf{r}$ the displacement vector from the nucleus, and Z is the total number of electrons of the atom.

Considering the scattered radiation in the forward direction, the electron positions are irrelevant and, therefore, eq. (A.7) can be rewrite as:

$$\begin{aligned}\mathbf{J}(\mathbf{r},t) &= -en_a\sum_s g_s\mathbf{v}_s(\mathbf{r},t)\\ &= -\frac{en_a}{m}\sum_s\frac{g_s}{(\omega^2 - \omega_s^2) + i\gamma\omega}\frac{\partial\mathbf{E}(\mathbf{r},t)}{\partial t}\end{aligned} \tag{A.8}$$

the last equality follows from the eq. (A.5).
In eq. (A.8), n_a is the number density (atoms or electrons per unit volume) and g_s are

the oscillator strengths, such that the sum of the oscillator strengths equals the number of electrons Z:

$$\sum_s g_s = Z \tag{A.9}$$

Substututing eq. (A.8) into eq. (A.2), it follows that:

$$\left(\frac{\partial^2}{\partial t^2} - c^2\nabla^2\right)\mathbf{E}(\mathbf{r},t) = \frac{e^2 n_a}{\varepsilon_0 m}\sum_s \frac{g_s}{(\omega^2-\omega_s^2)+i\gamma\omega}\frac{\partial^2\mathbf{E}(\mathbf{r},t)}{\partial t^2} \tag{A.10}$$

Combining terms with similar differential operators:

$$\left[\left(1-\frac{e^2 n_a}{\varepsilon_0 m}\sum_s \frac{g_s}{(\omega^2-\omega_s^2)+i\gamma\omega}\right)\frac{\partial^2}{\partial t^2} - c^2\nabla^2\right]\mathbf{E}(\mathbf{r},t) = 0 \tag{A.11}$$

which can be rewritten in the standard form of the wave equation as:

$$\left(\frac{n^2}{c^2}\frac{\partial^2}{\partial t^2} - \nabla^2\right)\mathbf{E}(\mathbf{r},t) = 0 \tag{A.12}$$

where the refractive index $n(\omega)$ is defined as:

$$n(\omega) = \left[1-\frac{e^2 n_a}{\varepsilon_0 m}\sum_s \frac{g_s}{(\omega^2-\omega_s^2)+i\gamma\omega}\right]^{1/2} \tag{A.13}$$

Note that the refractive index is in general a complex quantity and it has a strong frequency dependence, particularly near the resonant frequencies ω_s.

Now we consider the specific case of X-ray radiation, for which $\omega^2 \gg \frac{e^2 n_a}{\varepsilon_0 m}$, so the eq. (A.13) can be written as:

$$n(\omega) = 1-\frac{e^2 n_a}{2\varepsilon_0 m}\sum_s \frac{g_s}{(\omega^2-\omega_s^2)+i\gamma\omega} \tag{A.14}$$

Eq. (A.14) can be rewritten in somewhat simpler form in term of the classical electron radius $r_e = e^2/(4\pi\varepsilon_0)(mc^2)$:

$$n(\omega) = 1-\frac{n_a r_e \lambda^2}{2\pi} f^0(\omega) \tag{A.15}$$

where λ is the wavelength of radiation and

$$f^0(\omega) = \sum_s g_s \frac{\omega^2}{(\omega^2-\omega_s^2)+i\gamma\omega} \tag{A.16}$$

is the complex atomic scattering factor, whose real $(f_1^0(\omega))$ and imaginary $(f_2^0(\omega))$ parts are:

$$f_1^0(\omega) = \sum_s g_s \frac{\omega^2(\omega^2 - \omega_s^2)}{(\omega^2 - \omega_s^2)^2 + \gamma^2\omega^2} \tag{A.17}$$

$$f_2^0(\omega) = \sum_s g_s \frac{\gamma\omega^2}{(\omega^2 - \omega_s^2)^2 + \gamma^2\omega^2} \tag{A.18}$$

The two optical constant, f_1^0 and f_2^0, describes two physical interactions: the phase shifts and the absorption of X-ray into the matter. However, they are linked together by the well known Kramers-Kronig relations (KK relationships) [4, 48], first derived in 1927:

$$f_1^0(\omega) = Z - \frac{2}{\pi}\wp\int_0^\infty \frac{u f_2^0(u)}{u^2 - \omega^2}\,du \tag{A.19}$$

$$f_2^0(\omega) = \frac{2\omega}{\pi}\wp\int_0^\infty \frac{f_1^0(u) - Z}{u^2 - \omega^2}\,du \tag{A.20}$$

In eqs. (A.19) and (A.20), $\wp$ indicates taking only the non-divergent Cauchy principal part of the integral.